# Investigation of Reactive Transport and Coupled THM Processes in EBS: FY12 Report

## Fuel Cycle Research & Development

*Prepared for*

*U.S. Department of Energy*
*Used Fuel Disposition*

*Jonny Rutqvist*
*Carl Steefel*
*James Davis*
*Ian Bourg*
*Ruth Tinnacher*
*Juan Galindez*
*Michael Holmboe*
*Jens Birkholzer*
*Hui-Hai Liu*

*Lawrence Berkeley National Laboratory*

*May, 2012*

**FCRD-UFD-2012-000125**

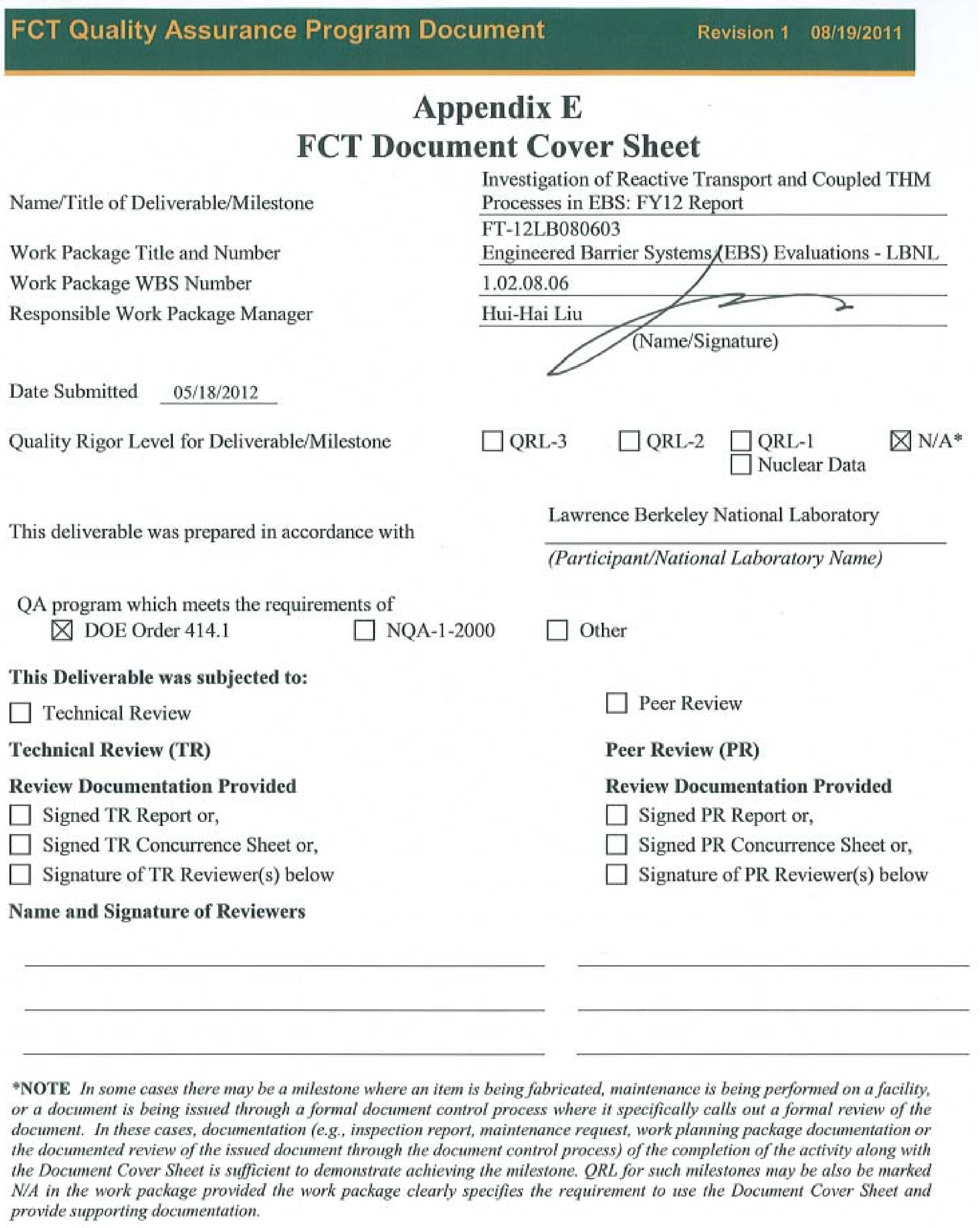

**FCT Quality Assurance Program Document** Revision 1 08/19/2011

# Appendix E
# FCT Document Cover Sheet

| | |
|---|---|
| Name/Title of Deliverable/Milestone | Investigation of Reactive Transport and Coupled THM Processes in EBS: FY12 Report |
| Work Package Title and Number | FT-12LB080603<br>Engineered Barrier Systems (EBS) Evaluations - LBNL |
| Work Package WBS Number | 1.02.08.06 |
| Responsible Work Package Manager | Hui-Hai Liu<br>(Name/Signature) |

Date Submitted 05/18/2012

Quality Rigor Level for Deliverable/Milestone ☐ QRL-3 ☐ QRL-2 ☐ QRL-1 ☐ Nuclear Data ☒ N/A*

This deliverable was prepared in accordance with Lawrence Berkeley National Laboratory
*(Participant/National Laboratory Name)*

QA program which meets the requirements of
☒ DOE Order 414.1 ☐ NQA-1-2000 ☐ Other

**This Deliverable was subjected to:**

☐ Technical Review ☐ Peer Review

| | |
|---|---|
| **Technical Review (TR)** | **Peer Review (PR)** |
| **Review Documentation Provided** | **Review Documentation Provided** |
| ☐ Signed TR Report or, | ☐ Signed PR Report or, |
| ☐ Signed TR Concurrence Sheet or, | ☐ Signed PR Concurrence Sheet or, |
| ☐ Signature of TR Reviewer(s) below | ☐ Signature of PR Reviewer(s) below |

**Name and Signature of Reviewers**

***NOTE** *In some cases there may be a milestone where an item is being fabricated, maintenance is being performed on a facility, or a document is being issued through a formal document control process where it specifically calls out a formal review of the document. In these cases, documentation (e.g., inspection report, maintenance request, work planning package documentation or the documented review of the issued document through the document control process) of the completion of the activity along with the Document Cover Sheet is sufficient to demonstrate achieving the milestone. QRL for such milestones may be also be marked N/A in the work package provided the work package clearly specifies the requirement to use the Document Cover Sheet and provide supporting documentation.*

This page is intentionally blank.

# CONTENTS

# FIGURES

# ACRONYMS

| | |
|---|---|
| BBM | Barcelona Basic Model |
| BExM | Barcelona Expansive Model |
| CEC | cation exchange capacity |
| DDL | diffuse double layer |
| EBS | engineered barrier system |
| EDZ | Excavation Disturbed Zone |
| FEPs | Features, Events and Processes |
| LC | loading-collapse |
| MC | microstructural contraction |
| MMT | montmorillonite |
| MS | microstructural swelling |
| NBS | natural barrier system |
| NL | Neutral Line |
| PA | performance assessment |
| P-N-P | Poisson-Nernst-Planck |
| SCMs | surface complexation models |
| THMC | thermal-hydrological-mechanical-chemical |
| TIC | Total Inorganic Carbon |
| UFD | Used Fuel Disposition |
| UDM | User Defined constitutive Model |
| ZPC | Zero Point of Charge |

# 1. INTRODUCTION

Geological repositories for disposal of high-level nuclear waste generally rely on a multibarrier system to isolate radioactive waste from the biosphere. The multibarrier system typically consists of the natural barrier system (NBS), which includes the repository host rock and its surrounding subsurface environment, and the engineered barrier system (EBS). The EBS represents the man-made, engineered materials placed within a repository, including the waste form, waste canisters, buffer materials, backfill, and seals (OECD, 2003). The EBS plays a significant role in the containment and long-term retardation of radionuclide release.

During the lifespan of a geologic repository, the performance of the EBS is affected by complex thermal, hydrogeological, mechanical, chemical and biological processes, such as heat release due to radionuclide decay, multiphase flow (including gas release due to canister corrosion), swelling of buffer materials, radionuclide diffusive transport, waste dissolution, and chemical reactions. All these processes are related to each other. An in-depth understanding of these coupled processes is critical for the performance assessment (PA) of an EBS and the entire repository. Within the EBS work package of the Used Fuel Disposition (UFD) Campaign, LBNL's research is currently focused on two relevant areas, namely (1) the thermal-hydrological-mechanical-chemical (THMC) processes in buffer materials (bentonite), and (2) the diffusive transport in the EBS associated with clay host rock, with the long-term goal of developing a full understanding of (and verified modeling capabilities to simulate) the impact of coupled processes on radionuclide transport in different components of EBS, as well as the interaction between the EBS components and the near-field host rock (e.g., clay/shale)—and how these processes affect radionuclide release.

LBNL's focus areas address key Features, Events and Processes (FEPs), which have been ranked in importance from medium to high, as listed in Tables 7 and 8 of the *Used Fuel Disposition Campaign Disposal Research and Development Roadmap* (FCR&D-USED-2011-000065 REV0) (Nutt, 2011). Specifically, they address FEP 2.2.01, Excavation Disturbed Zone (EDZ), for shale by investigating the effects of coupled processes on interactions between shale (clay) disposal formations and the EBS; FEPs 2.1.04.01, Buffer/Backfill; FEPs 2.1.07.02, 03, 04, 09, Mechanical Processes; FEPs 2.1.08.03, 07, 08, Hydrologic Processes; and FEP 2.1.11.04, Thermal Processes, by studying coupled processes in the EBS; and FEPs 2.1.09.52, 53, 54, Chemical Processes—Transport, by investigating reactive-diffusive radionuclide transport in bentonite.

This report documents the progress that LBNL has made in its two R&D focus areas in FY12. Section 2 presents the modeling results of THM processes within bentonite and the interaction between the EBS and a clay disposal formation in the near field. Sections 3 and 4 document the development of reactive-diffusive transport modeling approaches for radionuclide migration in bentonite, supported by molecular dynamics simulations of ion diffusion. Section 5 reports on experimental studies of reactive diffusive transport of U(VI) in bentonite. Work activities in the remaining months of FY12 and proposed activities in FY13 are presented in Section 6.

# 2. MODELING COUPLED THM PROCESSES IN EBS

The long-term chemical and mechanical stability of protective bentonite buffers and tunnel backfill is a key issue in the long-term performance of backfilled, multiple barrier nuclear waste repositories. For example, a certain swelling pressure should be maintained to keep the buffer homogenous, to prevent canister sinking, to prevent the adverse effect of external rock shear movements, to limit colloid transport, and to prevent the buffer from being a preferred pathway of radionuclide transport. The long-term stability of the buffer is governed by coupled thermal-hydrological-mechanical and chemical (THMC) processes. These coupled THMC processes can be simulated by numerical modeling, e.g., by a coupling of LBNL's TOUGHREACT reactive transport simulator to a geomechanical code such as FLAC3D. However, this requires appropriate constitutive models describing couplings between the different processes.

In this section, we describe our ongoing work on developing and applications of such models for the analysis of EBS coupled processes. We have previously implemented the Barcelona Basic Model (BBM) into the TOUGH-FLAC simulator in FY11 and currently are expanding this to a dual-structure model for expansive clay, such as bentonite. A dual-structure model has important features for modeling the mechanical behavior of a bentonite buffer, such as irreversible strain during suction cycles. However, most importantly, a dual-structure model provides the necessary link between chemistry and mechanics, enabling us to develop a fully coupled THMC model for the analysis of long-term EBS behavior.

In FY11, we focused on using TOUGH-FLAC with the newly implemented Barcelona Basic Model (BBM) for simulating coupled THM processes within a generic bentonite-backfilled emplacement tunnel and its interactions with the natural system (clay formations). In FY12, we are continuing such analysis, including more parameter studies, with the aim of summarizing this work in a journal paper. A substantial amount of FY12 work is being devoted to implementing a dual-structure model into TOUGH-FLAC for more rigorous modeling of expansive clay and potential coupling to chemistry. In addition, we are initiating modeling of the HE-heater test at the Mont Terri underground research laboratory, as a participant in the international DECOVALEX project. The HE-heater test is an ongoing half-scale heater experiment for EBS and near-field behavior; the measurements on coupled processes parameters will help validate the ongoing model development.

## 2.1 Sensitivity Studies Related to EBS THM Modeling of a Generic Repository

In FY12, we have continued EBS modeling using the newly implemented BBM model in TOUGH-FLAC for parameter study and scenario analysis. This work is being summarized in a journal paper related to a presentation made at the international TIMODAZ project workshop at Mont Terri, Switzerland, February 7 and 8, 2012. The journal paper describes the new code developments for EBS and their applications to a generic repository in a clay host rock.

In these simulations, we considered clay host-rock properties derived from the Opalinus clay at Mont Terri, Switzerland (Gens et al., 2007). The EBS design featured waste emplacement in horizontal tunnels back-filled with bentonite-based swelling clays as a protective buffer (Figure 2.1).

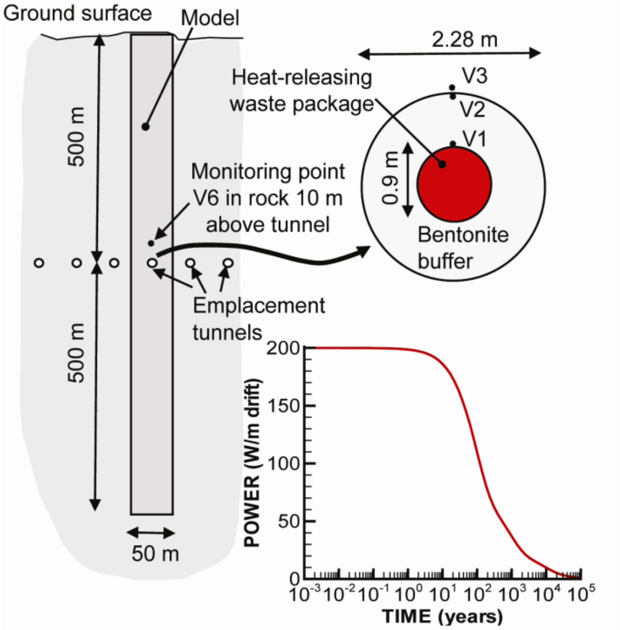

Figure 2.1. Model domain for an assumed bentonite back-filled horizontal emplacement drift at 500 m depth in clay host rock.

In FY11, a comprehensive sensitivity study was completed related to (1) thermal management and peak temperature, (2) resaturation time and buffer swelling, and (3) rock failure for layered rock. The FY11 modeling included extreme temperature conditions, leading to very high temperature in the buffer, slow buffer resaturation, and strong thermal pressurization. The thermal pressurization was related to thermal expansion of fluids in the pores of the low permeability clay host rock, leading to pore-pressure increases around the repository horizon lasting for thousands of years.

In FY12, we made additional simulations considering more realistic conditions and properties than what were assumed in some of the FY11 simulations:

1) In the case of the buffer consisting of bentonite pellets (rather than bentonite blocks), the initial water saturation of 1% considered in the FY11 modeling study was deemed unrealistic, based on observations in field tests at the Mont Terri underground laboratory. Even though the saturation could be a few percent during emplacement, the pellets will quickly equilibrate with the relative humidity in the air, and therefore an initial saturation around 20 to 25% would be realistic. In FY12, we conducted additional simulations in which the initial saturation was set to 20% in the case of a bentonite pellet.

2) In the extreme case of low rock thermal conductivity, a low initial buffer saturation, and a high thermal line load, a peak temperature up to 150°C was achieved in the FY11 sensitivity study. The justification for such a high peak temperature was based on early thermal simulations within the Swiss nuclear waste program, where such a high temperature was considered. However, the current concept targets the temperature at the canister-bentonite interface to be between 125°C and 135°C. This is also what is being considered as the upper target temperature at the planned full scale demonstration heater test at Mont Terri, although

the scientific basis for this is not yet fully established. Thus, in FY12, we conducted simulations for peak temperatures up to 135°C.

3) In the FY11 model simulations, a layered rock formation was considered corresponding to that of the Opalinus clay observed at the Mont Terri rock laboratory. However, Mont Terri is relatively shallow, in a sloping part of the Opalinus clay, with a layering dipping at an angle of 45°. A repository would likely be placed at deeper locations, where the target repository units would be horizontal, with horizontal beddings, and with relatively stiffer geomechanical properties as a result of compaction. In FY12, we therefore conducted simulations for the case of horizontal bedding planes.

Figure 2.2 shows an example of simulation results for a bentonite buffer made of dry pellets having an initial saturation of 20%. The peak temperature is 118°C at 40 years, whereas the peak temperature in the Opalinus clay is less than 100°C (Figure 2.2a). Time to complete saturation of the buffer is 100 years, and there is significant thermal pressurization. When the layers of the Opalinus clay are horizontal, the potential for shear failure along bedding planes is much less, since no significant thermally induced shear stress develops along the beddings in such a case.

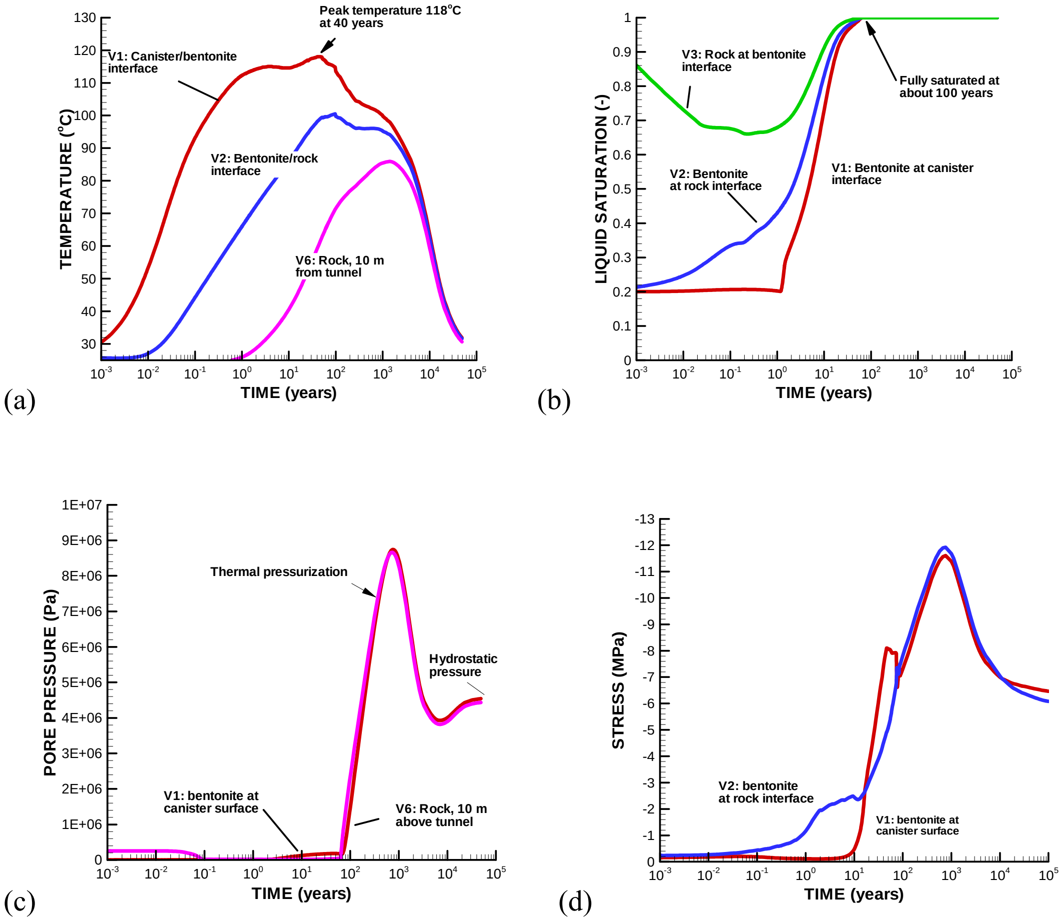

Figure 2.2. Simulated evolution of THM processes in buffer: (a) temperature, (b) liquid saturation, (c) fluid pressure, and (d) total radial stress (σx). See Figure 2.1 for locations of V1, V2, V3, and V6.

## 2.2 Implementation of a Dual-Structure Bentonite Model into TOUGH-FLAC

In this section, we present the development and implementation of a dual-structure material model of expansive clay into TOUGH-FLAC. In such a model, the material consists of two structural levels: a microstructure in which the interactions occur at the particle level, and a macrostructure that accounts for the overall fabric arrangement of the material comprising aggregates and macropores (Figure 2.3) (Gens et al., 2006, Sánchez et al., 2005, Gens and Alonso, 1992). The dual-structure (or double-structure) model approach is especially useful when trying to incorporate the effects of chemical variables on the mechanical behavior of expansive clays. Because they contain large amounts of active clay minerals, those materials are especially susceptible to changes in the geochemical environment. Thus, the double structure model can provided the link between mechanical and chemical processes modeling, which enables mechanistic modeling of processes important for long-term buffer stability, including:

- Effect of pore water salinity on swelling (loss of swelling?)
- Conversion of smectite to non-expansive mineral forms (loss of swelling?)
- Cementation by precipitation of silica (buffer becomes brittle?)

In this section, we first present an overview of the basic equations in the dual-structure model following (in part) the developments by Alonso et al. (1999) and Sánchez et al. (2005). We then summarize the implementation of this model into TOUGH-FLAC.

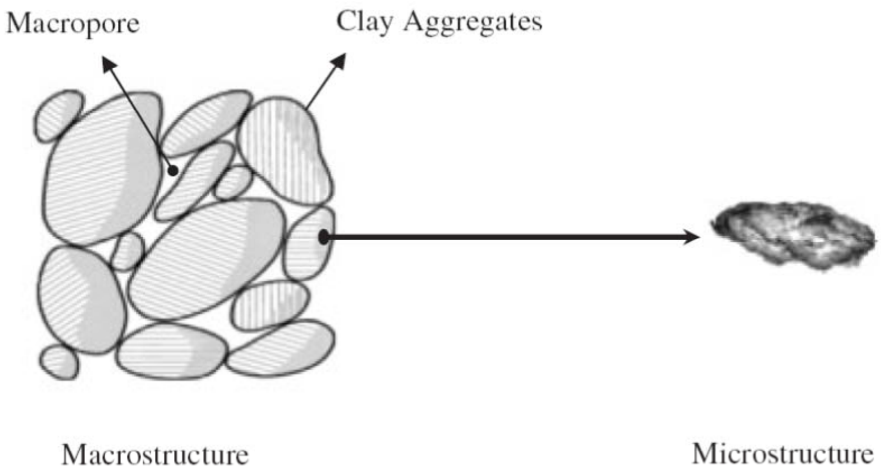

Figure 2.3. Schematic representation of the two structural levels considered (Sánchez et al., 2005).

### 2.2.1 The dual-structure approach and Barcelona Expansive Model

Alonso et al. (1999), in their presentation of the Barcelona Expansive Model (BExM), provide a suitable mathematical formulation for implementation of a dual structure model into TOUGH-FLAC. Sánchez et al. (2005) provide another comprehensive description and mathematical formulation in terms of generalized elastoplasticity and implementation into a finite element code. The implementation of the BExM into TOUGH-FLAC is done as an extension of the existing TOUGH-FLAC implementation of the BBM, adding the microstructural level. The BBM model can describe many typical features of unsaturated-soil mechanical behavior, including wetting-induced swelling or collapse strains, depending on the magnitude of applied stress, as well as the increase in shear strength and apparent preconsolidation stress with suction (Gens et al., 2006). The extension to dual-structure behavior enables modeling of more expansive soils, including dependency of swelling strains and swelling pressures on the initial state and on the stress path, strain accumulation during suction cycles, as well as secondary swelling. It is believed that such behavioral features are mainly related to the existence of coupled chemo-hydro-mechanical phenomena between distinct levels of structure within the material (Alonso et al., 1999).

Conceptually, in a dual-structure model as described by Alonso et al., (1999) and Sánchez et al., (2005), the total volume, $V$, of the material consists of the solid phase, $V_s$, the microstructural voids $V_{vm}$, and the macrostructure voids $V_{vM}$:

$$V = V_s + V_{vm} + V_{vM} = V_m + V_{vM} \tag{2.1}$$

with the total void ratio and porosity being the sum of microstructural and macrostructural components according to

$$e = \frac{V_v}{V_s} = e_M + e_m = \frac{V_{vM}}{V_s} + \frac{V_{vm}}{V_s} \tag{2.2}$$

$$\phi = \frac{V_v}{V} = \phi_M + \phi_m = \frac{V_{vM}}{V_s} + \frac{V_{vm}}{V_s} \tag{2.3}$$

The microstructure can swell to invade the macroporosity, depending on the mechanical confinement and load level. This is relevant when considering permeability changes during bentonite swelling, because fluid movement takes place through the macroporosity, which is not proportional to the total strain and deformation of the bentonite.

### *Macrostructural level*

The macrostructural behavior is modeled based on the BBM, in which the mechanical behavior depends on a three-dimensional yield surface in $p'$-$q$-$s$ space (Figure 2.4), where $p'$ is net mean stress (i.e., total stress minus gas-phase pressure), $q$ is deviatoric stress (or shear stress), and $s$ is suction. The size of the elastic domain increases as suction increases. The rate of increase, represented by the loading-collapse (LC) curve, is one of the fundamental characteristics of the BBM (Gens et al., 2006).

The suction-dependent loading collapse (LC) yield surface (Figure 2.4) bounds the elastic region according to

$$f_{LC} = \frac{q^2}{g_y(\theta)^2} - \frac{M^2}{g_y(\theta = 0)^2}(p' + p_s)(p_0 - p') = 0 \tag{2.4}$$

where $\theta$ is the Lode's angle and the function $g_y(\theta)$ describes the shape of the yield surface in the deviatoric plane. $M$ is the constant slope of the critical state line (Figure 2.4), whereas $p_s$ represents the increase in cohesion with suction and the function

$$p_0 = p^c \left( \frac{p_0^*}{p^c} \right)^{[\lambda_{Ps0} - \kappa_{Ps0}]/[\lambda_{Ps} - \kappa_{Ps0}]} \tag{2.5}$$

is the net mean yield stress (or apparent pre-consolidation stress) at current suction, where $P_0^*$ is the net mean yield stress (or pre-consolidation stress) at full saturation and $\lambda_{PS}$ is a compressibility parameter in virgin soil states at suction $s$.

$$g_{LC} = \frac{\alpha_a q^2}{g_y(\theta)^2} - \frac{M^2}{g_y(\theta = 0)^2} (p' + p_s)(P_0 - p') \tag{2.6}$$

where $\alpha_a$ is a parameter that gives rise to the nonassociative model, i.e., $g_{LC} \neq f_{LC}$.

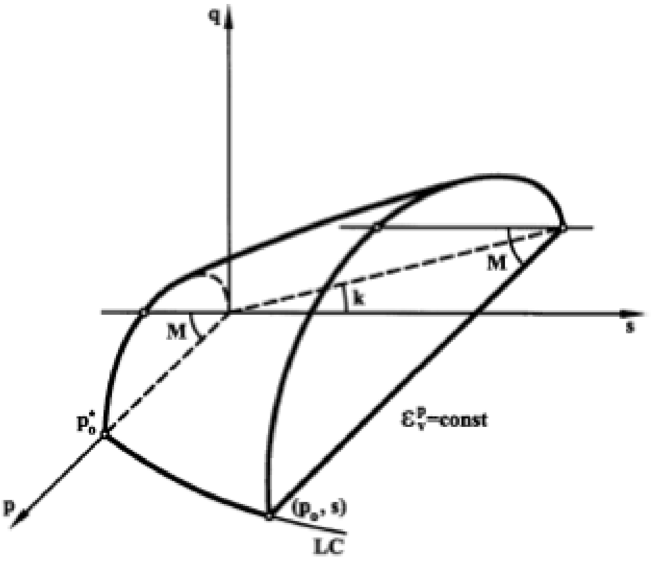

Figure 2.4. Three-dimensional representation of the yield surface in the BBM (Gens et al. 2006).

### *Microstructural level*

In the BExM, the following assumptions are adopted related to microstructural behavior and its interaction with the macrostructure:

- The microstructure is mainly saturated and the effective stress concept holds.
- The microstructural behavior is elastic and volumetric.
- Mechanical, hydraulic, and chemical equilibrium exists between microstructure and macrostructure.
- Coupling between microstructure and macrostructure results in a possible buildup of macrostructural elastoplastic strains when elastic microstructural strains occur.

With these assumptions, the increment of volumetric microstructural strain increment $d\varepsilon_{vm}^e$ depends exclusively on the increment of mean effective stress $dp' = d(p - p^l) = d(p - p^g + p^g - p^l) = d(p+s)$, where $p$ is mean stress (or mean pressure), $p^l$ is liquid phase pressure, $p^g$ is gas phase pressure as *s* is suction. Therefore, a straight line p + s = constant can be drawn around the current state of stress and suction along which no microstructural strain takes place. This line, called Neutral Line (NL), moves with the current stress state (C) and separates at each instant the zone of microstructural swelling from the zone of microstructural shrinkage in the p-s planes (Figure 2.5).

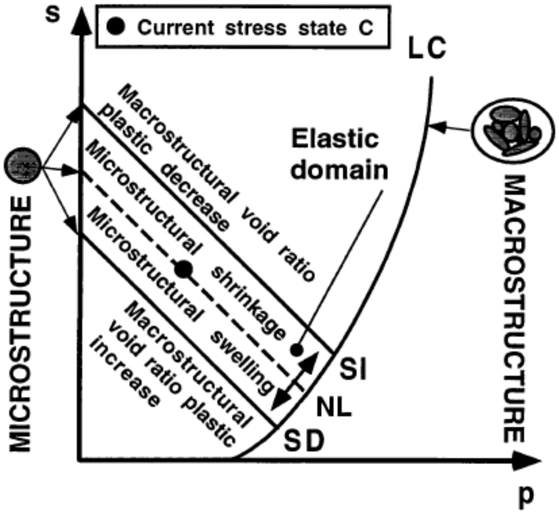

Figure 2.5. Microstructural and macrostructural elastoplastic responses in a double-structure model equivalent to the Barcelona Expansive Model.

### *Interaction between structural levels*

Microstructural swelling affects the structural arrangement of the macrostructure, inducing an irreversible increase of the macroporosity. Reciprocally, microstructural shrinkage induces an irreversible decrease of the macroporosity. In BExM, the irreversible macrostructural deformations induced by microstructural effects are considered proportional to the microstructural strain according to interaction functions with the general form:

$$\mathrm{d}\varepsilon^{p}_{v\beta} = f d\varepsilon^{e}_{vm} \qquad (2.7)$$

where $\varepsilon^{p}_{v\beta}$ is the macrostructural plastic strain arising from the interaction between both structures. Two interaction functions are defined; $f_c$ for MC (microstructural contraction) path and $f_s$ for MS (microstructural swelling) paths (Sánchez et al., 2005). Alonso et al. (1990) proposed the following possible interaction functions, in which case for isotropic loading, $f_c$ and $f_s$ depend on the ratio $p/p_o$ (Figure 2.6).

$$f_c = f_{c0} + f_{c1}\left(p / p_0\right)^{n_c} \text{ and } f_s = f_{s0} + f_{s1}\left(p / p_0\right)^{n_s} \qquad (2.8)$$

The ratio $p/p_o$ is a measure of the distance from the current stress state to the yield locus for the macrostructure *LC* and has the same meaning as the overconsolidation ratio for an isotropically consolidated soil. A low $p/p_o$ implies a dense packing of the material. It is expected that under such dense packing (dense macrostructure), the microstructural swelling strongly affects the global arrangement of clay aggregates, which becomes more open, resulting in a softening of the macrostructure. This also means that the macrostructural yield surface *LC* shrinks. On the other hand, when the microstructure contracts, macrostructural plastic strain can occur under the conditions of an open macrostructure, which tends to a more dense state. In such a case, the elastic domain increases and *LC* expands (Alonso et al. 1999; Sánchez et al., 2005).

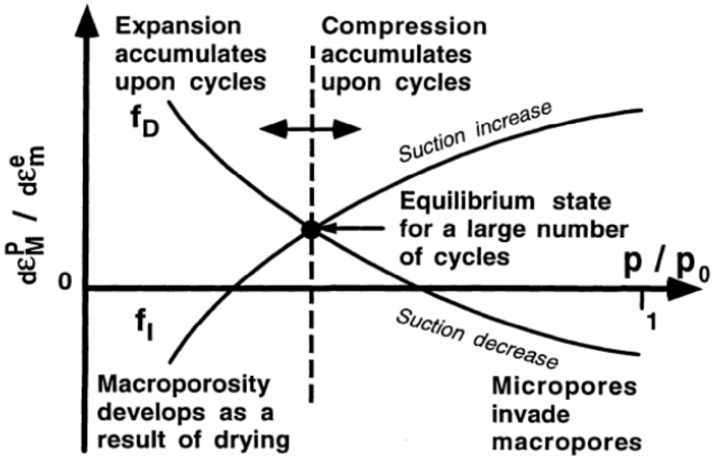

Figure 2.6. Summary of micro–macropore interaction mechanisms.

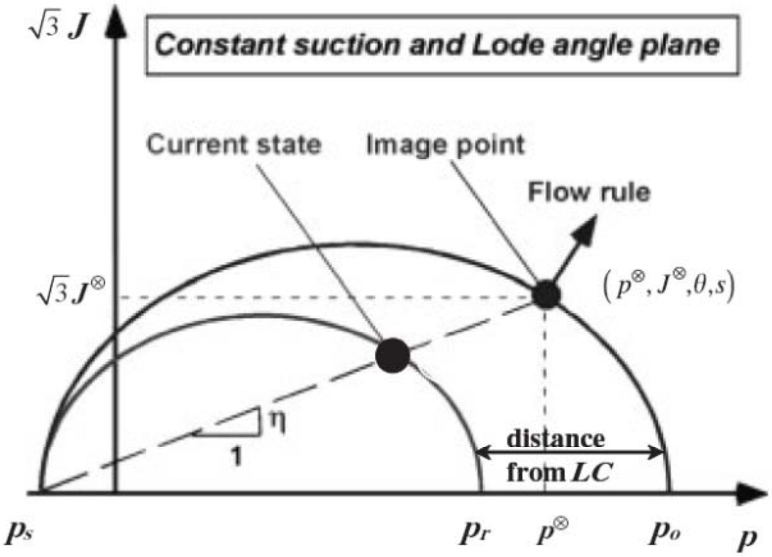

Figure 2.7. Reference pressure and plastic flow direction (Sánchez et al. 2005).

### *Elastic Strain*

Equivalent to the BBM model, the macrostructural volumetric elastic strain increment for the BExM model is associated with changes in net mean stress d$p'$ and suction $ds$ (Alonso et al., 1999)

$$\mathrm{d}\varepsilon_{vM}^{e} = \frac{1}{K_M}\mathrm{d}p' + \frac{1}{K_s}ds \tag{2.10}$$

where $K_M$ is the macrostructural bulk modulus and $K_s$ is the modulus associated with suction strain. $K_M$ and $K_s$ are defined as

$$K_M = \frac{(1+e)p'}{\kappa_{ps}(s)} \tag{2.11}$$

$$K_s = \frac{(1+e)(s+p_{atm})}{\kappa_{sp}(p',s)} \tag{2.12}$$

where $\kappa_{ps}$ and $\kappa_{SP}$ are compressibility parameters.

In BExM, the microstructural volumetric strain depends on the change in the microstructural effective stress

$$\mathrm{d}\varepsilon_{vm}^{e} = \frac{1}{K_m}\mathrm{d}\widehat{p} \tag{2.13}$$

where $K_m$ is the microstructural bulk modulus for change in mean effective stress. Alonso et al. (1999) define two alternative laws for the microstructural behavior through two alternative expression for the microstructural modulus

$$K_m = \frac{(1+e)\hat{p}}{\kappa_{ps}(s)} \tag{2.14}$$

$$K_m = \frac{e^{-\alpha_m \hat{p}}}{\beta_m} \tag{2.15}$$

The deviatoric elastic strain increment is defined as

$$d\varepsilon_{q}^{e} = \frac{1}{3G}dq \tag{2.16}$$

where $G$ may be obtained using a constant Poisson's ratio $\nu$ in

$$G = \frac{3(1-2\upsilon)}{2(1+\upsilon)}K \tag{2.17}$$

Thus, the equations for elastic mechanical strain indicate the dependency of bulk modulus on suction (and hence fluid saturation), which in a dry clay can be significantly stiffer than in a water-saturated clay.

### *Plastic Strain*

Macrostructural plastic strain occurs by two plastic mechanisms: either when the stress lies on the LC yield surface, or as a result of microstructural contraction/swelling (MC and MS path). The increment of volumetric macrostructural strain is described as a result of microstructural contraction/swelling

$$d\varepsilon_{v\beta}^{p} = f d\varepsilon_{vm}^{e} \tag{2.18}$$

where $d\varepsilon_{v\beta}^{p}$ is macrostructural strain as a result of microstructural contraction (MC or MS path).

The coupling between both plastic mechanisms is considered mathematically assuming that:

$$d\varepsilon_{v}^{p} = d\varepsilon_{vLC}^{p} + d\varepsilon_{v\beta}^{p} \tag{2.19}$$

Then the hardening variable of the macrostructure—the pre-consolidation pressure $p_0^*$—depends on the total plastic volumetric strain $\varepsilon_v^p$, which is the sum of the plastic strain induced by LC yielding ($\varepsilon_{LC}^{p}$) and plastic strain induced by microstructural strain impact on the macrostructure $\varepsilon_{v\beta}^{p}$. That is,

$$\frac{dp_0^*}{p_0^*} = \frac{(1+e_M)d\varepsilon_v^p}{\lambda_{ps0} - \kappa} \tag{2.20}$$

When the stress state is on the LC yield surface, the plastic strains are obtained from the plastic flow rule

$$\mathrm{d}\varepsilon_{vLC}^{P} = \mathrm{d}\Lambda \frac{\partial g}{\partial p'} \tag{2.21}$$

$$\mathrm{d}\varepsilon_{qLC}^{P} = \mathrm{d}\Lambda \frac{\partial g}{\partial q} \tag{2.22}$$

where $d\Lambda$ is the plastic multiplier obtained from the consistency condition $df_{LC} = 0$.

The macrostructure plastic strain induced by microstructure volumetric strain is given by the flow rule at the image point on the LC yield surface. The coordinates of the image point ($P^*$, $q^*$, $s^*$ ) are given by (Alonso et al., 1999)

$$p^* = \frac{\eta^2 k_s s - M^2 p_0}{\eta^2 - M^2},\ q^* = \eta(p + k_s s),\ s^* = s$$

where $\eta = \dfrac{q}{p + k_s s}$ (2.23)

### 2.2.2 Implementation of BExM into TOUGH-FLAC

We implemented the BExM in FLAC$^{3D}$, by extending our previous implementation of the BBM to include the microstructure level and its interactions with macrostructure. This is done using the User Defined constitutive Model (UDM) option in FLAC3D, including C++ coding and dynamic link libraries. Specifically, the following calculation items were added

1) Microstructural strain and effective stress
2) Micro/macrostructural interaction functions
3) Plastic macrostructural strain from structural interactions
4) Plastic corrections in the FLAC3D elastoplastic algorithm
5) Plastic hardening/softening factors
6) Global elastic tensor depending on microscopic and macroscopic structural compliances

Implementation of the first three items is straightforward, whereas items 4 and 5 are related to the FLAC3D elastoplastic algorithm and involve calculation of the plastic multiplier $\mathrm{d}\Lambda$ associated with the elastic predictor-plastic corrector algorithm in FLAC3D. In this algorithm, current stress increments are guessed (by Hooke's law) and added to the stresses from the previous time step, and then corrected back to the yield surface if the calculated principal stresses violate the yield criterion. Using such an approach the current stress is calculated as

$$p' = p'_{est} + K\mathrm{d}\Lambda c_a \tag{2.24a}$$

$$q = q_{est} + K\mathrm{d}\Lambda c_b \tag{2.24b}$$

where $p'_{est}$ and $q_{est}$ are the estimated stresses obtained in the previous step, plus the current incremental elastic estimates, and constants $c_a$ and $c_b$ are the components normal to the plastic potential calculated as (Rutqvist et al., 2011):

$$c_a = M^2\left(2p' - p_c + p_s\right) \tag{2.25a}$$

$$c_b = \alpha_a 2q \tag{2.25b}$$

The value of the plastic multiplier $\mathrm{d}\Lambda$ is defined by substituting Equations (2.25a) and (2.25b) in Equation (2.4), requiring that the new stress point be located on the yield surface ($f_{LC}(q, p') = 0$). Then,

$$a(\mathrm{d}\Lambda)^2 + b\mathrm{d}\Lambda + c = 0 \tag{2.26}$$

where

$$a = \left(MKc_a\right)^2 + \left(3Gc_b\right)^2 \tag{2.27a}$$

$$b = -\left[Kc_a c_a^e + \frac{3}{\alpha_a} G c_b c_b^e\right] \tag{2.27b}$$

$$c = f\left(q_{est}, p'_{est}\right) \tag{2.27c}$$

Finally, FLAC$^{3D}$ evaluates new stresses $p'$ and $q$ from Equations (2.24a) and (2.24b) using the expression for $\mathrm{d}\Lambda$ corresponding to the root of Equations (2.26) and (2.27) with smallest magnitude (Rutqvist et al., 2011). In the case of microstructural contraction or swelling (i.e., MC or MS path), the components normal to the plastic potential are given by substituting $p$ and $q$

with $p^*$ and $q^*$ into (2.25a) and (2.25b). In the case of simultaneous *LC* yield and microstructural contraction or swelling, the stress state will be on the *LC* surface, and therefore $p = p^*$ and $q = q^*$, and Equations 2.24–2.27 are still valid.

Finally, in at the end of each FLAC3D step, the hardening parameter, i.e., the pre-consolidation pressure $P_0$ and the tangential bulk modulus, are updated based on the total volumetric strain and stress state, and these are stored for use in the next step.

### 2.2.3 Testing and verification of implementation

The implementation will be tested by comparison of TOUGH-FLAC simulation results to published experimental results such as those provided in Sánchez et al. (2005). In fact, the numerical results by Sánchez et al. (2005) using their implementation into CODE_BRIGHT are to our knowledge the only existing numerical results using this type of dual-structure modeling of unsaturated clay. The implementation and testing will be further documented in a scientific paper and in the next progress report.

## 2.3 Modeling of the Mont Terri HE-Heater Test

We are initiating modeling of the Mont Terri HE-heater test as a participating research team in the newly launched international DECOVALEX-2015 project. DECOVALEX-2015 is the next project phase of the DECOVALEX Project, which is a unique international research collaboration, initiated in 1992 for advancing the understanding and mathematical modeling of coupled thermo-hydro-mechanical (THM) and thermo-hydro-mechanical-chemical (THMC) processes in geological systems—subjects of importance for performance assessment of radioactive waste repositories in geological formations.

The HE-E Heater Test focuses on the THM behavior of bentonite barriers in the early nonisothermal resaturation stage and their THM interaction with Opalinus clay (Figure 2.8). The objective is to better understand the evolution of a disposal system of high level waste in the early post-closure period with emphasis on the thermal evolution, buffer resaturation (*in situ* determination of the thermal conductivity of bentonite and its dependency on saturation), pore water pressure in the near field, and the evolution of swelling pressures in the buffer. Because the test is conducted in a micro-tunnel (at 1:2 scale), it is considered a validation, not a demonstration experiment. The heating test involves two types of bentonite buffer materials. The heater-buffer interface will be heated to a maximum of 135°C and a temperature of 60–70°C is expected at the buffer-rock interface. A dense instrumentation network is already in place in the host rock surrounding the micro-tunnel (from a previous experiment testing the impact of ventilation on the clay host rock) and will be improved (up to 40 piezometers in total); various sensors will also be placed in the buffer material. The heating phase has started in late summer of 2011 and is being continued for at least three years.

A proposed task description and plans for the DECOVALEX 2015 were presented at the 1st DECOVALEX-2015 workshop in Berkeley, April 17–19, 2012. It was decided that the final task description, including all necessary data to begin the modeling activities, will be distributed to the research teams in June 2012. The first task will be to model a previous single heater experiment (HE-D heater test) for determination and calibration of *in situ* properties related to the coupled THM behavior of the Opalinus clay host rock. This includes parameters governing heat transfer and thermal expansion, as well as hydraulic and mechanical coupling parameters.

The modeling of the HE-D heater experiment should be completed by October 2012, before the next DECOVALEX Workshop.

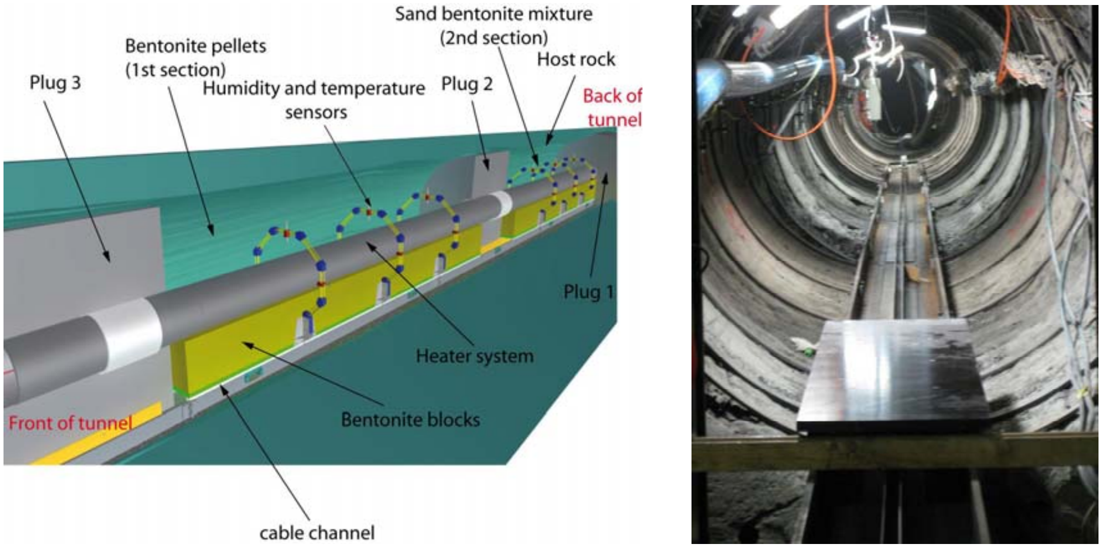

Figure 2.8. Schematic setup of HE-E heater test at Mont Terri and photo of micro-tunnel (Garritte et al. 2012).

## 2.4 Conclusions

We are developing and applying coupled THMC models for the analysis of EBS coupled processes in bentonite-backfilled repositories. In FY11, we developed an advanced modeling capability by implementing the Barcelona Basic Model into the TOUGH-FLAC simulator. In FY12, we have further improved our modeling capability and initiated a modeling validation study using international data sets. We expanded the Barcelona Basic Model to a dual-structure model for expansive clay, such as bentonite. We are currently testing and verifying this implementation against published numerical modeling and experimental data. The next step will be to link the dual-structure model with the diffuse double layer theory for the coupling between chemistry and mechanics, resulting in a coupled THMC model for the analysis of long-term EBS behavior. We have also initiated work on the modeling of the HE-E heater test, along with our participation in the DECOVALEX project. The first phase will involve modeling of a previous HE-D heater test for calibration and validation of the rock-mass model related to THM processes under heating of the Opalinus clay.

# 3. MODELING REACTIVE DIFFUSIVE TRANSPORT

Diffusion is one of the key transport processes that needs to be considered when studying radionuclide transport in the EBS. While it is possible to estimate diffusion coefficients for single species/contaminants in specific media (such as compacted bentonite and clay-rich rock) based on experiments, such an approach does not generally provide a robust predictive capability for diffusion rates across a range of physical and chemical conditions. It would be advantageous, therefore, to develop a more general model that could be used in the context of both mechanistic- and performance-assessment-style simulation tools for geological nuclear waste repositories. In the case of compacted bentonite in particular—but also for clay-rich rocks of the kind considered as host rocks for geological waste repositories in France and Switzerland (e.g., Bure in France and Mt. Terri in Switzerland)—there is a need to include the effect of electrical double layers around the clay in modeling ion transport through the EBS. Electrical double layers affect sorption, but perhaps more importantly, they affect transport. The negatively charged clay particles develop electrical double layers that will be balanced by a cation-enriched double layer. While anions are likely to be excluded completely only at very high degrees of compaction (e.g., a dry density of 1.9 g/cm$^3$—see Tournassat and Appelo, 2011), their concentration is decreased in the double layer even at lower degrees of compaction, and the tortuosity of the compacted clay with respect to chloride changes as well. Both of these contribute to slower diffusive transport rates through the clay (Bourg et al., 2003; Bourg et al., 2006; Leroy et al., 2006; Gonçalvès et al., 2007). These effects become increasingly important as the compaction increases, since this decreases the volume (or porosity) of bulk water at the expense of either the double layer or the clay interlamellar water**.**

Three types of water presence are recognized in compacted bentonite (Bourg et al, 2003; Wersin et al, 2004):

1. Interlayer water ($\phi_{IL)}$ with only water and cations within the Tetrahedral-Octahedral-Tetrahedral (TOT) layers of the montmorillonite. Here, the cations balance the fixed charge of the TOT layers;
2. Diffuse double layer ($\phi_{DDL}$) containing cations and anions, but with an excess of ions (normally cations) to balance the charge of the clay surface;
3. Bulk or free pore water ($\phi_B$), which is charge balanced.

The proportions of each kind of water depend on the compaction of the bentonite, but also on the ionic strength of the solution through its effect on the width of the diffuse double layer (DDL).

We are pursuing two separate but related approaches to modeling ion diffusion through clays. The first makes use of a Donnan equilibrium approach, in which a mean electrostatic potential is defined for the electrical double layer that balances the fixed negative charge of the clays. In this approach, the electrical double layer is treated as a single continuum (no discretization within it) in chemical equilibrium with the bulk water. The second approach involves the use of the Nernst-Planck and Poisson-Boltzmann equation (often referred to as the Poisson-Nernst-Planck or P-N-P equation). In this second approach (which is ultimately what the Donnan equilibrium or mean electrostatic approach is based on), the electrical potential as a function of distance from the charged clay surfaces is resolved. Thus, the concentration of anions and cations varies continuously. In the case of overlapping double layers, as between two clay interlamellae or closely spaced clay particles, the electrical potential does not decay to zero, with the result that the aqueous solution in the center of the space or pore cannot be described as corresponding to "bulk water."

## 3.1 Mean Electrostatic Approach for Diffuse Double Layer

Initially at least, the mean electrostatic or Donnan Equilibrium approach to describing the diffuse electrical double layer balancing the negatively charged clay surfaces is based on the Poisson-Boltzmann equation, a full treatment of which is provided in the next section. A rigorous model for the diffuse layer could be derived from the combination of several equations, including the Poisson equation that describes the distribution of electrical potential, $\varphi$, in water

$$\frac{\partial^2 \varphi}{\partial x^2} = -\frac{\rho_z}{\varepsilon}, \tag{3.1}$$

where $\varepsilon$ is the permittivity and $\rho_z$ is the volumetric charge density given by

$$\rho_z = e \sum_i z_i C_i \tag{3.2}$$

where $e$ is the elementary charge of an ion, $z_i$ is the charge of the ion, and $C_i$ is its concentration. The Boltzmann distribution gives an expression for the concentration $\overline{C_i(x)}$ in the diffuse layer:

$$\overline{C_i(x)} = C_i \exp\left(\frac{-z_i e \varphi(x)}{k_B T}\right) \tag{3.3}$$

where $C_i$ is here the concentration in the bulk solution, $k_B$ is the Boltzmann constant, and $T$ is the absolute temperature. By combining Equation 3.3 with the Poisson equation (Eqn. 3.2) yields the Poisson-Boltzmann equation

$$\frac{\partial^2 \varphi}{\partial x^2} = \frac{-e}{\varepsilon} \sum_i z_i C_i \exp\left(\frac{-z_i e \varphi(x)}{k_B T}\right) \tag{3.4}$$

which can be solved exactly for various simple formulations (e.g., the Gouy-Chapman model). For an arbitrary multicomponent system, Equation 3.4 needs to be solved numerically along with the diffusion equations for the various species.

The approach adopted here treats a porous medium as consisting of three kinds of porosity, corresponding to the kinds of water described above for compacted bentonite. For the Diffuse Double Layer, this involves defining a mean potential for the diffuse layer, the thickness of which will depend on the ionic strength of the solution. Its volume is given by the total surface area of charged mineral multiplied by the diffuse layer thickness:

$$\phi_{DDL} = \tau_{DDL} A_{ext} w_{mont} \rho_{dry} \tag{3.5}$$

where $A_{ext}$ is the external surface area of the montmorillonite, $\tau_{DDL}$ is the thickness of the diffuse layer, $w_{mont}$ is the weight fraction of montmorillonite in the bentonite, and $\rho_{dry}$ is the dry density of the compacted bentonite. At 25°C, the thickness of the diffuse layer can be approximated by the Debye length ($\kappa^{-1}$, the distance over which the potential in the diffuse layer drops by $e$)

$$\tau_{DDL} \cong \kappa^{-1} = \frac{3.04 \times 10^{-10}}{\sqrt{I}} \tag{3.6}$$

where $I$ is the ionic strength (Stumm, 1992; Schoch et al., 2006). In some cases, the diffuse layers may overlap, resulting in a smaller volume for the total diffuse layer per unit volume of porous medium.

### 3.1.1 Donnan Equilibrium Model

Several treatments of an explicit diffuse layer calculation based on a Donnan Equilibrium assumption have been presented in the literature (Wersin et al., 2004; Appelo et al., 2007; Leroy et al., 2007; Appelo et al., 2008). Typically, this involves an assumption that the Donnan Equilibrium condition applies, which equates the chemical potentials of the species in the diffuse layer and the bulk solution. Writing equations for the chemical potentials of the species $i$ in the macroporosity (superscript "B") and microporosity (superscript "MP") respectively, we have

$$\mu_i^B = \mu_i^{B,0} + k_B T \ln a_i^B \tag{3.7}$$

$$\mu_i^{DDL} = \mu_i^{DDL,0} + k_B T \ln a_i^{DDL} + q_i \varphi_m \tag{3.8}$$

where the superscript *0* (first term on the right-hand side) refers to the chemical potential at the reference state, $a_i$ are the species activities, $q_i$, is the charge of an ion (the elementary charge of a particle, $e$, multiplied by the valence of the ion, $z_i$), $k_B$ is the Boltzmann constant, and $\varphi_m$ is the mean electrical potential in the diffuse layer. The condition of Donnan Equilibrium implies that

$$\mu_i^{DDL} = \mu_i^B \tag{3.9}$$

$$\mu_i^{DDL,0} = \mu_i^{B,0} \tag{3.10}$$

Combining Equations 3.7 through 3.10 gives the Boltzmann distribution for the ion activities in the diffuse layer:

$$a_i^{DDL} = a_i^B \exp\left(\frac{-z_i e \varphi_m}{k_B T}\right) \tag{3.11}$$

If the activity coefficients for the ions are assumed to be the same in the diffuse layer and the bulk water (probably not strictly true, but we would need a much more sophisticated model to improve on this assumption), then one can use Equation 3.11 to calculate concentrations in the diffuse layer as well

$$C_i^{DDL} = C_i^B \exp\left(\frac{-z_i e \varphi_m}{k_B T}\right) \tag{3.12}$$

Note that from Equation 3.12, it is possible to calculate all of the concentrations in the diffuse layer once its mean potential is determined numerically. The mean potential of the diffuse layer can be calculated with an additional charge balance equation:

$$\phi^{DDL}\sum_{i} z_i C_i^{DDL} = Q^{SL} \tag{3.13}$$

where $Q^{SL}$ is the total charge in the Stern Layer calculated with the surface complexation model, $\phi^{DDL}$ is again the volume of the diffuse layer, and $C_i^{DDL}$ is the concentration in mol m$^{-3}$. The left-hand side of Equation 3.13 gives a volumetric charge density in units of charge equivalents per unit volume porous medium. The surface charge is given by

$$Q^{SL} = \sum_{k}^{Ns} z_k \Gamma_k \tag{3.14}$$

where $\Gamma_k$ is the concentration in units of moles sorbed species per unit volume porous medium and $z_k$ is the valence of the surface complex. By combining the Boltzmann equation (Eqn. 3.12), and the charge balance (Equation 3.13), it is possible to calculate the mean potential of the diffuse layer, $\varphi_m$, along with the total concentrations of the primary species partitioned between the mineral surfaces (the Stern Layer), the diffuse layer, and the bulk solution. Since Equation 3.12 provides an algebraic relationship between the primary species in the bulk water and diffuse layer, it is not necessary to introduce the primary species in the diffuse layer as independent unknowns. In contrast, a kinetic treatment of the exchange between the two domains would require that the primary species in the diffuse layer be considered as independent unknowns.

### 3.1.2 Dynamic Calculation of Double Layer Width

Previously, the volume corresponding to the "microporosity" or electrical double layer sub-continuum was calculated in advance using Eqn. 3.4. During FY12, we have added the capability to calculate this quantity dynamically at initialization, although update of the double layer thickness (on input, as some fraction or multiple of the Debye Length defined in Eqn. 3.4) is not yet possible. It turns out that an update of the diffuse layer volume (or porosity) requires weighting appropriately both the old and the new concentrations in the accumulation term within an individual time step, or a significant mass-balance error develops. Adding this feature is planned for the continuing FY12 work. When this is complete, it will be possible to simulate the effects of a changing double layer volume as a result of a propagating ionic strength (or salinity) wave. Currently, this option is now available only during the initialization—the user specifies multiples of the Debye length to be considered, and this is multiplied by the total surface area of the clay (typically bentonite) specified in the input. This also makes it possible for the DDL volume to be spatially variable.

Figure 3.1 shows the results of two calculations of the same 25 cm clay domain that use the same surface area of illitic clay (200 m$^2$/g) present at 20% of the rock volume. A site density of $5.88\times10^{-6}$ mol sites/m$^2$ illite is used to determine the fixed mineral charge, which is variable in this case because of the inclusion of pH-dependent surface complexation. A no-flux boundary is used at 25 cm (on the right side of the domain), while the left boundary is treated as a Dirichlet (fixed concentration) boundary condition. At pH 7.5, two cases are considered: (1) a case in which the bulk water ionic strength is 0.04M, and (2) a case in which the bulk water ionic strength is 0.4M. The cations in the initial domain ($Na^+$, $Ca^{2+}$, and $Mg^{2+}$ at 0.1M, 0.05M, and 0.05M in the higher ionic strength case and 0.01M, 0.005M, and 0.005M respectively in the lower ionic strength case) are balanced by bromide. In the 0.4 M ionic strength case, a total site density of 1.509 moles sites/L solution is calculated, with 82% of the sites negatively charged. A diffuse layer microporosity of 1% is calculated. In the 0.04 M case, nearly the same percentage of negatively charged sites (82%) is calculated, resulting in 1.238 moles negatively charged sites per liter solution. A microporosity of 3.3% is calculated in the 0.04 M ionic strength case. The boundary condition consists of $K^+$ at either 0.1M (high ionic strength) or 0.01M (lower ionic strength) in place of $Na^+$ and chloride rather than bromide as the balancing anion. Solving for the Nernst-Planck equation, the range of diffusivities in the bulk water porosity (12%) is assumed to be representative of bulk water without a tortuosity connection such that the values range from $8.37 \times 10^{-5}$ $cm^2/s$ for $H^+$ to $7.3 \times 10^{-6}$ $cm^2/s$ in the case of $Ca^{2+}$ and $Mg^{2+}$. Diffusivities in the electrical double layer are assumed to be an order of magnitude lower than in the bulk water macroporosity. In both cases, potassium diffuses into the domain while sodium diffuses out. Chloride also diffuses into the domain, replacing bromide as the balancing anion.

Figure 3.1 shows the results of the simulation after 10 days over the 10 cm close to the fixed concentration (Dirichlet) boundary on the left. Chloride is suppressed (partially excluded) in both cases, but the difference between the double layer porosity and the bulk water porosity is more pronounced at lower ionic strength. Sodium is strongly enriched in the diffuse layer at lower ionic strength (0.04M), although the gap between diffuse layer and bulk water porosity is equally pronounced at high ionic strength because of the presence of the divalent cations, which tend to balance the charge in this case.

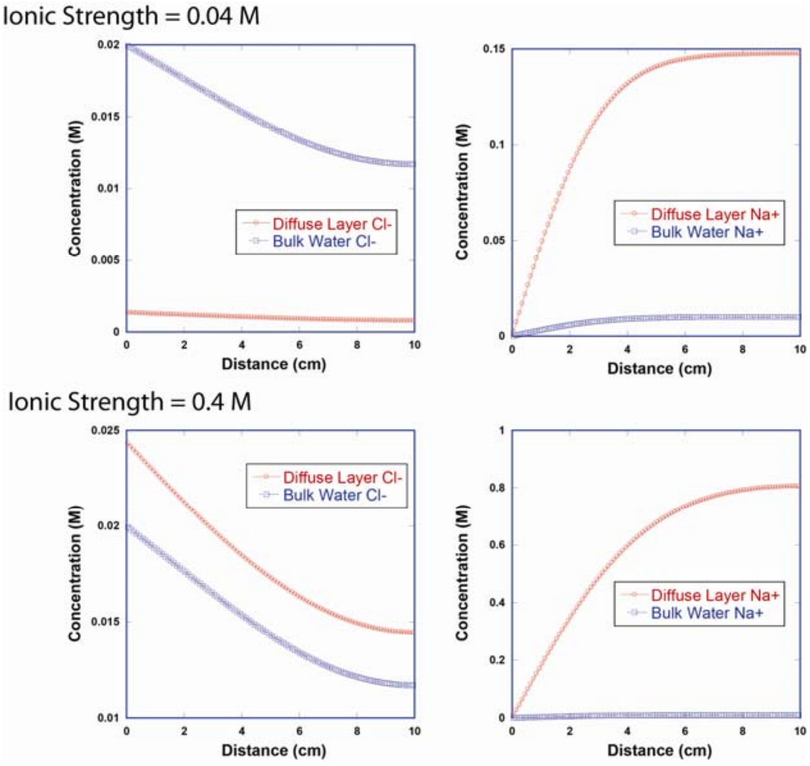

Figure 3.1. Effect of ionic strength on the anion (chloride) and cation (sodium) concentrations in the diffuse double layer compared to the bulk water.

### 3.1.3 Alternative Models for Montmorillonite Surface Charge

The classical surface complexation model considers the possibility of cations being added to the Stern layer, thus changing the net charge that needs to be balanced by the diffuse layer. In some clays, protonation and deprotonation reactions can change the charge—at the pH corresponding to the Zero Point of Charge (ZPC), in fact, the net charge of the surface in these clays is zero. In the case of the planar sites on montmorillonite, the clay making up most of the bentonite, the sites are not easily protonated or deprotonated. As a result, ion exchange models that do not consider protonation are often considered. In the case of the mean electrostatic diffuse layer model described here, it is now possible to consider either completely fixed mineral surface charge, in which case all of the charge is accommodated by the diffuse layer, or a case in which only cation (exclusive of protons) sorption in the Stern layer is included. The latter case has been investigated by using surface complexation reactions that do not include $H^+$, but allow for Stern layer sorption of $Ca^{2+}$, $Mg^{2+}$, $Na^+$, and $K^+$.

When modeling experimental data like that presented in Fernández and Mäder (2011), the ability to partition between the Stern layer (which is assumed to be largely immobile) and the diffuse layer itself is an advantage for achieving the best possible fit with the experimental data. Here we present the initial speciation of the initial conditions for a column experiment conducted over a period of 300 days by Fernández and Mäder (2011).

Table 3.1. Initial and boundary conditions for the column experiment conducted by Fernández and Mäder (2011).

| **Component** | **Initial Condition** |
|---|---|
| pH | 8.5 |
| $Na^+$ | 400 |
| $Ca^{2+}$ | 23 |
| $Mg^{2+}$ | 15 |
| $K^+$ | 2.7 |
| $Cl^-$ | 362 |
| $SO_4^{2-}$ | 58 |

The non-electrostatic surface complexation constants used in the speciation calculations are given in Table 3.2. The simulations indicate that only 0.265% of the sites are filled by cations, leaving the rest of the montmorillonite surface as negatively charged. For the initial conditions in Table 3.1, the computed percentages are 0.263%, 0.0012%, and 0.00068% for $Na^+$, $Ca^{2+}$, and $Mg^{2+}$, respectively, while the coverage by $K^+$ is insignificant. The remainder of the 9.32 moles site/liter will be unfilled, negatively charged hydroxyl sites that are balanced by cation enrichment in the diffuse layer.

Table 3.2. Surface complexation constants (non-electrostatic) used in speciation calculations for initial condition (from Fernández and Mäder, 2011)

| **Reaction** | **Log Keq** |
|---|---|
| $>\text{Montmor-Ca}^{2+} \rightarrow \text{Ca}^{2+} + 2\ >\text{Montmor-}$ | 3.58 |
| $>\text{Montmor-Mg}^{2+} \rightarrow \text{Mg}^{2+} + 2\ >\text{Montmor-}$ | 3.64 |
| $>\text{Montmor-Na}^{+} \rightarrow \text{Na}^{+} +\ >\text{Montmor-}$ | 5.99 |
| $>\text{Montmor-K}^{+} \rightarrow \text{K}^{+} +\ >\text{Montmor-}$ | 1.99 |

## 3.2 Poisson-Nernst-Planck Approach

Surface phenomena in the clay pore space gain in relevance as the level of compaction increases and the dimensions of the space confined between clay layers shifts towards the range of nanometers. At such scales, solute transport can no longer be explained by concentration gradients alone. In fact, DDL develops in the neighborhood of the negatively charged clay surfaces can extend well into the aqueous phase, effectively constraining the space available to anions (an event known as anion exclusion) and, in general, distorting the spatial distribution of ionic species in solution. This can be addressed by solving the Poisson-Nernst-Planck (PNP) set of equations, which allows for the determination of the electric potential over the entire domain, along with the spatial distribution of the concentration of ionic species. Although this approach has been taken for some time in the field of nanofluidic dynamics, it has largely been neglected in clay science.

In this sense, the model that has been developed here may constitute a significant step forward towards the understanding of solute transport in highly compacted clays, because it makes it possible to avoid the simplifying assumptions that pervade previous modeling efforts, and perhaps most importantly, that limit the extension of results to differing conditions.

A brief review of the commonly used simplifications include:

a) Treatment of molecular diffusion as described by Fick's law, where the diffusion rate is linearly proportional to the concentration gradient alone;

b) Surface complexation models, whether of the double- (e.g., Avena and De Pauli, 1998) or triple-layer (e.g., Leroy and Revil, 2004) type, relying on the assumption that counter-ions swarming in a fully developed DDL would neutralize the charge density of the clay surface. From a mathematical standpoint, that implies that the set of equations is closed by the following additional expression:

$$Q_d = -\varepsilon \frac{\partial \varphi}{\partial n} = \operatorname{sgn} \varphi_0 \left\{ 2\varepsilon RTI_c \sum_i C_i^* \left[ \exp\left( -\frac{z_i F \varphi_0}{RT} \right) - 1 \right] \right\}^{1/2} \tag{3.15}$$

where $Q_d$ is the electrical charge as integrated over the whole extension of the DDL and $\varphi_0$ is the electrical potential at the shear plane.

c) Anion exclusion effects (which entail an effective reduction of the anion-accessible porosity) being explained in terms of a Donnan equilibrium between pore and external solutions (see Section 3.1 above), along with charge-balance considerations, as in Birgersson and Karnland (2009).

As the mean pore size decreases, e.g., as a result of compaction, DDL developing on opposite clay surfaces may overlap (Gonçalvès et al., 2007). On the one hand, this increases the relative weight of migration into solute transport, as diffusing ions are subjected to non-negligible electrical forces. On the other hand, this dilutes the independence of surface complexation reactions with respect to solute transport, as the evolving ion spatial distribution influences the charge of the DDL, $Q_d$. Finally, by allowing for a continuous spatial distribution of ionic species both along and transversally to the direction of the pore axis, the PNP set of equations suggests that it is not possible to discretize the pore space in a nonphysical way (e.g., micro- and macroporosity, total and anion-accessible porosity, etc.).

### 3.2.1 Conceptual model

The present PNP model relies on the following set of statements:

a. Solutes may be either adsorbed to the clay surface or remain mobile in the pore space;
b. These two distinctly different behaviors correspond to the two domains on either side of the so-called shear plane;
c. Double- or triple-layer models can be used in simulating surface complexation reactions;
d. On the diffuse layer side of the shear plane, diffusion of ionic species is simulated by means of the PNP set of equations;
e. Continuity of mass and electric potential should hold at the Stern layer, which implies a permanent feedback between both domains.

Figure 3.2 shows a sketch of the triple layer model and its related electric potential profiles for the cases of fully developed and truncated (overlapping) diffuse layers.

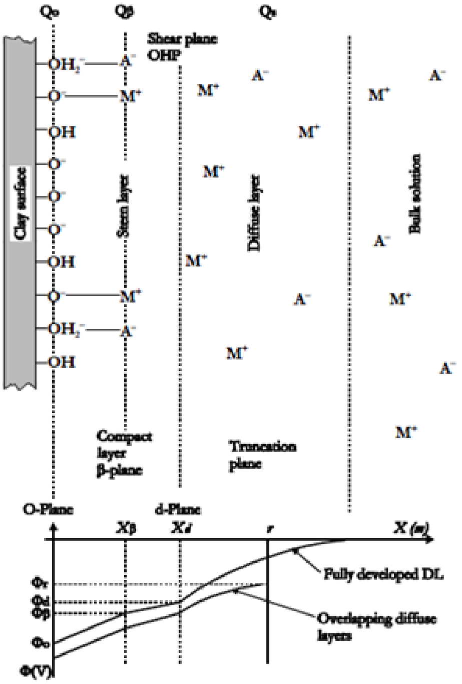

Figure 3.2. Sketch of the triple-layer model at clay surface (top) and its related electrical potential in the cases of truncated and untruncated diffuse layers (bottom). M+ represents a metal cation (e.g., Na+) and A− an anion (e.g., Cl−). OHP is the outer Helmholtz plane. The d-plane is associated with the shear plane; i.e., φd ~ξ, where ξ is the zeta potential arising in electrokinetic phenomena. The β-plane and 0-plane are respectively the mean plane in of Stern layer and the surface of the clay particle. After Gonçalvès et al. (2007).

### 3.2.2 Surface complexation

While ample literature exists on this particular topic, a surface complexation model of Avena and Pauli (1998), developed specifically for clays, is worth looking at as potentially useful for the present research.

The following cation exchange reactions are considered in the model:

$$\begin{aligned} X + H^+ &\rightleftharpoons XH^+ \\ X + Na^+ &\rightleftharpoons XNa^+ \end{aligned} \tag{3.16}$$

along with protonation/deprotonation reactions:

$$\begin{aligned} SOH_2^+ &\rightleftharpoons SOH + H^+ \\ SOH &\rightleftharpoons SO^- + H^+ \end{aligned} \tag{3.17}$$

whose reaction constants are, respectively:

$$K_1 = \frac{\left\{XH^+\right\}}{\left\{X\right\}\left[H^+\right]}\exp\left(\frac{F\varphi_0}{RT}\right) \tag{3.18}$$

$$K_2 = \frac{\{XNa^+\}}{\{X\}\left[Na^+\right]}\exp\left(\frac{F\varphi_0}{RT}\right) \tag{3.19}$$

$$K_3 = \frac{\{SOH_2^+\}}{\{SOH\}\left[H^+\right]}\exp\left(\frac{F\varphi_0}{RT}\right) \tag{3.20}$$

$$K_4 = \frac{\{SOH\}}{\{SO^-\}\left[H^+\right]}\exp\left(\frac{F\varphi_0}{RT}\right) \tag{3.21}$$

Mass-balance equations are:

$$N_1 = \{X\} + \{XNa^+\} + \{XH^+\} \tag{3.22}$$

$$N_2 = \{SOH_2^+\} + \{SO^-\} + \{SOH\} \tag{3.23}$$

where $N_1$ and $N_2$ are the surface densities of variable charged sites, and are given in mol/m$^2$. The structural surface charge density is defined as:

$$Q_i = -FN_1 = -F\left(\{X\} + \{XNa^+\} + \{XH^+\}\right) \tag{3.24}$$

$$Q_i = -FN_1 = -F\left(\{X\} + \{XNa^+\} + \{XH^+\}\right) \tag{3.25}$$

$$Q_i = -FN_1 = -F\left(\{X\} + \{XNa^+\} + \{XH^+\}\right) \tag{3.26}$$

where $F$ is the Faraday constant, given in C/mol, and the surface charge density is:

$$Q_s = F\left(\{SOH_2^+\} - \{SO^-\} + \{XNa^+\} + \{XH^+\}\right) \tag{3.27}$$

$$Q_s = F\left(\{SOH_2^+\} - \{SO^-\} + \{XNa^+\} + \{XH^+\}\right) \tag{3.28}$$

As a consequence, the total surface charge density is the net sum of the two:

$$Q_0 = Q_s + Q_i = F\left(\{SOH_2^+\} - \{SO^-\} - \{X\}\right) \tag{3.29}$$

Finally, for surface charge to be balanced by the DDL, the following identity must be met:

$$Q_d = -Q_0 \tag{3.30}$$

where $Q_d$ is derived by the Gouy–Chapman theory:

$$Q_d = -\left(8000\varepsilon RT\right)^{1/2} I^{1/2} \sinh\left(\frac{F\varphi_d}{2RT}\right) \tag{3.31}$$

As discussed above, Equation 3.31 is only valid when the DDL is fully developed, i.e., there is no overlapping between DDLs surrounding opposite clay surfaces. The model also assumes that the surface plane and the diffuse layer plane are separated by a region of constant capacitance; thus:

$$\varphi_0 - \varphi_d = \frac{1}{C_{Str}} Q_0 \tag{3.32}$$

The set of Equations 3.18-3.28 is solved with the sorption sites as unknowns, along with Equation 3.29, 3.31, and 3.32 for $Q_0$, $Q_d$, $\varphi_0$ and $\varphi_d$, respectively

The set of equations above (3.18 through 3.32) can be solved for the case where Equation 3.31 applies. Unfortunately, Equation 3.31 holds whenever the DDL occupies a small portion of the pore space such that the bulk water properties ($\varphi = 0$) are present between the charged surfaces of the clay. That is not necessarily the case for highly compacted clays; on the contrary, the EDL affects concentrations and transport in the pore space in the case of the compacted clays and its geometry is in turn affected by the geometry of the pore structure.

The preceding paragraphs hint at the need for coupling the modules of solute transport and surface complexation reactions into a single, holistic model. As described above, such a model discretizes the pore space in terms of the predictable behavior ionic species, DDL, and pore architecture and is therefore more physically based than the somewhat ad hoc Donnan schemes.

From a mathematical standpoint, continuity should be assured for mass, namely, $C_i$, and the electric properties, $Q_d$ and $\varphi_d$, at the interface between the two domains (i.e., the so-called shear plane, which is the outer confine of the Stern layer), so that a constant feedback from one sub-domain (DDL, Stern layer) to the other is accounted for. This particular feature of the model is currently under development.

## 3.2.3 The Poisson–Nernst–Planck set of equations

### *3.2.3.1 Background*

The Poisson–Nernst–Planck set of equations is given by:

$$\begin{cases} \dfrac{\partial C_1}{\partial t} + \nabla \bullet \left( D_1 \nabla C_1 + D_1 \dfrac{F z_1}{RT} C_1 \nabla \varphi \right) = 0 \\ \dfrac{\partial C_2}{\partial t} + \nabla \bullet \left( D_2 \nabla C_2 + D_2 \dfrac{F z_2}{RT} C_2 \nabla \varphi \right) = 0 \\ \vdots \\ \dfrac{\partial C_N}{\partial t} + \nabla \bullet \left( D_N \nabla C_N + D_N \dfrac{F z_N}{RT} C_N \nabla \varphi \right) = 0 \\ \dfrac{F}{\varepsilon}\left( z_1 C_1 + z_2 C_2 + \ldots + z_N C_N \right) + \nabla^2 \varphi = 0 \end{cases} \tag{3.33}$$

where $C_i$, $z_i$, and $D_i$, for $i$ = 1, 2, …, $N$ (number of species), are, respectively, the concentration, valence and diffusion coefficient of the $i$-th ionic species, $\varphi$ is the electrical potential, $R$ is the universal gas constant, ε is the permittivity of the medium, and $T$ is the temperature.

The finite element scheme adopted in this work makes use of the variational approach, namely the Galerkin weighted residual method, of establishing the governing equilibrium equations of a system. Let $w$ be a weighting function; then the Nernst–Planck set of equations becomes:

$$\begin{aligned}
&\frac{\partial C_i}{\partial t}+D_i\frac{\partial^2 C_i}{\partial x^2}+D_i\frac{Fz_i}{RT}C_i\frac{\partial^2\varphi}{\partial x^2}=0\Rightarrow\\
&\int w\frac{\partial C_i}{\partial t}dx+D_i\int w\frac{\partial^2 C_i}{\partial x^2}dx+D_i\frac{Fz_i}{RT}\int wC_i\frac{\partial^2\varphi}{\partial x^2}dx=0\Rightarrow\\
&\int w\frac{\partial C_i}{\partial t}dx-D_i\int\frac{\partial w}{\partial x}\frac{\partial C_i}{\partial x}dx-D_i\frac{Fz_i}{RT}\int\frac{\partial wC_i}{\partial x}\frac{\partial\varphi}{\partial x}dx=-D_i\int w\frac{\partial C_i}{\partial n}d\Gamma-D_i\frac{Fz_i}{RT}\int wC_i\frac{\partial\varphi}{\partial n}d\Gamma
\end{aligned}\tag{3.34}$$

where, for the sake of simplicity, a one-dimensional case was considered.

Given that $\varphi$ and $\frac{\partial\varphi}{\partial n}$ are non–zero at the same boundary, namely the clay surface, then both terms on the right–hand side of the equation can be merged together. Therefore:

$$\int w\frac{\partial C_i}{\partial t}dx-D_i\int\frac{\partial w}{\partial x}\frac{\partial C_i}{\partial x}dx-D_i\frac{Fz_i}{RT}\int\frac{\partial wC_i}{\partial x}\frac{\partial\varphi}{\partial x}dx=-D_i\int w\left(\frac{\partial C_i}{\partial n}+\frac{Fz_i}{RT}C_i\frac{\partial\varphi}{\partial n}\right)d\Gamma\tag{3.35}$$

At the boundary the flux, $J$, is equal to zero, that is:

$$J_\Gamma=D_i\frac{\partial C_i}{\partial n}+D_i\frac{Fz_i}{RT}C_i\frac{\partial\varphi}{\partial n}\bigg|_\Gamma=0\Rightarrow D_i\left(\frac{\partial C_i}{\partial n}+\frac{Fz_i}{RT}C_i\frac{\partial\varphi}{\partial n}\right)\bigg|_\Gamma=0\tag{3.36}$$

As a consequence, when substituting into the Nernst–Planck set of equations, one obtains:

$$\int w\frac{\partial C_i}{\partial t}dx-D_i\int\frac{\partial w}{\partial x}\frac{\partial C_i}{\partial x}dx-D_i\frac{Fz_i}{RT}\int\frac{\partial wC_i}{\partial x}\frac{\partial\varphi}{\partial x}dx=0\tag{3.37}$$

as the right–hand side of the equation vanishes.

Analogously, for the one-dimensional form of the Poisson equation:

$$\begin{aligned}
&\frac{\partial^2\varphi}{\partial x^2}=-\frac{F}{\varepsilon}\sum_i z_iC_i\Rightarrow\\
&\int w\frac{\partial^2\varphi}{\partial x^2}dx=-\frac{F}{\varepsilon}\sum_i z_i\int wC_idx\Rightarrow\\
&\int\frac{\partial w}{\partial x}\frac{\partial\varphi}{\partial x}dx-\frac{F}{\varepsilon}\sum_i z_i\int wC_idx=\int w\frac{\partial\varphi}{\partial n}d\Gamma
\end{aligned}\tag{3.38}$$

At the boundary, both the electrical potential and the surface charge are non-zero and interdependent. It can be assumed that a linear relationship exists between the potential and its gradient, namely:

$$\alpha\frac{\partial\varphi}{\partial n}=\varphi-\varphi_0 \tag{3.39}$$

for a given value of $\varphi$.

Substituting into the Poisson equation yields:

$$\int\frac{\partial w}{\partial x}\frac{\partial\varphi}{\partial x}dx-\frac{F}{\varepsilon}\sum_i z_i\int wC_i dx=\frac{1}{\alpha}\int w\varphi d\Gamma-\frac{1}{\alpha}\int w\varphi_0 d\Gamma \tag{3.40}$$

#### 3.2.3.2 *Finite element formulation*

Using a finite element approach, the Nernst–Planck set of equations becomes:

$$\begin{aligned}
&\int w\frac{\partial C_i}{\partial t}dx-D_i\int\frac{\partial w}{\partial x}\frac{\partial C_i}{\partial x}dx-D_i\frac{Fz_i}{RT}\int\frac{\partial wC_i}{\partial x}\frac{\partial\varphi}{\partial x}dx=\\
&-D_i\int w\left(\frac{\partial C_i}{\partial n}+\frac{Fz_i}{RT}C_i\frac{\partial\varphi}{\partial n}\right)d\Gamma\Rightarrow\\
&\left(\int\underline{H}^T\underline{H}dx\right)\frac{\partial\underline{\hat{C}}_i}{\partial t}-D_i\left(\int\underline{B}^T\underline{B}dx\right)\underline{\hat{C}}_i-2D_i\frac{Fz_i}{RT}\left(\int\underline{H}^T\underline{\hat{C}}_i\underline{B}^T\underline{B}dx\right)\underline{\hat{\varphi}}=\\
&-D_i\int\underline{H}^T\left(\frac{\partial\underline{H}}{\partial n}\underline{\hat{C}}_i+\frac{Fz_i}{RT}\underline{H}^T\underline{\hat{C}}_i\frac{\partial\underline{H}}{\partial n}\underline{\hat{\varphi}}\right)d\Gamma
\end{aligned} \tag{3.41}$$

which for both off– and on–boundary nodes results in:

$$\left(\int\underline{H}^T\underline{H}dx\right)\frac{\partial\underline{\hat{C}}_i}{\partial t}-D_i\left(\int\underline{B}^T\underline{B}dx\right)\underline{\hat{C}}_i-2D_i\frac{Fz_i}{RT}\left(\int\underline{H}^T\underline{\hat{C}}_i\underline{B}^T\underline{B}dx\right)\underline{\hat{\varphi}}=0 \tag{3.42}$$

Similarly, the Poisson equation takes the following form:

$$\left(\int\underline{B}^T\underline{B}dx\right)\underline{\hat{\varphi}}-\frac{F}{\varepsilon}\sum_i z_i\left(\int\underline{H}^T\underline{H}dx\right)\underline{\hat{C}}_i=\left(\int\underline{H}^T\frac{\partial\underline{H}}{\partial n}d\Gamma\right)\underline{\hat{\varphi}} \tag{3.43}$$

So, for all off–boundary nodes:

$$\left(\int\underline{B}^T\underline{B}dx\right)\underline{\hat{\varphi}}-\frac{F}{\varepsilon}\sum_i z_i\left(\int\underline{H}^T\underline{H}dx\right)\underline{\hat{C}}_i=0 \tag{3.44}$$

and for on-boundary nodes:

$$\left(\int\underline{B}^T\underline{B}dx\right)\underline{\hat{\varphi}}-\frac{F}{\varepsilon}\sum_i z_i\left(\int\underline{H}^T\underline{H}dx\right)\underline{\hat{C}}_i=\frac{1}{\alpha}\left(\int\frac{\partial\underline{H}^T}{\partial n}d\Gamma\right)\underline{\hat{\varphi}}-\frac{1}{\alpha}\left(\int\frac{\partial\underline{H}^T}{\partial n}d\Gamma\right)\varphi_0 \tag{3.45}$$

and regrouping:

$$\left[\left(\int\underline{B}^T\underline{B}dx\right)-\frac{1}{\alpha}\left(\int\underline{H}^T\frac{\partial\underline{H}}{\partial n}d\Gamma\right)\right]\underline{\hat{\varphi}}-\frac{F}{\varepsilon}\sum_i z_i\left(\int\underline{H}^T\underline{H}dx\right)\underline{\hat{C}}_i=-\frac{1}{\alpha}\left(\int\underline{H}^T\frac{\partial\underline{H}}{\partial n}d\Gamma\right)\varphi_0 \tag{3.46}$$

So, in matrix notation:

$$\underline{\underline{M}} = \int \underline{H}^T \underline{H} dx \tag{3.47}$$

$$\underline{\underline{K}}_{D_i} = -D_i \int \underline{B}^T \underline{B} dx \tag{3.48}$$

$$\underline{\underline{K}}_{D_i nl} = -2D_i \frac{F z_i}{RT} \left( \int \underline{H}^T \underline{\widehat{C}}_i \underline{B}^T \underline{B} dx \right) \tag{3.49}$$

$$\underline{\underline{K}} = \int \underline{B}^T \underline{B} dx \tag{3.50}$$

$$\underline{\underline{M}}_{z_i} = -\frac{F}{\varepsilon} z_i \int \underline{H}^T \underline{H} dx \tag{3.51}$$

$$\underline{\underline{B}} = -\left( \int \underline{H}^T \frac{\partial \underline{\underline{H}}}{\partial n} d\Gamma \right) \tag{3.52}$$

$$\left[ \left( \int \underline{B}^T \underline{B} dx \right) - \frac{1}{\alpha} \left( \int \frac{\partial \underline{H}^T}{\partial n} d\Gamma \right) \right] \underline{\widehat{\varphi}} - \frac{F}{\varepsilon} \sum_i z_i \left( \int \underline{H}^T \underline{H} dx \right) \underline{\widehat{C}}_i = -\frac{1}{\alpha} \left( \int \frac{\partial \underline{H}^T}{\partial n} d\Gamma \right) \varphi_0 \tag{3.53}$$

For off–boundary nodes, this yields:

$$\begin{pmatrix} M & 0 & \cdots & 0 & 0 \\ 0 & M & \cdots & 0 & 0 \\ \vdots & \vdots & \ddots & 0 & \vdots \\ 0 & 0 & \cdots & M & 0 \\ 0 & 0 & \cdots & 0 & 0 \end{pmatrix} \frac{1}{\Delta t} \left( C^{t+\Delta t} - C^t \right) + \begin{pmatrix} K_{D_1} & 0 & \cdots & 0 & K_{D_1 nl} \\ 0 & K_{D_2} & \cdots & 0 & K_{D_2 nl} \\ \vdots & \vdots & \ddots & 0 & \vdots \\ 0 & 0 & \cdots & K_{D_N} & K_{D_N nl} \\ M_{z_1} & M_{z_2} & \cdots & M_{z_N} & K \end{pmatrix} C^{t+\Delta t} = \begin{pmatrix} 0 \\ 0 \\ \vdots \\ 0 \\ 0 \end{pmatrix} \tag{3.54}$$

For on–boundary nodes, this yields:

$$\begin{pmatrix} M & 0 & \cdots & 0 & 0 \\ 0 & M & \cdots & 0 & 0 \\ \vdots & \vdots & \ddots & \vdots & \vdots \\ 0 & 0 & \cdots & M & 0 \\ 0 & 0 & \cdots & 0 & 0 \end{pmatrix} \frac{1}{\Delta t} \left( C^{t+\Delta t} - C^t \right) + \begin{pmatrix} K_{D_1} & 0 & \cdots & 0 & K_{D_1 nl} \\ 0 & K_{D_2} & \cdots & 0 & K_{D_2 nl} \\ \vdots & \vdots & \ddots & 0 & \vdots \\ 0 & 0 & \cdots & K_{D_N} & K_{D_N nl} \\ M_{z_1} & M_{z_2} & \cdots & M_{z_N} & \left( K + \frac{1}{\alpha} B \right) \end{pmatrix} C^{t+\Delta t} = \begin{pmatrix} 0 \\ 0 \\ \vdots \\ 0 \\ \frac{1}{\alpha} B \varphi_0 \end{pmatrix} \tag{3.55}$$

so that when $\alpha$ is small, $\underline{\underline{B}}$ becomes dominant over the remaining elements of the equation, with the result that $\widehat{\varphi} = \varphi_0$, i.e., it becomes a boundary condition of the Dirichlet type. On the other hand, when $\alpha$ is large, then $\dfrac{\partial \varphi}{\partial n}$ tends progressively towards 0, which is a boundary condition of the Neumann type:

$$\begin{pmatrix} K_{D_1} & 0 & \cdots & 0 & K_{D_1 nl} \\ 0 & K_{D_2} & \cdots & 0 & K_{D_2 nl} \\ \vdots & \vdots & \ddots & 0 & \vdots \\ 0 & 0 & \cdots & K_{D_N} & K_{D_N nl} \\ M_{z_1} & M_{z_2} & \cdots & M_{z_N} & \left( K + \dfrac{1}{\alpha} B \right) \end{pmatrix} C^{t+\Delta t} = \begin{pmatrix} 0 \\ 0 \\ \vdots \\ 0 \\ \dfrac{1}{\alpha} B \varphi_0 \end{pmatrix} \tag{3.56}$$

### 3.2.3.3 Calibration

A code was developed for the resolution of the PNP set of equations under a two-dimensional finite-element framework. To evaluate its performance, a relatively simple 1D case was chosen for which other numerical solutions are known.

Figure 3.3 shows the results provided by the code along with those obtained by CrunchFlow (Steefel, 2009) for a simple one-dimensional problem developed originally by Lichtner (1998). In this problem, $Na^+$ and $Cl^-$ are present at 0.1 mM in both the internal domain and at the boundary on the left. However, the concentrations of $H^+$ and $NO3^-$ are different between the boundary (0.001 mM and pH 6) and the internal domain (0.1 mM and pH 4). Without coupling and using only Fick's Law, the sodium and chloride profile should remain flat, but the electrochemical migration flux (Steefel and Maher, 2009) causes fluxes of both of these as the hydrogen ion diffuses more rapidly than the nitrate out of the system. As can be seen, the agreement is excellent, as the code reproduces the electrical interaction of ionic species induced by the differing diffusion coefficients once a concentration gradient is introduced.

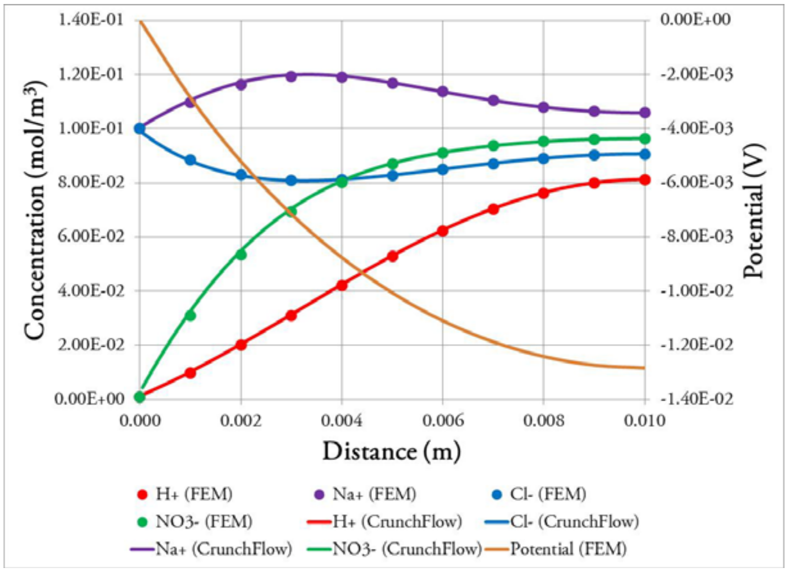

Figure 3.3. Results obtained by the PNP set of equations under a 2D finite element scheme (dotted lines), as compared to those provided by CrunchFlow (solid lines).

### 3.2.3.4 *Special case: The Poisson–Boltzmann equation*

Let us consider a binary solution under steady-state conditions. Then, the system can be described by the following set of equations:

$$\begin{cases} \dfrac{\partial C_1}{\partial x} + \dfrac{F}{RT} z_1 C_1 \dfrac{\partial \varphi}{\partial x} = 0 \\ \dfrac{\partial C_2}{\partial x} + \dfrac{F}{RT} z_2 C_2 \dfrac{\partial \varphi}{\partial x} = 0 \\ \dfrac{\partial^2 \varphi}{\partial x^2} + \dfrac{F}{\varepsilon}\left(z_1 C_1 + z_2 C_2\right) = 0 \end{cases} \tag{3.57}$$

as the partial time derivatives go to zero.

Assuming that the solution to the set of equations is

$$\begin{gathered} C_1 = C_{1,\infty} \exp\left(-z_1 \frac{F\varphi}{RT}\right) \\ C_2 = C_{2,\infty} \exp\left(-z_2 \frac{F\varphi}{RT}\right) \end{gathered} \tag{3.58}$$

then

$$\begin{gathered} \frac{\partial C_1}{\partial x} = \frac{\partial C_1}{\partial \varphi}\frac{\partial \varphi}{\partial x} = -z_1 \frac{F}{RT} C_{1,\infty} \exp\left(-z_1 \frac{F\varphi}{RT}\right)\frac{\partial \varphi}{\partial x} \\ \frac{\partial C_2}{\partial x} = -z_2 \frac{F}{RT} C_{2,\infty} \exp\left(-z_2 \frac{F\varphi}{RT}\right)\frac{\partial \varphi}{\partial x} \end{gathered} \tag{3.59}$$

Substituting into the set of equations yields:

$$\begin{cases} -z_1 \dfrac{F}{RT} C_{1,\infty} \exp\left(-z_1 \dfrac{F\varphi}{RT}\right) \dfrac{\partial \varphi}{\partial x} + \dfrac{F}{RT} z_1 C_{1,\infty} \exp\left(-z_1 \dfrac{F\varphi}{RT}\right) \dfrac{\partial \varphi}{\partial x} = 0 \\ -z_2 \dfrac{F}{RT} C_{2,\infty} \exp\left(-z_2 \dfrac{F\varphi}{RT}\right) \dfrac{\partial \varphi}{\partial x} + \dfrac{F}{RT} z_2 C_{2,\infty} \exp\left(-z_2 \dfrac{F\varphi}{RT}\right) \dfrac{\partial \varphi}{\partial x} = 0 \\ \dfrac{\partial^2 \varphi}{\partial x^2} + \dfrac{F}{\varepsilon}\left[ z_1 C_{1,\infty} \exp\left(-z_1 \dfrac{F\varphi}{RT}\right) + z_2 C_{2,\infty} \exp\left(-z_2 \dfrac{F\varphi}{RT}\right)\right] = 0 \end{cases} \qquad (3.60)$$

The first two identities are true, whereas the third one is the Poisson–Boltzmann equation. As a consequence, it can be stated that, under a consistent set of boundary conditions, the Poisson–Boltzmann equation represents the solution of the PNP set of equations for the steady state. This is relevant for the determination of the initial conditions of a given problem, since even before a concentration gradient is introduced, a pre-existing, non-uniform spatial distribution of the species should be observable by virtue of the electric potential emanating from the charged clay surfaces.

In keeping with the notation of the preceding section, the determination of the initial conditions entails that the Poisson–Boltzmann equation has to be solved. That means that a solution has to be found for the set of equations given by:

$$\begin{pmatrix} K_{D_1} & 0 & \cdots & 0 & K_{D_1 nl} \\ 0 & K_{D_2} & \cdots & 0 & K_{D_2 nl} \\ \vdots & \vdots & \ddots & 0 & \vdots \\ 0 & 0 & \cdots & K_{D_N} & K_{D_N nl} \\ M_{z_1} & M_{z_2} & \cdots & M_{z_N} & K \end{pmatrix} C = \begin{pmatrix} 0 \\ 0 \\ \vdots \\ 0 \\ 0 \end{pmatrix} \qquad (3.61)$$

which is valid for off–boundary nodes. And for on–boundary nodes:

$$\begin{pmatrix} K_{D_1} & 0 & \cdots & 0 & K_{D_1 nl} \\ 0 & K_{D_2} & \cdots & 0 & K_{D_2 nl} \\ \vdots & \vdots & \ddots & 0 & \vdots \\ 0 & 0 & \cdots & K_{D_N} & K_{D_N nl} \\ M_{z_1} & M_{z_2} & \cdots & M_{z_N} & \left(K + \dfrac{1}{\alpha} B\right) \end{pmatrix} C = \begin{pmatrix} 0 \\ 0 \\ \vdots \\ 0 \\ \dfrac{1}{\alpha} B \varphi_0 \end{pmatrix} \qquad (3.62)$$

In the following, a simple case of a binary solution in compacted clay will be considered with the aim of demonstrating the applicability of the Poisson–Boltzmann equation (and, by extension, of the PNP set of equations) for the description of the spatial distribution ionic species concentrations in the pore space.

Figure 3.4 shows an example 2D calculation with the electrical potential field using the numerical PNP approach in which the differing diffusion rates of the ionic species is combined with a transverse (perpendicular to the charged clay surfaces) calculation of the electrical potential and flux. The boundary conditions at the clay surfaces are no-flux for the species concentrations and Dirichlet for the electrical potential, with a value of -0.12 Volts assumed.

After ten days of diffusion down the length of the clay interlamellae (X-coordinate), the electrical potential shows a curved front due to the effects of the negatively charged clay surface at the top and bottom.

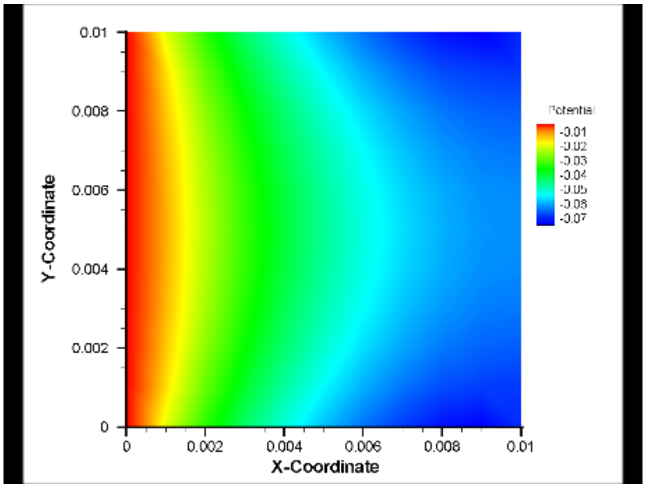

Figure 3.4. Example 2D calculation of electrical potential field for the case where the charged clay surfaces (top and bottom) have a -0.12 V charge.

### 3.2.4 Comparison to Van Loon et al. (2007) Diffusion Data

For such a case, it should be proved that the anion concentration, $C(x,y,z)$ integrated over the pore space should equal that measured experimentally:

$$\int_{V_P} C(x,y,z)\,dV = \left[A^-\right]\varepsilon_{A^-}V_T \tag{3.63}$$

where $V_T$ is the total volume of a given clay sample whose porosity is $\phi$, $V_P = \phi V_T$ is its volume of pores, $\left[A^-\right]$ is the concentration of anions in solution at the outlet of the sample, and $\varepsilon_{A^-}$ is the so-called anion-accessible porosity (Van Loon et al., 2007).

Considering the case of a solution confined between two parallel charged walls, the Poisson–Boltzmann equation takes the following form:

$$\frac{d^2\varphi}{dy^2} = \frac{2FC_\infty}{\varepsilon}\sinh\left(\frac{F\varphi}{RT}\right) \tag{3.64}$$

Incorporating the steric correction, which accounts for the constraint to the space physically available to ions in highly concentrated solutions, the expression above becomes:

$$\frac{d^2\varphi}{dy^2} = \frac{2FC_\infty}{\varepsilon}\frac{\sinh\left(\frac{F\varphi}{RT}\right)}{1+4\frac{C_\infty}{C_{\max}}\sinh^2\left(\frac{F\varphi}{2RT}\right)} \tag{3.65}$$

where $C_{\max}$ represents the maximum possible concentration for a given ion size in solution. It becomes apparent that this equation recovers its original form when $C_{\max} \rightarrow \infty$.

Under the hypothesis that the pore space is constituted by a number of layers of thickness $h$, the total amount of anions in one such layer is:

$$Total\ mass\ per\ layer = \int_0^h C(r)\,dr = C_\infty \int_0^h \exp\left(\frac{F\varphi(r)}{RT}\right) dr = G(h) \tag{3.66}$$

where $\varphi(r)$ is the solution of the Poisson–Boltzmann equation ($r$ is a dummy variable), and the total mass is written explicitly as a function of $h$.

It is worth pointing out that $G(h)$ equals zero when $h$ is less than the threshold marking the transition between innercrystalline and interlamellar water, which is on the order of 0.94 nm (Tournassat and Appelo, 2011).

Assuming that the sizes of clay pores are uniform, then the anion concentration is simply:

$$\left[A^-\right]_{calc} = \frac{G(h_{med})}{h_{med}} \tag{3.67}$$

where $h_{med}$ is the average pore thickness.

Numerical results were compared to experimental data provided by Van Loon et al. (2007). In the process, the values of the surface electrical potential, the average pore thickness, and the effective hard-sphere packing length were adjusted to obtain the best fit (Table 3.1).

Table 3.3. Parameters used during the fitting of Van Loon et al (2007) data.

| **Dry density (kg/m$^3$)** | **Surface potential (V)** | **Effective hard-sphere packing length (m)** | **Pore thickness (m)** |
|---|---|---|---|
| 1300 | -0.12 | 5.00E-10 | 3.00E-09 |
| 1600 | -0.12 | 5.00E-10 | 1.40E-09 |
| 1900 | -0.12 | 5.00E-10 | 1.00E-09 |

Results obtained for best-fit values are shown in Figure 3.5

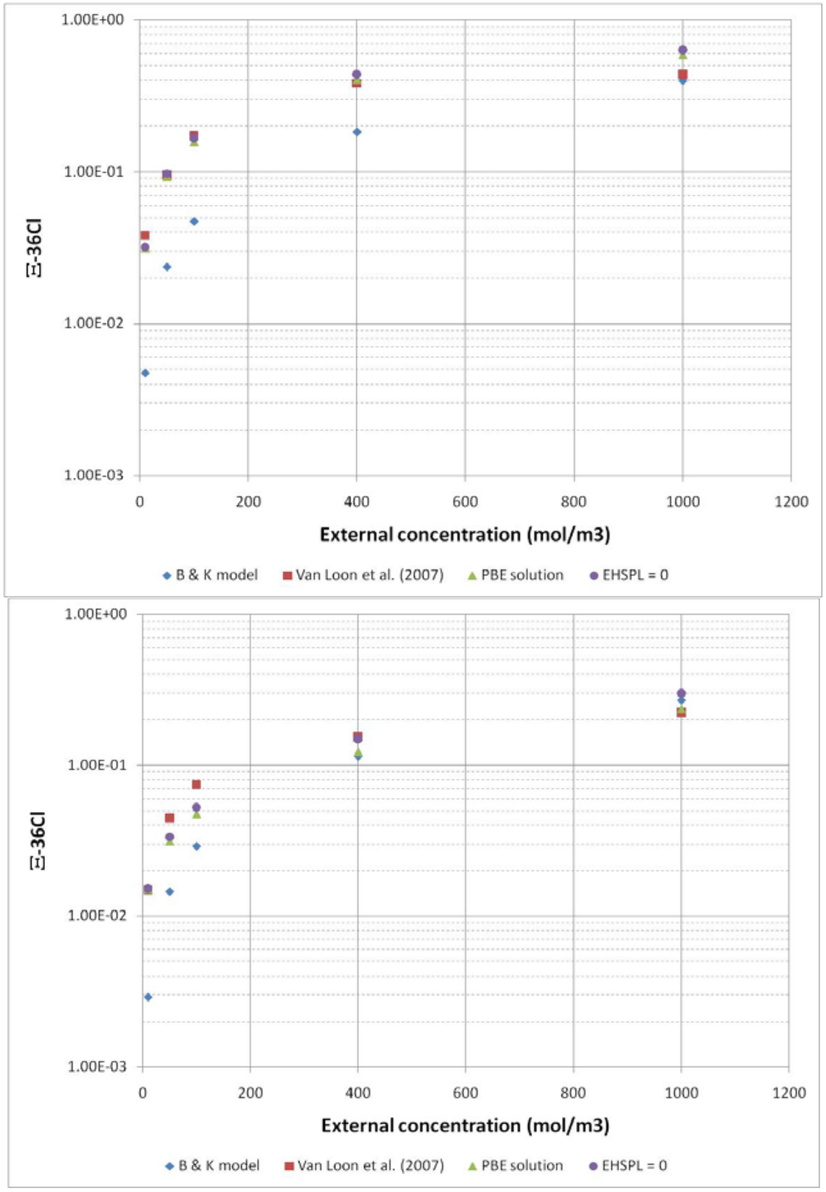
1.00E+00
1.00E-01
1.00E-02
1.00E-03
Ξ-36Cl
0
200
400
600
800
1000
1200
External concentration (mol/m3)
◆ B & K model
■ Van Loon et al. (2007)
▲ PBE solution
● EHSPL = 0
1.00E+00
1.00E-01
1.00E-02
1.00E-03
Ξ-36Cl
0
200
400
600
800
1000
1200
External concentration (mol/m3)
◆ B & K model
■ Van Loon et al. (2007)
▲ PBE solution
● EHSPL = 0

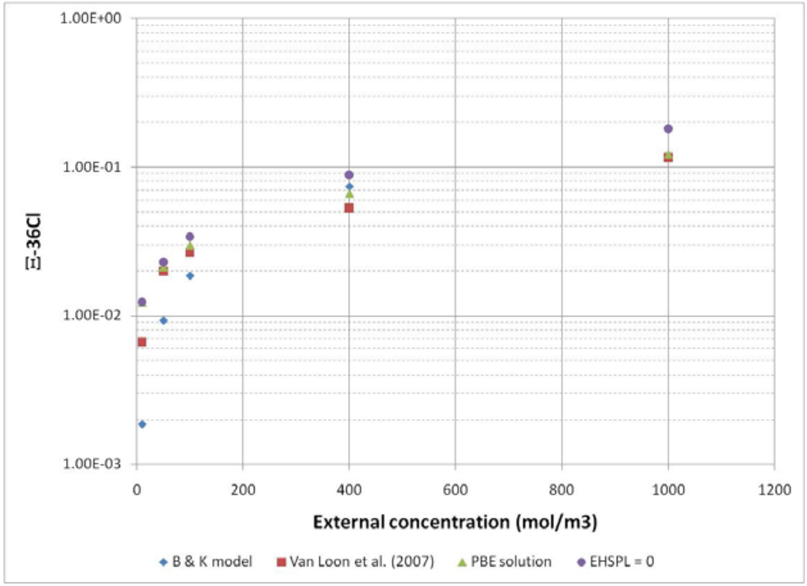

Figure 3.5. Chloride concentration ratios as a function of dry density and ionic strength of the external solution (from top to bottom: results obtained for dry density equal to 1300 kg/m$^3$, 1600 kg/m$^3$ and 1900 kg/m$^3$)

As can be seen, the results obtained provide a good approximation to experimental data for all the dry density values considered. They even improve upon the predictions of the Birgersson and Karnland model, as shown in the diagram above. Moreover, the calculated average pore thickness is consistent with the values calculated by Tournassat and Appelo (2011) for the range of dry density values below approximately 1600 kg/m$^3$. For higher dry density values, however, the total pore volume is reduced to such an extent that the calculated average interlamellar distance is less than the fitted $h_{med}$ that is shown in the table above and, in fact, even less than the maximum innercrystalline spacing (the above-mentioned threshold of 0.94 nm). Since anions are completely excluded from the innercrystalline pore space, it follows that for dry densities higher than 1600 kg/m$^3$, the concentration of anions in clay should be nil. As noted by Tournassat and Appelo (2011), this contradicts experimental evidence. Based on this, it is suggested that the assumption of the pore space being uniformly distributed is not correct.

In contrast to the assumption of a uniform pore distribution, we assume in what follows that the pore size distribution of clays obeys a fractal law, such that the following number-size relationship holds (Mandelbrot, 1999):

$$N\left(L\right) = kL^{-D} \qquad (3.68)$$

where $N\left(L\right)$ is the number of elements of size equal to or less than a given characteristic length $L$, $D$ is the fractal dimension and $k$ is a constant of proportionality.

Fractal theory has been used for the description of the pore-size distribution of soils and its related hydraulic, mechanical, and surface properties (Xu, 2004; Xu et al., 2004; Xu and Xia, 2006; Ersahin et al., 2006, among others). In most cases, however, the characteristic length considered was the radius of pores. An original contribution of the present study is to insert the interlamellar distance into the relationship above, namely:

$$N\left(L\right)=kL^{-D} \tag{3.69}$$

where $h$ varies between 0 and a maximum thickness, $h_{\max}$, which corresponds to the total porosity of the sample.

If one further assumes that, as Viani et al. (1983) put it, “Clay minerals normally occur as crystals of colloidal size in which parallel silicate layers are stacked one above the other like the leaves of a book” (which in itself supports the hypothesis of $h$ being described as a fractal, since a fractal is a shape made of parts similar to the whole in some way), then it becomes apparent that the total pore space should be proportional to the number of spaces between those leaves and to the distance between them, which means that:

$$V_P \;\alpha \sum_{i=1}^{N} N_i h_i \tag{3.70}$$

Let us assume a parallelepipedic sample of perfectly flat layered clay whose sides in the $x$- and $y$-directions are $B$ and $L$, respectively. For such a case, the total pore space is given by:

$$V_P = BL\sum_{i=1}^{N} N_i h_i \tag{3.71}$$

In a more general, less restrictive, case, we suggest here that the factor $BL$ can be replaced by a shape factor, $\xi$, which condenses the information related not only to the geometrical shape of the sample, but also (in keeping with the image depicted by Viani et al., 1983) the information about how flat or bent the leaves are.

The number of layers being continuous rather than discrete, then the summation becomes an integral:

$$V_P = \xi\int_0^{\infty} h\,dN \tag{3.72}$$

Differentiating $N$ from the number-size relationship and performing the integral, one obtains:

$$\begin{aligned} &V_P = \xi\int_0^{\infty} h\,dN = -\xi Dk\int_{h_{\max}}^{0} h^{-D}dh = \xi Dk\frac{1}{1-D}h_{\max}^{1-D} \Rightarrow \\ &h_{\max} = \left[\left(1-D\right)\frac{\phi V_T}{\xi Dk}\right]^{\frac{1}{1-D}} \end{aligned} \tag{3.73}$$

Analogously, the total amount of anions in the clay sample can be calculated in terms of the mass of each interlamellar space, as shown above:

$$\begin{aligned} &Total\,mass = \xi\int_0^{\infty} G\left(h\right)dN = -\xi\int_{h_{\max}}^{0} G\left(h\right)Dkh^{-D-1}dh = \\ &-\xi\int_{h_{\min}}^{0} G\left(h\right)Dkh^{-D-1}dh - \xi\int_{h_{\max}}^{h_{\min}} G\left(h\right)Dkh^{-D-1}dh = \xi\int_{h_{\min}}^{h_{\max}} G\left(h\right)Dkh^{-D-1}dh \end{aligned} \tag{3.74}$$

because, as discussed above, the integral vanishes between 0 and $h_{\min}$ = 0.94 nm.

The integral can be calculated numerically by making use of a Gaussian quadrature rule, according to which the following equation is valid:

$$\xi\int_{h_{\min}}^{h_{\max}} G(h)Dkh^{-D-1}dh = \sum_{j=1}^{n} w_i \xi G(h_i) Dkh_i^{-D-1} \tag{3.75}$$

where $n$ is the number of integration points and $w_i$ are the corresponding weighting factors.

Several simulations were performed in order to find the combination of the factor $\xi k$ and the fractal dimension $D$ that minimizes the error made with respect to the total amount of anions measured experimentally. Let the error be defined as:

$$Error = \sum_{i=1}^{5}\left(\frac{CalcMass_i - ExpMass_i}{ExpMass_i}\right)^2 \tag{3.76}$$

where $CalcMass_i$ and $ExpMass_i$ represent the total amount of anions calculated and experimentally measured, respectively, for a given value of the ionic strength of the external solution. The summation has as many terms as ionic strength values considered.

Figure 3.6 display the error made as a function of the fractal dimension and the shape factor (assuming $k$ is equal to one).

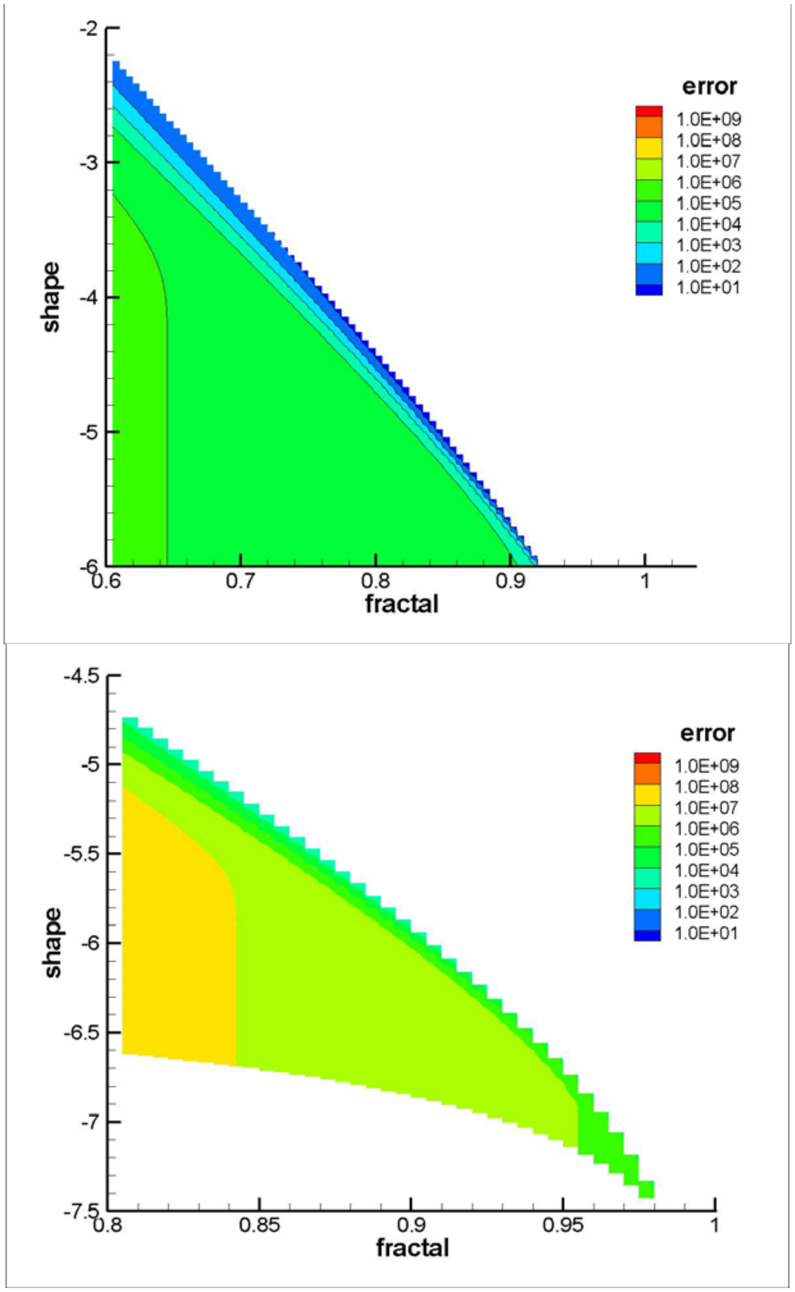

Figure 3.6. Error as a function of the combination of the fractal dimension and the shape factor

Some comments are worth making concerning Figure 3.6. The values of $h_{\max}$ calculated increase from the upper right towards the lower left of the diagrams, so that the points of that region correspond to the case where the calculated $h_{\max}$ is less than $h_{\min}$ and thus were thus deemed irrelevant. Furthermore, the minimum errors are confined to a very small range of $h_{\max}$ very close in value to $h_{\min}$, but this is perhaps what might be expected when dealing with highly compacted clays. Best-fit values are summarized in Table 3.4.

Table 3.4. Parameters used during the fitting procedure of fractal behavior

| **Dry density (kg/m$^3$)** | **Fractal dimension** | **Log($\xi$)** |
|---|---|---|
| 1300 | 0.875 | -5.400 |
| 1600 | 0.960 | -6.730 |
| 1900 | 0.980 | -7.330 |

Results that take into account the values listed in Table 3.4 with a non-uniform clay interlamellae spacing are shown in the following figures.

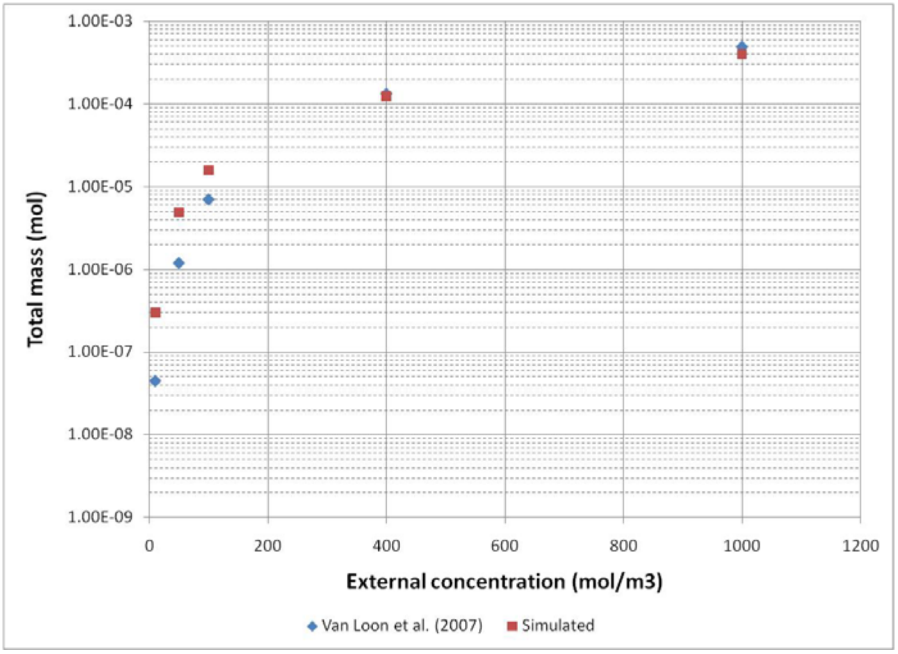

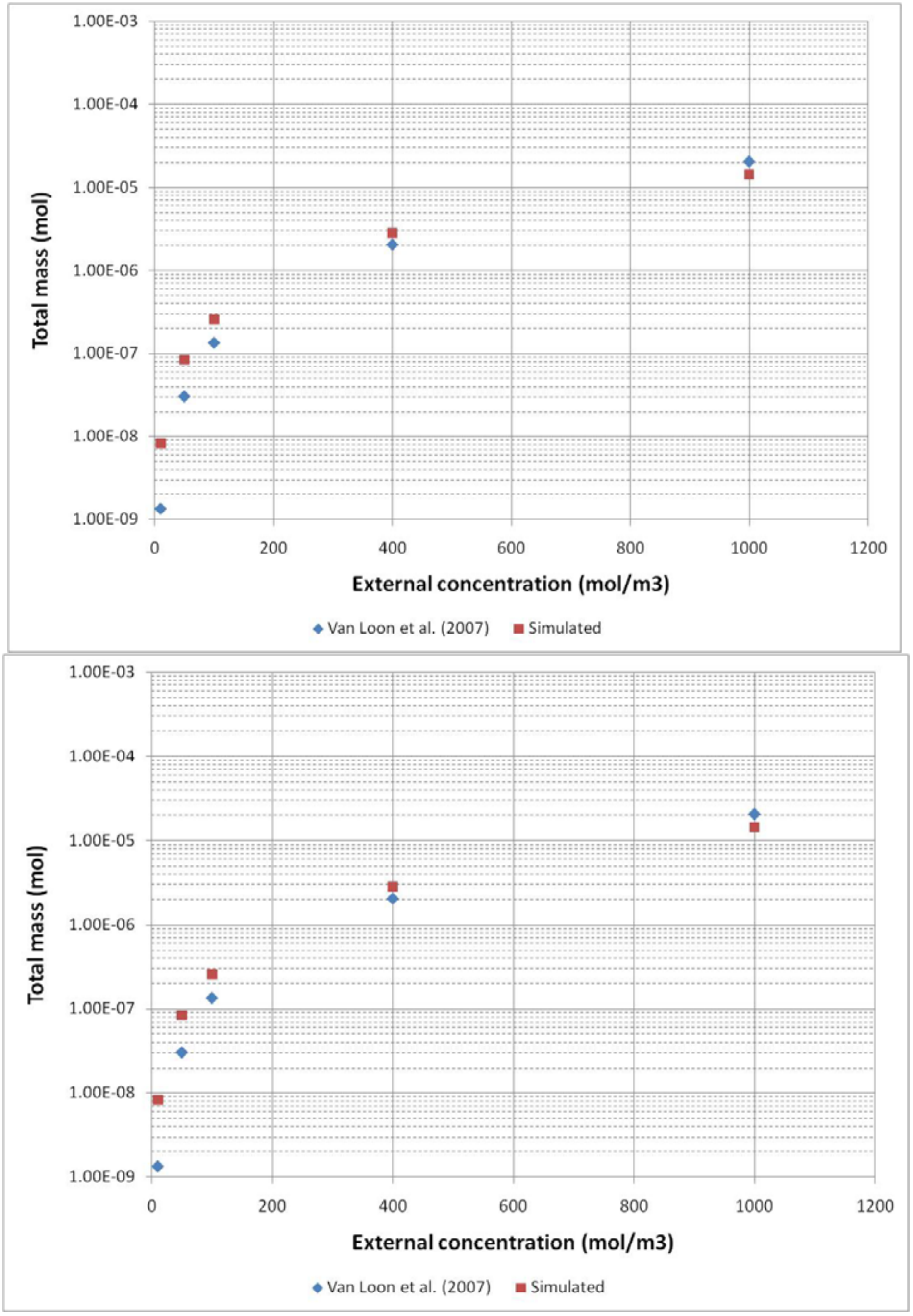

Figure 3.7. Chloride total mass as a function of dry density and ionic strength of the external solution (from top to bottom: Results obtained for dry density equal to 1300 kg/m$^3$, 1600 kg/m$^3$ and 1900 kg/m$^3$), based on fractal values in Table 3-4

As Figure 3.7 demonstrates, the agreement with experimental data is satisfactory even though values of $D$ and Log($\xi$) that were tested were restricted to rational numbers. The solutions shown above, however, may not be unique, which suggests that an additional constraint may be required. In this regard, the analysis of swelling pressure might provide the needed constraint. Unfortunately, Van Loon et al. (2007) do not provide such data.

## 3.3 Conclusions

A conceptual model involving the coupling of the Poisson-Nernst-Planck set of equations with a suitable surface complexation model was presented as an attempt to bridge the gap between nanofluidic dynamics and clay science.

Even though the practical features of the model are currently under development, the evidence collected so far allows us to state that it has great potential for the simulation of solute transport in such media because it is more physically grounded than previous models. Good agreement with available experimental data gives further support to such a claim. Indeed, the spatial distribution of the electric potential and the concentration of every species of the geochemical system were simulated, and a good fit of experimental data was found over a wider range of external conditions than is possible with the Donnan-based models.

In addition, the present study is able to reconcile the theory of the Poisson–Boltzmann equation with seemingly conflicting experimental evidence of non-zero anion concentrations found in highly compacted clays by making use of the theory of fractals. If proved suitable, that would have relevant implications for the process of upscaling results from the nano- up to macro-scales based on the self-similarity of the fractal structure of clays.

# 4. MOLECULAR DYNAMICS (MD) SIMULATIONS OF ION DIFFUSION IN MONTMORILLONITE INTERLAYER NANOPORES

Considering that EBS is subject to substantial temperature variations, the objective of our MD simulations is to predict the temperature dependence of water and solute diffusion coefficients ($D$) in clay interlayer nanopores as characterized by the phenomenological activation energy $E_A$ (kJ mol$^{-1}$) of the Arrhenius relation: $\ln D \propto -E_A/RT$, where $R$ is the ideal gas constant and $T$ is absolute temperature. We aim to predict $E_A$ in *individual nanopores* with sufficient accuracy to aid in the interpretation of experimental data on $E_A$ in *macroscopic* (cm-scale) samples of compacted montmorillonite (MMT) (Kozaki et al., 1996,1998,1999,2005,2008). For a variety of ionic solutes ($Na^+$, $Ca^{2+}$, $Cs^+$, $Cl^-$) diffusing in macroscopic (cm-scale) samples of compacted Na-MMT, $E_A$ takes three distinct values, suggestive of three distinct diffusion pathways or mechanisms, with increasing compaction. In the case of $Na^+$, for example, $E_A$ equals ~18.5 ± 1.5 kJ mol$^{-1}$ (consistent with the value in bulk liquid water) at low dry bulk densities ($\leq$ 0.8 kg dm$^{-3}$), decreases to ~15.5 ± 1.5 kJ mol$^{-1}$ at intermediate dry bulk densities (0.9 to 1.2 kg dm$^{-3}$), and increases to ~25 ± 2 kJ mol$^{-1}$ at high dry bulk densities ($\geq$ 1.6 kg dm$^{-3}$) (Kozaki et al., 2005). It will be possible to use these results to determine activation energies for diffusion through the compacted bentonite in larger (repository) scale models as a function of the evolving temperature field. In the nearer term, these activation energies will be used as input for microscopic continuum models of the kind described in Section 3.

As a necessary first step of our simulations, we conducted a series of simulations of the three-layer hydrate of Na-MMT (Figure 4.1) aimed at developing a best-practice methodology for predicting $D$ and $E_A$ values of interlayer solutes in smectite interlayers using MD simulations. A thorough sensitivity analysis was found necessary in order to accurately predict self-diffusion coefficients over a wide range of temperatures, i.e., to accurately mimic the temperature dependence of experimental self-diffusion coefficients. For our sensitivity analysis, we investigated the influence of three methodological choices (the rigidity of the clay structure, the size of the simulated system, and the water content per clay unit cell) as described in the next paragraph. At each condition, we investigated four temperatures (278 to 353 K) to determine the activation energy of sodium and water diffusion. In order to determine the accuracy of our predicted self-diffusion coefficients, we also simulated "homogenous" systems without smectite, i.e., $Na^+$ ions in bulk water.

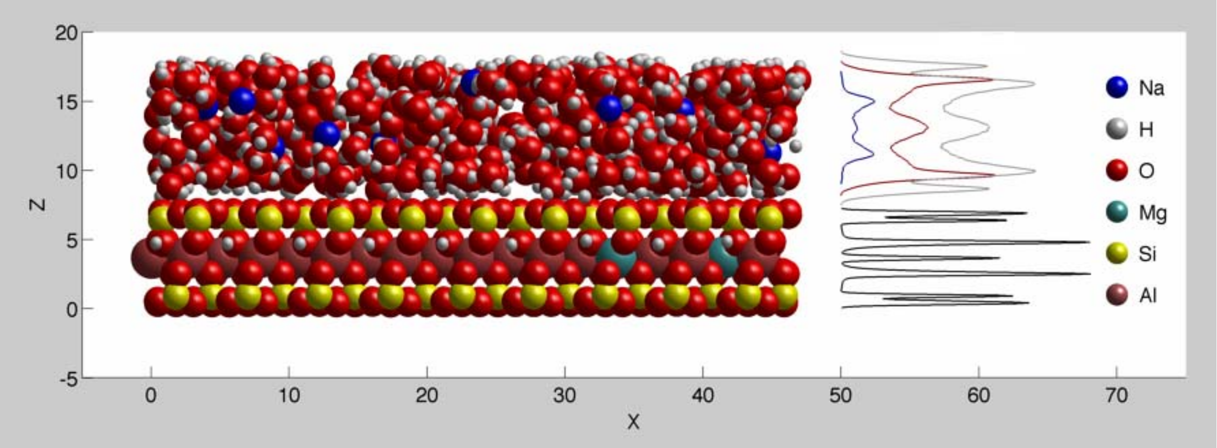

Figure 4.1. Illustration showing a typical MMT lamella of size ~45×45×1 nm in the three-layer hydrate (expected to be the predominant hydration state in the bentonite barrier in different concepts of geological nuclear waste disposal, such as the Swedish KBS-3 concept (Holmboe et al., 2012) with a basal spacing (total MMT + $H_2O$ thickness) of 1.89 nm. The figure shows a "snapshot" of the interlayer water and sodium, whereas clay atoms (Al, Si, Mg, O, H) are displayed at their time-averaged coordinates. The curves on the right side of the figure show the average z-direction density distributions of the different types of atoms present in the system (scaled independently for clarity): $Na^+$ (blue), water oxygen (red), water hydrogen (gray) as well as all MMT atoms (black).

Our decision to investigate the influence of clay structure rigidity was motivated by the fact that most previous MD simulation studies of clay interlayer nanopores probed relatively small smectite-water systems (< $10^4$ atoms) using rigid smectite clay structures. The use of fully flexible clay layers has been advocated by several authors (Kalinichev et al., 2000; Cygan et al., 2004), but data comparing systems with rigid and flexible clay structures have not been published. To fully evaluate the influence of clay flexibility, we modeled systems where the clay lamellae were either fully rigid, fully flexible, or semi-flexible (i.e., all atoms were fixed except the structural H atoms). To probe the influence of simulation cell size, we simulated clay-water systems with one, two, three, or four clay lamellae (denoted MMTx1-4), as shown in Figure 4.2, and homogeneous systems (bulk water with dissolved $Na^+$) with 512, 2778, or 22,224 water molecules. Simulation cell size is known to influence diffusion coefficients predicted by MD simulations, but this artifact has only been studied in simulations of bulk fluids (Yeh and Hummer, 2004), never in simulations of porous media. Finally, we simulated systems with a range of water contents (12, 15, and 18 $H_2O$ molecules per unit cell) because although the basal spacing of the three-layer hydrate [1.89 nm (Kozaki et al., 1998; Chen et al., 2009)] is relatively well known from XRD data, the exact water content of the three-layer hydrate is less precisely known.

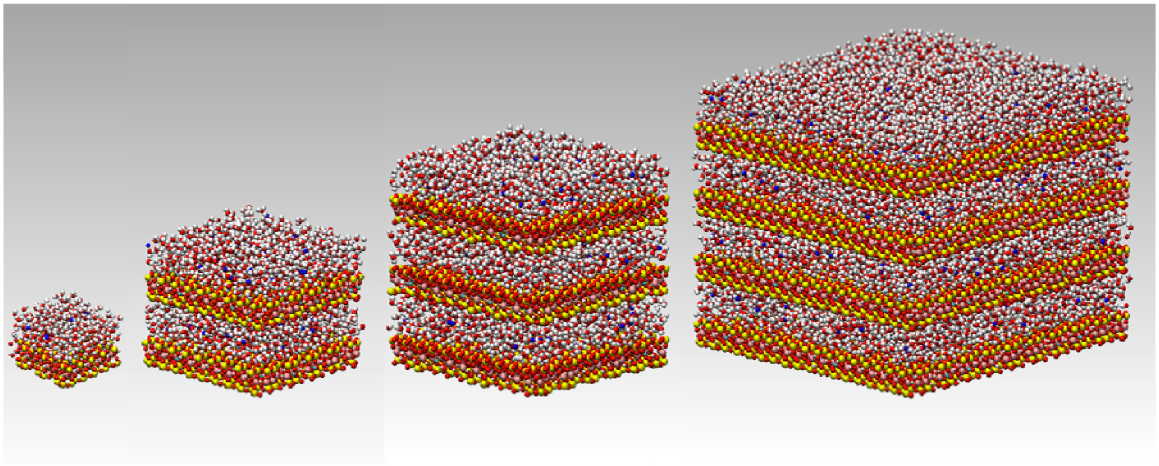

Figure 4.2. MD simulation snapshots showing the four different sizes of MMT/$H_2O$/$Na^+$ systems simulated in this work, hereafter designated as MMTx1-4 (from left to right).

## 4.1 Simulation methodology

In brief, our methodology uses the versatile MD code LAMMPS (Plimpton, 1995) with a rigid SPC/E water model and the CLAYFF force field (Cygan et al., 2004), which is known to correctly predict a range of structural and thermodynamical properties of smectite interlayer water and exchangeable cations (Bourg and Sposito, 2010; Ferrage et al., 2011) The CLAYFF force field includes atomic partial charges and van der Waals parameters for all clay structural atoms along with bond stretch parameters for structural OH groups. The clay investigated in this study was a typical 2:1 $Na^+$-exchanged smectite (Wyoming montmorillonite) with the unit cell structural formula of $(Al_{3.33}Mg_{0.66})Si_8O_{20}(OH)_4Na_{0.66}$, i.e., containing a negative structural charge of 0.66/unit cell, created by Al to Mg substitutions in the octahedral sheet. Clay atomic coordinates were taken from Bickmore et al. (2003) and relaxed during an initial equilibration in the NVT ensemble (constant number of particles, volume and temperature) followed by a volume optimization in the NPT ensemble (constant number of particles, pressure and temperature), resulting in equilibration runs of > 500 ps in fully flexible configurations at the corresponding sizes and temperatures. Production runs were then carried out for a total duration of 10 ns for each simulated system. In total, close to 300,000 CPU hours were used on the Hopper NERSC cluster, a Cray XE6 with 153,216 compute cores. For each simulated system, we determined the self-diffusion coefficient of water and sodium (hereafter we focus primarily on the sodium results) from the slope of the mean square displacement of the simulated particles using the well-known Einstein relation,

$$D = \frac{1}{2n} \lim_{\tau \to \infty} \frac{d\langle l^2 \rangle}{d\tau} \tag{4.1}$$

where $n$ is the dimensionality of the system and $\langle l^2 \rangle = \langle |r(t) - r(t+\tau)|^2 \rangle$ is the mean square displacement.

## 4.2 Results

***Interlayer water content:*** Our simulations with different water contents showed that an interlayer water content of 14.5 ± 0.5 water molecules per unit cell is consistent with experimental data on the basal spacing of the three-layer hydrate of Na-MMT. Within this range, uncertainty regarding the interlayer water content has a negligible influence on the overall uncertainty of predicted $E_A$ values. Therefore, we focus hereafter on results obtained at the interlayer water content of 15 water molecules per unit cell.

***Flexibility of the clay structure**:* Figure 4.3 shows the $D$ values of $Na^+$ in the three-layer hydrate of Na-MMT for different degrees of flexibility of the MMT structure. Similar data were obtained for $H_2O$. In general, although clay flexibility had a small influence on the self-diffusion coefficients of $Na^+$ and $H_2O$, the influence on $E_A$ was substantial, with a difference of 2.5 kJ/mol when comparing the fully flexible and fully rigid systems. The semi-flexible system yielded essentially the same $E_A$ values as the fully flexible system, suggesting that most of the impact of clay flexibility on the dynamics of interlayer water and sodium results from the motion of H atoms in the clay structure. This finding is quite remarkable in view of the fact that the clay H atoms are not in direct contact with the interlayer water (Figure 4.1).

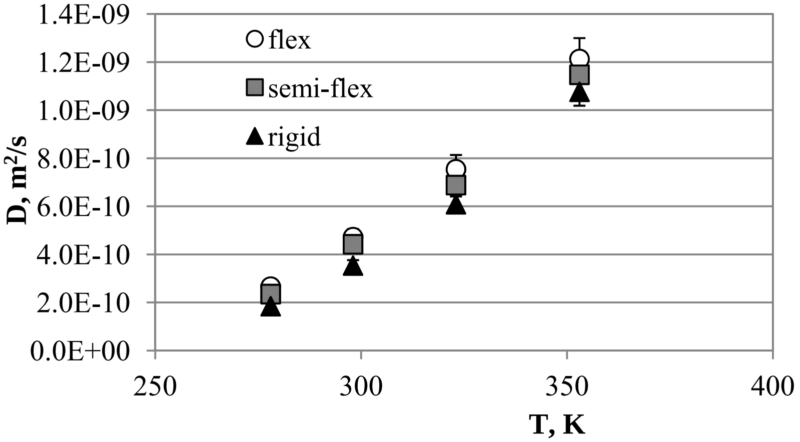

Figure 4.3. MD simulation predictions of the self-diffusion coefficient of $Na^+$ as a function of temperature for different degrees of flexibility of the MMT structure from fully flexible or semi-flexible (with flexible structural hydroxyl groups) to fully rigid.

***Simulation cell size:*** Our results on the size-dependence of $D$ are shown in Figures 4.4 and 4.5 for the systems with a fully flexible clay structure and a water content of 15 water molecules per unit cell. In general, we find that $D$ decreases linearly with the inverse of the simulation cell size ($1/L$) as expected from simulations of bulk liquid water (Yeh and Hummer, 2004). Interestingly, for $Na^+$ (but not for $H_2O$) the smallest system deviates from the expected trend, perhaps because the arrangement of structural charge sites in a system with a single clay sheet creates unrealistic charge and electric field environments.

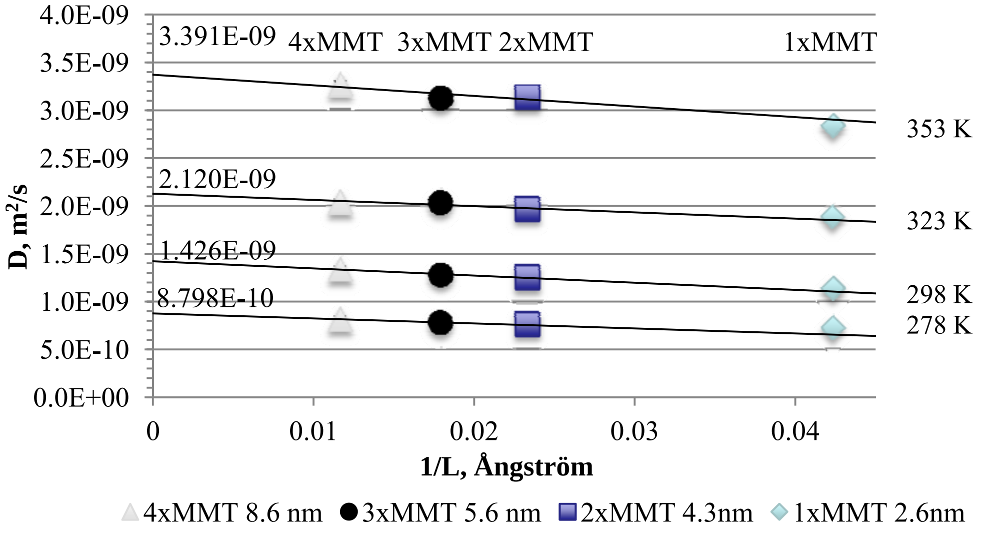

Figure 4.4. Self-diffusion coefficients of $H_2O$ plotted vs. the inverse of system size.

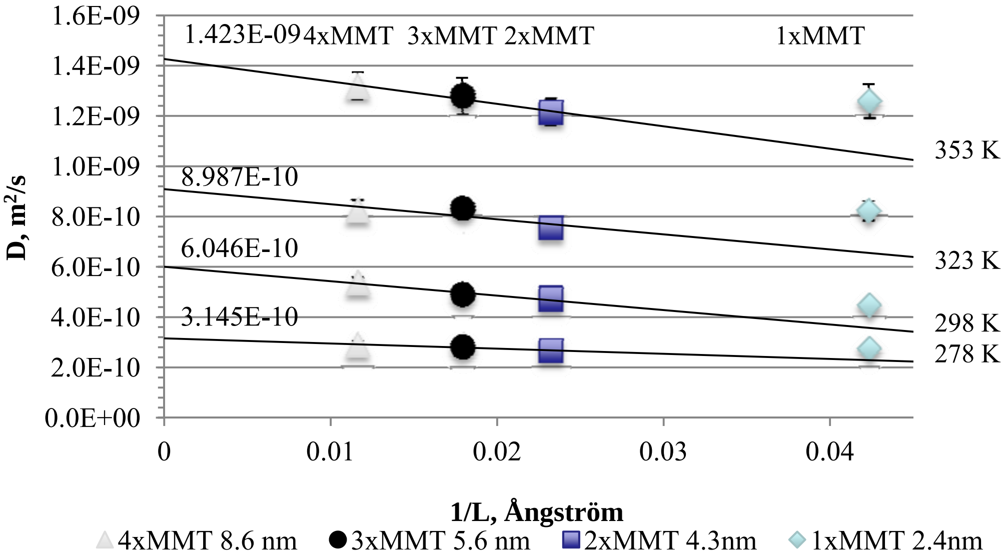

Figure 4.5. Self-diffusion coefficients of $Na^+$ plotted vs. the inverse of system size.

***Prediction of $E_A$ values:*** Figure 4.6 summarizes the $E_A$ values obtained for $Na^+$ (data for water are not shown) in bulk liquid water and in clay interlayer water. The green column on the left side of the figure shows the measured $E_A$ value for sodium diffusion in bulk liquid water (18.43 kJ/mol). The second set of columns (denoted "*D* SPC/E") shows $E_A$ values calculated from sodium diffusion coefficient in bulk liquid water and in the three-layer hydrate of Na-MMT (reported for the fully flexible clay system). The third set of columns (denoted "*Ds* SPC/E") shows $E_A$ values calculated from MD simulation *D* values *extrapolated to an infinitely large simulation cell*. This third set of colums (our best estimates of the $E_A$ values of sodium) shows that our MD simulations closely approximate the experimental $E_A$ value for sodium diffusion in bulk liquid water (green bar). This third set of columns also shows that sodium diffusion in the three-layer hydrate of Na-MMT has a $E_A$ value roughly 2 kJ/mol lower than sodium diffusion in bulk liquid water. Longer simulations will be required to precisely quantify this difference.

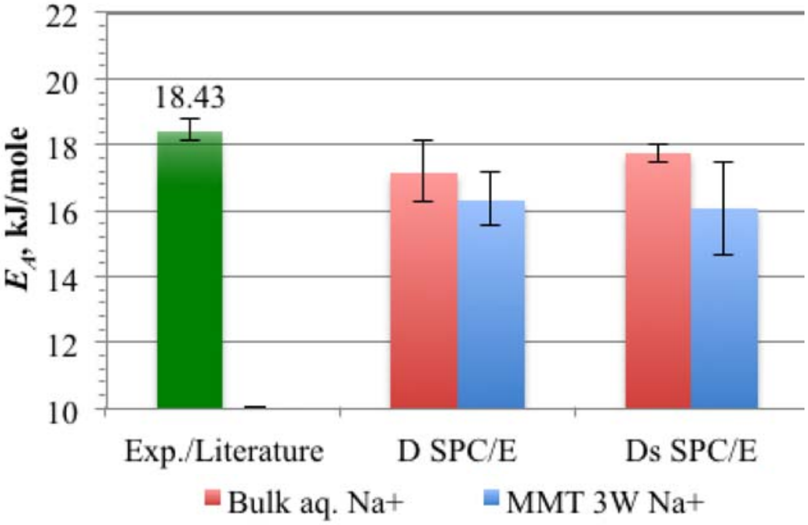

Figure 4.6. Comparison of our predicted $E_A$ values for $Na^+$ diffusion in bulk liquid water (red bars) and in 3-layer hydrate of Na-MMT (blue bars). The experimental value for $Na^+$ in bulk liquid water is displayed on the left (green bar).

## 4.3 Conclusions

Per molecular dynamics simulations, we determined the influence of temperature, clay structure flexibility, simulation cell size, and water content on water and sodium diffusion in the three-layer hydrate of Na-montmorillonite. Our simulations led to the development of a robust MD simulation methodology that correctly predicts the temperature dependence of sodium diffusion in bulk liquid water. This methodology predicts that sodium diffusion has a lower activation energy ($E_A$) in the three-layer hydrate of Na-montmorillonite than in bulk liquid water. These results open up a promising avenue for explaining experimental results on the activation energy of diffusion of ionic solutes in macroscopic samples of compacted montmorillonite. It will be possible to use these results to determine activation energies for diffusion through the compacted bentonite in larger (repository) scale models as a function of the evolving temperature field. In the nearer term, these activation energies will be used as input for microscopic continuum models of the kind described in Section 3.

# 5. EXPERIMENTAL STUDIES OF THE REACTIVE DIFFUSIVE TRANSPORT OF U(VI) IN BENTONITE

Bentonite backfill/buffer is proposed as part of EBS around nuclear wastes disposed in deep underground disposal sites. An important aspect of the prediction of repository performance for an EBS is the capacity of the barrier to limit the flux of radionuclides to the biosphere to acceptably low levels. Montmorillonite is the dominant mineral phase present in bentonites. In current models for radionuclide diffusion through bentonite in an EBS, the apparent and effective diffusion coefficients are linked through a $K_d$ value, a sorption partitioning coefficient that is often believed to be a constant value for a particular radionuclide and solid phase sample. In the case of U(VI), however, this s unlikely to be true because of the very high sensitivity of the $K_d$ value to pH and bicarbonate and calcium concentrations. By extension to the aqueous chemistry of other actinides, we can expect the $K_d$ values of Np(V), Am, and Pu(VI) to be also sensitive to pH and bicarbonate concentrations. It should be noted that waste forms, and possibly concrete in the vicinity of an EBS, are likely to create gradients in these chemical variables (pH, $HCO_3^-$, $Ca^{2+}$) within the EBS. Therefore, it is important to represent U(VI) (and other actinides) partitioning within an EBS with a *surface complexation model* rather than a constant $K_d$ value. This will have a significant impact on the conceptual model that describes U(VI) diffusion through an EBS.

## 5.1 Background

### 5.1.1 Diffusion of Radionuclides

The state of knowledge with respect to diffusion-driven flux shows that there are large differences in the measured diffusion behavior of various radionuclides, e.g. between halides ($^{36}$Cl, $^{129}$I) and actinides ($^{238,235}$U, $^{237}$Np, $^{232}$Th). The differing behaviors are a result of the two major processes that have important effects on macroscopic diffusive transport, i.e. *molecular diffusion* and *sorption.* The research effort described in this section is an effort to describe these two processes for U(VI) in fundamental terms and to develop a conceptual model that can be used in numerical, diffusion-driven transport models (Sections 3 and 4 of this report).

Generally speaking, the mineralogical composition of bentonites is nearly all montmorillonite. Varying amounts of carbonate minerals (calcite, dolomite), quartz, accessory minerals (pyrite, feldspar), other clay minerals, and organic matter are typically present at low concentrations. For an experimental study of fundamental processes, these other minerals present serious difficulties in the maintenance of aqueous chemical conditions and in constraining U(VI) processes to only diffusion and sorption. For example, the presence of calcite makes it extremely difficult to control pH and dissolved calcium and bicarbonate concentrations by experimental design, and each of these variables has a significant impact on U(VI) sorption (Davis et al., 2004; Fox et al., 2006). Furthermore, the presence of pyrite may cause reduction of U(VI) to U(IV). U(IV) would be present almost completely in the solid phase, either precipitated as $UO_2$ or very strongly sorbed, to a different extent than U(VI), thus complicating the quantification of U(VI) sorption. Because of the experimental difficulties introduced by such impurities and the objective of understanding the *fundamental processes* that control macroscopic diffusion, the experimental program in this research effort is composed of two parts, studies of U(VI) sorption and diffusion in: 1) pure montmorillonite, and 2) bentonite. The pure montmorillonite studied in this research is a purified sample of Wyoming Swy-2, Na-montmorillonite, as obtained from the Clay Minerals Society. The bentonite sample has not yet been selected, but will be chosen in consultation with other DOE laboratories.

Montmorillonite is composed of particles made up of positive charge-deficient alumino-silicate lamellae stacked one above the other (Figure 4.1). The net negative structural charge is compensated by cations located in the interlamellar space and adjacent to the external stack surfaces. These characteristics explain the substantial cation exchange capacities (CEC) and high specific surface areas of montmorillonite.

Two factors are known to be particularly important in controlling macroscopic diffusion: 1) the charge of the diffusing species (anion, cation, neutral), and 2) the degree to which the diffusing species adsorbs onto the mineral surface contacting the aqueous solution, commonly quantified in terms of the parameter, $K_d$, the sorption distribution coefficient (Bourg et al, 2003; 2006). Generally speaking, the interaction of these factors leads to the classification of radionuclides into two groups: one for elements relatively unaffected by sorption ($K_d \sim 0$), and for which the predominant species is generally anionic, and a second group for which sorption is important ($K_d > 100$).

Macroscopic diffusion has been classically evaluated based on Fick's laws for one dimensional diffusion in a saturated, homogeneous porous material, adapted to take into account "simple" effects of sorption on radionuclide flux through the material. These laws are as follows:

- *Fick's first law* (for steady state flux in one dimension) is given by $J = -D_e \frac{dC}{dx}$ where J is the solute flux ($mol \cdot s^{-1} \cdot m^{-2}$), $D_e$ the so-called 'effective' diffusion coefficient, and dC/dx the gradient in radionuclide concentration (C, $mol \cdot m^{-3}$) resulting from conditions imposed at the boundaries of the system (separated by a distance, dx (m)). The expression is then adapted to account for the effects of material porosity and pore space geometry by defining $D_e = D_0 \left(\frac{\delta}{\tau^2}\right) \omega$, where $D_0$ is the solute diffusion coefficient in free solution, ω is the total porosity, δ is a 'constrictivity' factor, and τ is a 'tortuosity' factor (≥ 1), representing the average length of the diffusion paths effectively linking the boundaries of the system relative to the distance dx.

- *Fick's second law* (for flux time dependence) is given by $\frac{\partial C}{\partial t} = D_a \frac{\partial^2 C}{\partial x^2}$ , where $D_a$ is the 'apparent' diffusion coefficient, given by $D_a = \frac{D_e}{(\omega + \rho K_d)}$, where ρ is the clay density ($kg \cdot m^{-3}$), and $K_d$ ($m^3 \cdot kg$) is a constant representing the partitioning of the radionuclide between total mobile dissolved species and total immobilized sorbed species. Note here that the word, total, refers to the fact that the dissolved and sorbed radionuclide may have several species in aqueous solution and sorbed to the clay. $K_d$ is generally determined experimentally. If needed, $K_d$ can be replaced in numerical macrodiffusion models by more complex representations (isotherms, surface complexation models) capable of taking into consideration variable sorption as a function of system composition. It is the intent of this research to determine a surface complexation model and conceptual model for U(VI) sorption on montmorillonite that would replace $K_d$ in the expressions above.

Values for diffusion and sorption parameters have been measured for a variety of radiotracers in montmorillonites and bentonites (van Loon et al., 2007; Glaus et al., 2007; Bradbury and Baeyens, 2000, 2002, 2005). The vast majority of the experimental data measured the flux through a mass of clay material compacted to a given density and equilibrated with an electrolyte solution of known composition. Most data have been collected for non-sorbing anions (e.g. $^{36}Cl^-$,

$^{129}I^-$), tritium, i.e., the water tracer (HTO), and alkali ($Cs^+$, $Na^+$, $K^+$, $Rb^+$, $Li^+$) and alkaline earth ($Sr^{2+}$, $Ca^{2+}$) cations. Several interesting trends have been observed:

1) $D_e$ and associated 'accessible porosity' values for anionic tracers are generally much smaller than corresponding values for HTO,

2) $D_e$ for anions has been observed to *decrease* with decreasing solution ionic strength (van Loon et al., 2007)

3) $D_e$ values for certain cations ($Na^+$, $K^+$, $Rb^+$, $Cs^+$) have been found to be significantly higher than $D_e$ for tritium (HTO) and *increases* with decreasing solution ionic strength.

4) $D_e$ for any given tracer type (anion, HTO, cation) tends to decrease with increasing material density.

The current conceptual model for radionuclide (and U(VI)) diffusive transport in clay and bentonites has the following features:

- U(VI) dissolved speciation is determined by the bentonite porewater composition. Thus, understanding the macroscopic diffusive transport of U(VI) requires a thorough characterization of the composition of aqueous solutions, as this determines the solubility and speciation of U(VI). U(VI) is known to form strong ternary aqueous complexes with $CO_3^{2-}$ and $Ca^{2+}$ (Fox et al., 2006).

- The majority of connected porosity is associated with the clay mineral fraction of a bentonite, a major proportion of which is made up of the permanent negative charge clay mineral, montomorillonite.
- U(VI) solid-solution partitioning in bentonites is dominated by sorption on montmorillonite minerals, although there could be exceptions for unusual bentonite samples, in which other minerals contribute to U(VI) sorption, or for systems in which U(VI) is reduced to U(IV).
- U(VI) sorption on bentonites and montmorillonites can be described using surface complexation models that divide U(VI) sorption between ion exchange sites and complexation by edge sites.
- Accessible porosities differ depending on radionuclide species net charge, with cations and neutral species accessing most if not all of the total connected porosity, while anions are excluded from clay interlayer volumes and the solution immediately adjacent to external basal surfaces – anion accessible porosity is therefore less than the total porosity.

### 5.1.2 Surface complexation models for U(VI) sorption on montmorillonite

Several models have been developed to describe surface complexation on montmorillonite. However, there is a lack of consistency among these models and large differences in the conceptual development. For example, some of the models have been developed with an electrical double layer model (generally the diffuse double layer model) to provide an electrostatic energy correction term to the mass laws for surface complexation. Others have been developed without electrostatic potential correction terms. Most differentiate between binding within the interlamellar space (called ion exchange, and believed to be dominated by electrostatic energy) and binding at the edge sites of the alumino-silicate layers, where the layer structures are terminated (surface complexation, dominated by covalent chemical bonds). Some differentiate between aluminol and silanol groups that are present at the edge sites.

A classic paper in the field is that of McKinley et al. (1995), who studied U(VI) sorption to montmorillonite in $NaClO_4$ solutions as a function of ionic strength and pH under a $N_2$(g) atmosphere. The authors developed a surface complexation model that described their experimental U(VI) sorption data. The model included fixed-charge (ion exchange sites) and aluminol and silanol edge sites similar to those on gibbsite and quartz. At low pH and low ionic strength, U(VI) was bound predominantly to the ion exchange sites; the concentration of ion exchange sites was determined experimentally. The concentration of edge sites was estimated by image analysis from a transmission electron microscope (TEM). The binding constants for surface complexation of U(VI) at aluminol and silanol sites, and for $UO_2^{2+}/2Na^+$ ion exchange, was determined by fitting to the experimental U(VI) sorption data. The triple layer electrical double layer (EDL) model was used to correct for electrostatic energy terms associated with U(VI) binding to the edge sites. The EDL properties of the aluminol sites were based on fitting acid-base titration data for gibbsite and for the silanol sites using data from the literature. A half-reaction approach was used for the ion exchange reactions.

Important new data that impact conceptual model development were collected in the paper of Catalano and Brown (2005). Extended X-ray absorption fine structure (EXAFS) spectroscopy was performed for samples with sorbed U(VI) at various pH values and ionic strengths. Solutions reacted with the montmorillonite samples were in equilibrium with partial pressure of $CO_2$(g) in air. The spectroscopic results at low pH (about 4) and low ionic strength (0.001M) agree with the conclusion of McKinley et al. (1995) that U(VI) sorption was dominated by ion exchange. At pH 7 and at high ionic strength (1M), spectroscopic results indicate covalent surface complexation binding of U(VI) species. For conditions between these two extremes, both ion exchange and surface complexation binding of U(VI) was indicated, and the general results suggested that ion exchange was likely more important under these conditions than was previously thought by McKinley et al. (1995). Furthermore, the authors concluded that the covalent surface complexation binding on montmorillonite occurred at iron (Fe) octahedral edge sites rather than at aluminol and silanol sites as had been previously thought. The Fe atoms to which U(VI) was bonded (through oxygen atoms) was not thought to be present as contaminant iron nanoparticles, but instead to uncommon Fe atoms that had substituted for Al atoms in the octahedral sheets that make up the montmorillonite mineral structure. The spectroscopic results also led to a conclusion that a significant fraction of the U(VI) bound at edge sites was also bound with one or two carbonate molecules, a so-called ternary surface complex (Bargar et al., 2000). No sorbed U(VI) dimers or polymers were observed, suggesting that the U(VI) multimeric surface species assumed to exist at the montmorillonite by McKinley et al. (1995) did not occur. This study has important implications for the development of a surface complexation model for U(VI) sorption on montmorillonite, especially the evidence for the speciation of sorbed U(VI).

Bourg et al. (2007) reviewed the surface chemistry of montmorillonite and an important new interpretation of acid-base titration data for montmorillonite/solution suspensions and the estimation of surface potentials at edge sites, with special influences from the work of Tournassat et al (2004) and Bickmore et al. (2003). Along with the paper by Catalano and Brown (2005), this work should have a major impact on the development of new surface complexation models for U(VI) sorption on montmorillonite. Tournassat et al. (2004) developed an edge surface structure and reactivity model that explicitly includes edge sites that arise from the isomorphic substitution of Fe(III) for Al, based on the chemical composition of the bentonite sample, MX-80. The total number of Fe-substituted sites in MX-80 is equal to 0.68 sites/$nm^2$, divided among three site types, Fe(III)-hydroxyls, Fe-Si bridging hydroxyls, and Fe-Al bridging hydroxyls. Ten types of edge site hydroxyls were identified, each with its own acidity constant, and it was argued that the electrical potential related to the constant charge deficiency of the mineral structure has an influence on edge site electrical potential. These interactions result in a complex electrical double layer model for the edge sites.

In conclusion, a conceptual model for the binding of U(VI) to montmorillonite exists but a surface complexation model has not been carefully calibrated over a wide range of chemical conditions. In addition, the complexities of the electrical double layer at edge sites have not yet been incorporated in any surface complexation model. Moreover, new thermodynamic data are available for the U(VI) system that indicate that uranyl-calcium-carbonate ternary aqueous complexes dominate U(VI) speciation and affect its sorption behavior (Fox et al., 2006; Bradbury and Baeyens, 2011). A systematic study of sorption as a function of U(VI) aqueous speciation for variable pH, bicarbonate, and Ca concentrations is needed. Surface species need to be selected for a new surface complexation model that are consistent with bond valence calculations and spectroscopic results (Arai et al., 2006; Catalano and Brown, 2005) and the acid-base chemistry model of Bourg et al. (2007).

## 5.2 Materials and Methods

Our research goal is to gain a detailed understanding of U(VI) sorption characteristics onto clay minerals as a function of U(VI) solution speciation. A mechanistic understanding of U(VI) sorption behavior is required for the interpretation of apparent diffusion coefficients, and the de-coupling of U(VI)-mineral interactions from apparent metal diffusion rates. U(VI) sorption data are needed for the successful design of U(VI) diffusion experiments, e.g. in terms of expected U(VI) concentrations in the solid phase, the duration of experiments, and appropriate sampling intervals. Our research approach includes a variety of experiments as well as the development of U(VI) surface complexation models.

First, typical batch sorption envelope experiments were performed to characterize U(VI) sorption onto a pretreated clay mineral (Na-montmorillonite) over a range of pH conditions and atmospheric $CO_2$ concentrations, using specific sorption equilibration times. The partial pressure of carbon dioxide in equilibrium with the solution phase was varied in order to study the role of U(VI)-carbonate solution complexes on U(VI) sorption. The experiments described in this report had the goal to minimize calcium solution concentrations, and hence, the influence of ternary aqueous U(VI)-Ca-carbonato complexes. However, future experiments will also include calcium at various, controlled solution concentrations. The resulting batch sorption data are used in the development of U(VI)-Na-montmorillonite surface complexation models (SCMs), which are able to link U(VI) sorption behavior with U(VI) solution speciation based on existing thermodynamic data.

Second, batch kinetic studies were performed to investigate U(VI) sorption kinetics at various ionic strength conditions, which is motivated by the following reasons. First, kinetic data are needed for the selection of appropriate sorption equilibration times in lab-scale experiments, which aim to characterize U(VI) sorption under equilibrium conditions. For instance, substantial errors may be introduced into model-based predictions of U(VI) mobility if experimentally-determined $K_d$ values do not represent equilibrium values. Second, U(VI) contact times with the solid phase are expected to be substantially longer in diffusion experiments than in typical batch sorption studies. Therefore, kinetic data over extended sorption times are needed in order to ensure that metal sorption characteristics are comparable between these systems. Finally, it is well understood that differences in the series of elemental reactions comprising a reaction pathway can lead to changes in the overall reaction rate (Stone and Morgan, 1990). Hence, kinetic sorption studies provide a useful tool to indicate potential changes in the dominant, underlying processes responsible for U(VI) sorption, e.g. as a function of chemical solution composition. For instance, Nagasaki reported fast (‘outer’ surface) and slow (‘interlayer’ surface) steps for U(VI) sorption to montmorillonite in the absence of organic ligands (Nagasaki, 2001), while in the presence of U(VI)-humic acid complexes only the fast metal sorption step was observed. Kinetic results do not allow any conclusions about the formation of specific surface complexes, in contrast to spectroscopic data. However, they provide first indications of potential changes in sorption mechanisms over a range of environmentally relevant U(VI) concentrations, which are typically far below the concentration limits accessible by spectroscopic techniques.

### 5.2.1 Materials

All chemicals used in this study were reagent grade or better. Acids, bases and salt solutions used in equilibrium and kinetic batch experiments were of TraceSelect grade (Sigma Aldrich) in order to minimize calcium background concentrations. Aqueous solutions were prepared with Nanopure water (Barnstead ultrapure water system). Glassware was cleaned by soaking in acid (10 % (v/v) HCl) over 12 to 24 hours, followed by thorough rinsing with Nanopure water and air-drying.

U(VI) solutions contained $^{238}$U from a 1.299 mM uranyl nitrate stock solution, provided by Dr. David Singer and originally obtained from Wayne Lukens (both, Lawrence Berkeley National Laboratory). Uranium solution concentrations were quantified by ICP-MS after acidification with TraceSelect grade $HNO_3$. All samples from batch sorption studies were analyzed for U solution concentrations; selected samples were analyzed for calcium background concentrations and for elements that could indicate clay dissolution or insufficient solid-liquid separations (Si, Al, Fe, etc.).

A commercially available, well-characterized, standardized Source Clay (Na-montmorillonite, SWy-2, Clay Minerals Society) was selected for experimental study. This material is known to contain considerable impurities of quartz (8 %) and feldspars (16 %) as well as calcite (Costanzo and Guggenheim, 2001; Chipera and Bish, 2001; Mermut and Cano, 2001). This required a purification procedure in order to ensure that U(VI) sorption is investigated for a (reasonably) pure clay mineral. Hence, prior to its use in experiments, the clay was pretreated to remove mineral impurities and minimize calcium release from the mineral due to Ca-carbonate dissolution during experiments (see 5.2.2 Clay Pretreatment). Treatment methods were selected with the goal to effectively remove mineral impurities while preserving the original clay characteristics as much as possible. After mineral pretreatment, a clay stock suspension of 10 g/L was prepared in Nanopure water, and its exact solid concentration determined by weighing two 10 mL volume fractions before and after drying at 45 °C. A solid concentration of 0.5 g/L was selected for all batch sorption studies, in order to cover a range of U surface concentrations while avoiding complete (i.e. 100%) U(VI) sorption.

### 5.2.2 Clay Pretreatment

The steps for the pretreatment of Na-montmorillonite (SWy-2, Clay Minerals Society) included: (1) the removal of calcite impurities using a sodium acetate/acetic acid solution, (2) the clean-up of acetate from the clay suspension with Nanopure water, (3) transforming the clay into its sodium-form by equilibration with a Na-salt solution, (4) the removal of excess Na-salts from suspended clay, (5) the separation of quartz and feldspar impurities from clay particles by centrifugation and (6) oven-drying of the clay mineral phase. We decided to first treat a small batch (approximately 20 grams) of the Source Clay according to this procedure, to monitor relevant solutes over the course of this pretreatment process, and to use this clay material for a first set of batch sorption envelope and batch kinetic experiments. Then, the results from the monitoring of the purification process combined with data describing the release of calcium in batch experiments will allow us to decide if the selected pretreatment methods are sufficient for our experimental needs. Pretreatment steps were performed using dialysis membranes, since it is possible to efficiently 'up-scale' this set-up for the purification of larger mineral quantities later on.

At the beginning of the pretreatment, dialysis membranes (SpectraPor #6, 8kDa MWCO, regenerated cellulose, 40 mm flat width) were cleaned by soaking (15-30 minutes) and thorough rinsing in Nanopure water for three times. In the meantime, four liters of extractant solution of 1 M sodium-acetate/glacial acetic acid (0.5635 M), buffered at pH=5, were prepared. Aliquots of the extraction solution and all other solutions used as dialysis buffers subsequently were collected for ICP-MS (Ca, Mg, Mn, Ti, Si, Al, K, Fe) and IC (acetate, nitrate) analysis blanks, and the original conductivity of the solution was determined. Then, approximately 20 grams of the original Source Clay (as received) were weighed into a glass beaker, and 40 mL of extractant solution added. After stirring the suspension with a disposable transfer pipette for about one minute, the suspension was filled into two 13-cm long, pre-cleaned dialysis bags using a glass funnel.

Then, the clay contained in the dialysis bags was dialyzed against approximately 950 mL of the extractant solution in a glass beaker over 3.5 hours. Afterwards, the buffer solution was sampled for ICP-MS and IC analysis and the conductivity of the solution recorded. Dialysis bags were brought into contact with a fresh sodium acetate/glacial acetic acid buffer solution of the same volume, and the dialysis continued over another 43.6 hours. Again, at the end of this dialysis step, the buffer solution was sampled for ICP-MS and IC analysis of metals and salts, and its conductivity measured. This procedure was continued, for a total of four dialysis steps with acetate extractant solutions over various individual dialysis time-frames (3.5, 43.6, 5.7 and 15.2 hours). Then, the buffer solution composition was changed to a 1 M $NaNO_3$ solution in order to bring the clay into its Na-form, again following a similar buffer exchange and sampling procedure. Overall, four buffer exchanges with nitrate solutions were performed using individual dialysis times of 4.4, 4.5, 15.3 and 3.5 hours. Finally, excess salts were removed from the clay by dialysis against Nanopure water over a series of five buffer exchanges with dialysis times of 2.8, 16.7, 2.8, 6.8 and 13.2 hours.

In the next step, the clay was removed from the dialysis bags and re-suspended in Nanopure water. In order to fully re-suspend the solid, the suspensions were sonicated, stirred in glass beakers and shaken up by hand after transfer into 250 mL Corning glass bottles. Then, the clay suspension (2 x 600 mL) was poured into centrifugation liners and centrifuged on a Beckman Avanti J-25 centrifuge at 1000 g over 7 minutes. This centrifugation time was calculated (based on Stokes law) to effectively remove particles of an average particle size > 2 µm from suspension, which is believed to be an appropriate size cut-off for quartz and feldspar impurities. After centrifugation, the supernatant solutions were transferred into glass beakers and dried in a VWR convection oven set at 45 °C , which resulted in a temperature of 42-43 °C inside the oven. The larger size fraction produced in the centrifugation step, which was characterized by a darker sediment color, was discarded. Depending on the beaker size used during drying, the clay suspensions took 6-13 days to reach apparent dryness.

The dried clay was recovered from the glass beakers using Teflon rods. Then, the mineral was milled in 10 mL capsules using a Retsch MM 400 ball mill at a frequency of 30/sec over two minutes. After milling of several clay batches, all of the material was combined in one glass beaker and thoroughly homogenized. Last, a 10 g/L stock suspension was prepared and its exact solid concentration determined by drying as described above.

### 5.2.3 Batch Sorption Equilibrium Experiments

All batch sorption experiments were set up at room temperature (22.5 – 23.5 °C), with a nominal total U(VI) concentration of $10^{-6}$ M, a Na-montmorillonite concentration of 0.5 g/L, and a total ionic strength of 0.1 M. Target pH values ranged from 4.0 to 10.0; the sorption equilibration time was set at 48.5 hours. Solutions were equilibrated with three different gas phases varying in terms of their $CO_2$ partial pressures: (1) atmospheric $CO_2$ in air (0.039%, 390 ppm), (2) $CO_2$-free atmosphere (glove box, filled with 93.3% $N_2$/5.7% $H_2$ gas mixture) (3) ~1% $CO_2$ atmosphere (disposable Sigma Aldrich glove bag purged with certified 2% $CO_2$/balance nitrogen gas mixture; Praxair P/N: NI CD2C-K). In experiments performed under atmospheric or elevated $CO_2$ levels, additions of sodium bicarbonate buffer were used to facilitate solution equilibration with the gas phase for samples with target pH values of 7.0 or greater. Fifty-mL polycarbonate centrifuge vials ('Oakridge centrifuge tubes') were used as sample vials to minimize U(VI) wall sorption effects. In addition to samples containing Na-montmorillonite and U(VI) (1 replicate per pH condition), each experiment also included experimental standards (in duplicate). These standards represented 100% of the U(VI) solution concentration in the absence of a mineral phase and at pH conditions selected for minimization of wall sorption effects (pH=2). In addition, electrolyte blanks containing 0.1 M NaCl but no U(VI) or solid were used in order to provide blank values (in duplicate) for calcium concentrations.

At the beginning of batch sorption experiments, aliquots of Nanopure water, the Na-montmorillonite stock suspension and a 1M NaCl solution were transferred into sample vials to give the desired solid concentration and ionic strength in the final sample volume of 40 mL. For samples with target pH values of equal or above 7.0, increasing amounts of 1M or 0.1M $NaHCO_3$ buffer solution were added. Solution pH values were adjusted with small volumes of 1, 0.1, 0.01 and 0.001M HCl or NaOH solutions, and closed sample vials pre-equilibrated with shaking over 12 to 24 hours. On the next day, aliquots of the U(VI) stock solution were added to obtain the final desired concentrations. After re-adjustment of solution pH, U(VI) sorption equilibration was allowed to take place during shaking over 48.5 hours. Afterwards, final pH values were recorded while minimizing gas exchange during the pH measurements. Then, a 13-mL aliquot of the sample suspension was removed by pipetting in order to decrease the liquid mass of the suspensions, and decrease sample centrifugation times. The remaining 27 mL of the sample suspensions were centrifuged to remove >50 nm particles from solution, as calculated based on Stokes law (Beckman Coulter Allegra 64R, F0850 rotor, centrifugation at 26,900 g over 61 minutes). Afterwards, 1.5 mL and 20 mL aliquots of supernatant solution were collected to analyze for metal concentrations by ICP-MS, and carbonate concentrations by Total Inorganic Carbon (TIC) analysis on a Shimadzu TOC-V.

For the correction of U(VI) wall sorption effects, solid phases and remaining sample solutions were discarded, and vials briefly rinsed with UV-water. In the process, some clay was re-mobilized from the container vials by vigorous shaking by hand, or if necessary, by using disposable, plastic transfer pipettes. Sample vials were then filled with 40 mL of 2% nitric acid solutions (TraceSelect grade) in order to facilitate U(VI) desorption from container walls during shaking over approximately 60 hr. Washing solutions were analyzed for concentrations of desorbed U(VI) as described above.

Experimental results for batch sorption envelope experiments are reported in terms of distribution coefficients ($K_d$ values) and fractions of U(VI) sorbed. Distribution coefficients, with units of L/kg, represent the ratio of sorbed (e.g., in mol/kg) over dissolved (e.g., in mol/L) U concentrations after sorption reaction for 48.5 hours. Sorbed U(VI) fractions were calculated based on concentration differences in supernatant and acid-wash solutions:

$$f_{U(VI)_{sorbed}} = \frac{\left([U]_{Std,supernat.} + [U]_{Std,wash}\right) - \left([U]_{Sample,supernat.} + [U]_{Sample,wash}\right)}{\left([U]_{Std,supernat.} + [U]_{Std,wash}\right)} \times 100\% \qquad (5\text{-}1)$$

where $[U]_{supernat.}$ and $[U]_{wash}$ represent U(VI) concentrations in supernatant and acid-wash solutions for standards (subscript *Std*) and individual sample vials (subscript *Sample*) respectively.

### 5.2.4 Batch Kinetic Experiments

In order to allow for a direct comparison, kinetic studies were also set up at room temperature (22.5 – 23.5 °C), with a nominal total U(VI) concentration of $10^{-6}$ M and a Na-montmorillonite concentration of 0.5 g/L. All kinetic samples were in contact with atmospheric $CO_2$ in air (0.039%, 390 ppm). Total ionic strengths were varied between the values of 0.002, 0.01, and 0.1M; pH conditions were set up at target values of pH=5.

In kinetic experiments, U(VI) sorption behavior was characterized as a function of time based on the repeated sampling of the same sample suspension at specified time-points. Hence, larger, initial sample volumes (100 mL) were needed. Furthermore, standard concentrations representing 100% of U(VI) in solution in the absence of a mineral phase were calculated based on direct ICP-MS analysis of 5 µL aliquots of the U(VI) stock solution. No wall sorption corrections were performed in these experiments. However, due to the use of larger suspension volumes and sample vials compared to the batch equilibration experiments, we assume that the total mineral surface area may largely exceed the total surface area of container walls. This would lead to even lower wall sorption effects than observed in batch equilibration experiments.

Kinetic sorption experiments consisted of two main steps: (1) pre-equilibration of U(VI) solutions and Na-montmorillonite suspensions at the specified pH and ionic strength conditions; and (2) time-dependent sorption of U(VI) onto the clay, which is characterized by repeated sampling of sample suspensions. On the first day, we prepared 43.8 mL U(VI)-electrolyte solutions and clay-electrolyte suspensions in 125 mL Nalgene bottles and 50 mL Corning centrifuge tubes, respectively. In the process, we combined Nanopure water with 1M NaCl, and an aliquot of either the U(VI) stock solution or Na-montmorillonite stock suspension. Addition volumes were selected in order to give the desired final concentrations in a total suspension volume of 100 mL. The pH values of solutions were adjusted with small volumes of HCl and NaOH (1, 0.1, 0.01, 0.001M; $V_{pH,1}$ = 3.75 mL). Then, sample vials were set up on a shaking table for pre-equilibration overnight.

On the next day, a second pH check/adjustment was performed ($V_{pH,2}$ = 2.5 mL). Then, the kinetic experiment and recording of time was started by pouring the individual clay suspensions into the Nalgene bottles containing U(VI) solutions at the same pH and ionic strength. After brief mixing of suspensions by hand, four 1-mL volume fractions were transferred into four 2-mL centrifugation vials. (Suspension volumes of 1 mL in 2-mL centrifugation vials were selected in order to minimize the height of liquid levels, sample centrifugation times, and hence, the time-frames needed in between sampling events.) The remaining sample suspensions were set up for sorption equilibration under continuous shaking. Sampled suspensions were centrifuged in order to remove >50 nm clay particles, based on calculations using Stokes law (Beckman Coulter Allegra 64R, F3602 rotor, 11 minutes at 26,000 g / 16,335 rpm). After centrifugation, two 0.75 mL supernatant fractions were combined twice to give two 1.5-mL sample solutions for ICP-MS analysis.

After sampling the first time-point, basically the same sampling/centrifugation procedure was followed for the rest of the kinetic experiment. However, for the remaining time-points only one 1.5 mL ICP-MS sample was created per sampling event. In addition, the same procedure was applied to collect supernatant solutions for TIC analysis on the first and last day of the kinetic experiment. TIC measurements allow us to determine if potential changes in dissolved carbonate concentrations occurred over time. Last, the pH-values of sample suspensions were determined every couple of days in order to monitor for any potential pH-shifts over the course of the experiment.

## 5.3 Results and Discussion

### 5.3.1 Clay Pretreatment

An overview of the conductivity measurements over the course of dialysis steps using different types of buffer solutions is given in Figure 5.1. In the following figures, all of the measurements represent values determined in buffer solutions at the end of individual dialysis steps; the switching to different, initial buffer solution compositions, from Na-acetate/acetic acid to sodium nitrate and Nanopure water, are indicated by dashed lines in the diagrams. First, conductivity measurements (Figure 5.1) show fairly constant values for the dialysis steps with extractant and 1 M $NaNO_3$ solutions. This is followed by a sharp drop with the use of Nanopure water as dialysis buffer, and is continued with increasingly lower conductivity values due to the repeated exchange of Nanopure water (lowest conductivity value measured: 151 μS/cm). For comparison, the fractions of Na, acetate and nitrate remaining in the buffer solutions over time (Figure 5.2) show similar trends. Hence, conductivity measurements are a useful tool to monitor clay dialysis in ‘real-time’. In addition, the dialysis procedure appears to effectively remove excess salts from the pretreated clay.

Furthermore, Ca solution concentrations in the extractant buffer solutions during Ca removal steps are shown in Figure 5.3. These measured concentrations were further used in a mass balance calculation in order to estimate (1) the efficiency of the Ca removal process, and (2) the maximum Ca concentrations potentially released from pretreated Na-montmorillonite in later batch sorption experiments. In this calculation, we used the CaO content provided for SWy-2 by the Clay Minerals Society (1.68% (w/w)), and assumed a solid concentration of 0.5 g/L in batch experiments. We determined that the Ca purification steps removed 84.8% of total Ca found in the original Source Clay material. Furthermore, maximum Ca solution concentrations in batch sorption experiments were estimated at 2.3 x $10^{-5}$ mol/L. Actual measurements of calcium concentrations released over the course of batch sorption envelope experiments are provided in the Results and Discussion section for batch sorption equilibrium experiments. Overall, Ca concentrations measured in batch experiments agree well with the upper limit estimated based on mass balance considerations. Furthermore, our data indicate that Ca concentrations released from the clay in batch sorption experiments are not high enough to affect U(VI) solution speciation in terms of the formation of ternary U(VI)-Ca-carbonato species in these systems.

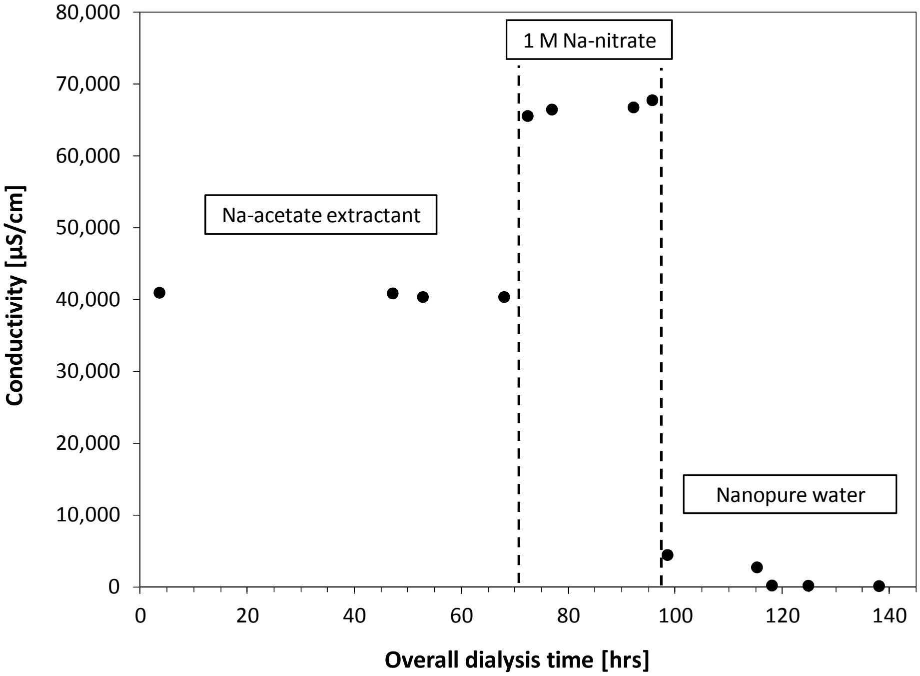

Figure 5.1. Results of conductivity measurements of dialysis buffer solutions over the course of clay pretreatment steps. (Dashed lines indicate changes in buffer compositions.)

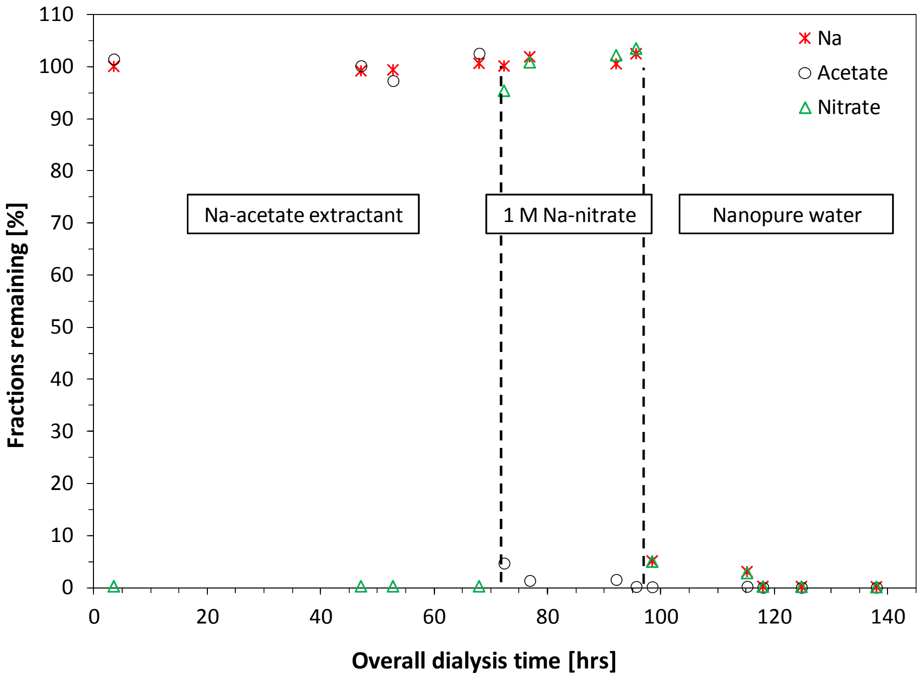

Figure 5.2. Fractions of sodium (Na), acetate and nitrate remaining in dialysis buffer solutions over the course of clay pretreatment.

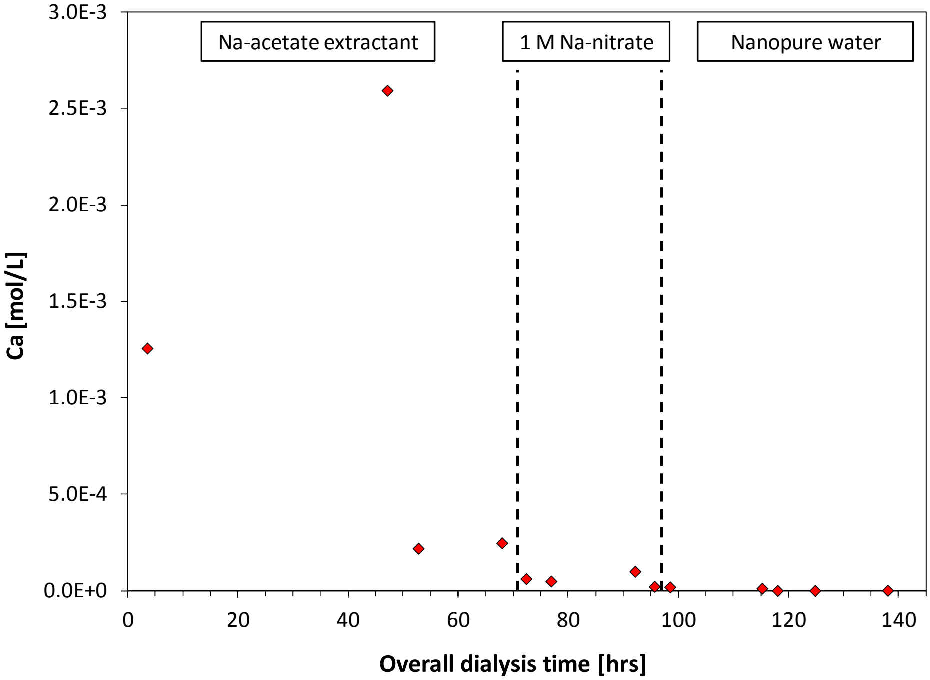

Figure 5.3. Calcium concentrations measured in dialysis buffer solutions over the course of clay pretreatment.

### 5.3.2 Batch Sorption Equilibrium Experiments

The results from the batch U(VI) sorption equilibrium experiments will be the basis for the development of U(VI)-montmorillonite surface complexation models. They provide important input parameters in terms of total and dissolved U(VI), dissolved inorganic carbon (TIC), and calcium concentrations, equilibrated with the mineral phase at various pH conditions and partial pressures of $CO_2$(g). In the following, we describe and compare the data for all experiments in terms of uranium, TIC and Ca concentrations. Throughout this report, error bars for ICP-MS and TIC data represent 95% confidence intervals of analytical errors.

#### *5.3.2.1 Uranium(VI) Sorption*

In Figs. 5.4 to 5.6, U(VI) sorption onto Na-montmorillonite is illustrated for three different $CO_2$ gas compositions: (1) atmospheric $CO_2$ (0.039% $CO_2$), (2) $CO_2$-free atmosphere, and (3) ~1% $CO_2$ atmosphere. Each figure describes U(VI) sorption data in terms of percent U(VI) sorbed (primary y-axis) and log $K_d$ values (secondary y-axis). In addition, in Figures 5.7 and 5.8, all U(VI) sorption data are shown for visual comparison; Table 5-1 provides a detailed overview of all values.

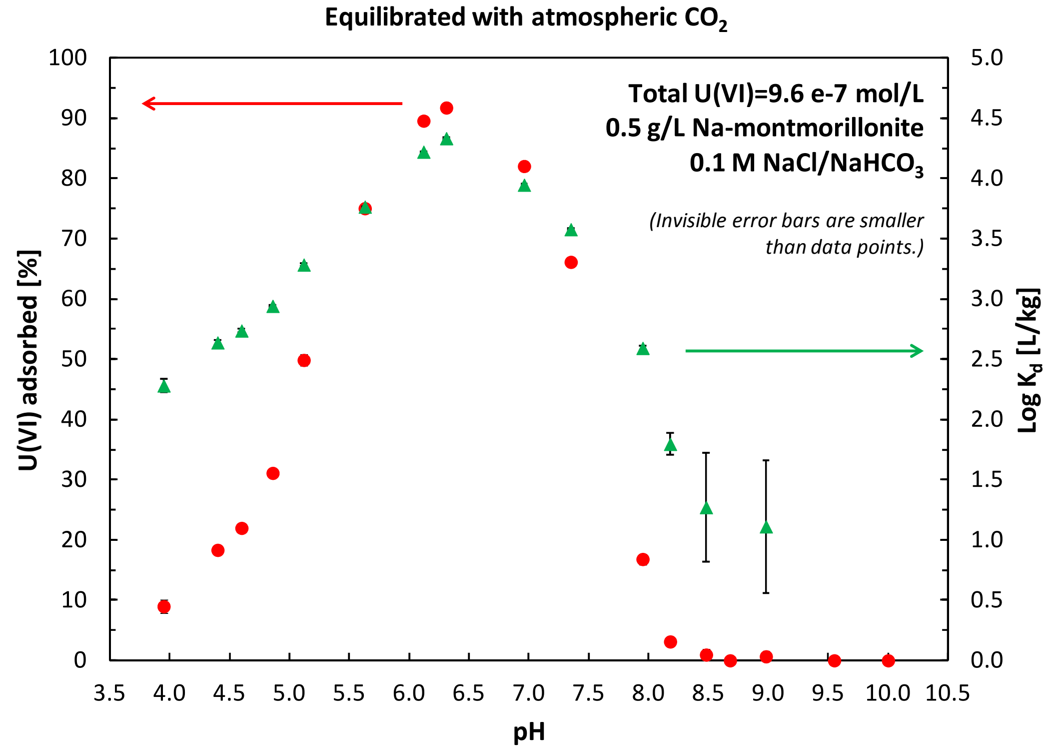

Figure 5.4. U(VI) adsorption onto Na-montmorillonite under atmospheric $CO_2$ conditions.

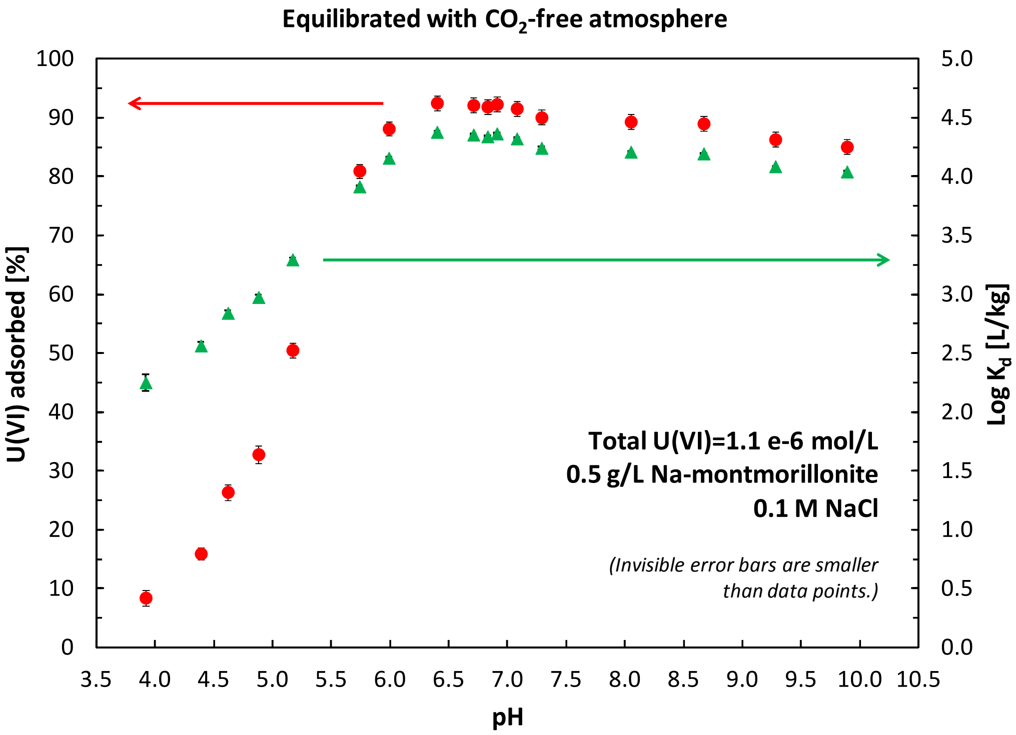

Figure 5.5. U(VI) adsorption onto Na-montmorillonite under an atmosphere free of $CO_2$ and $O_2$ gases.

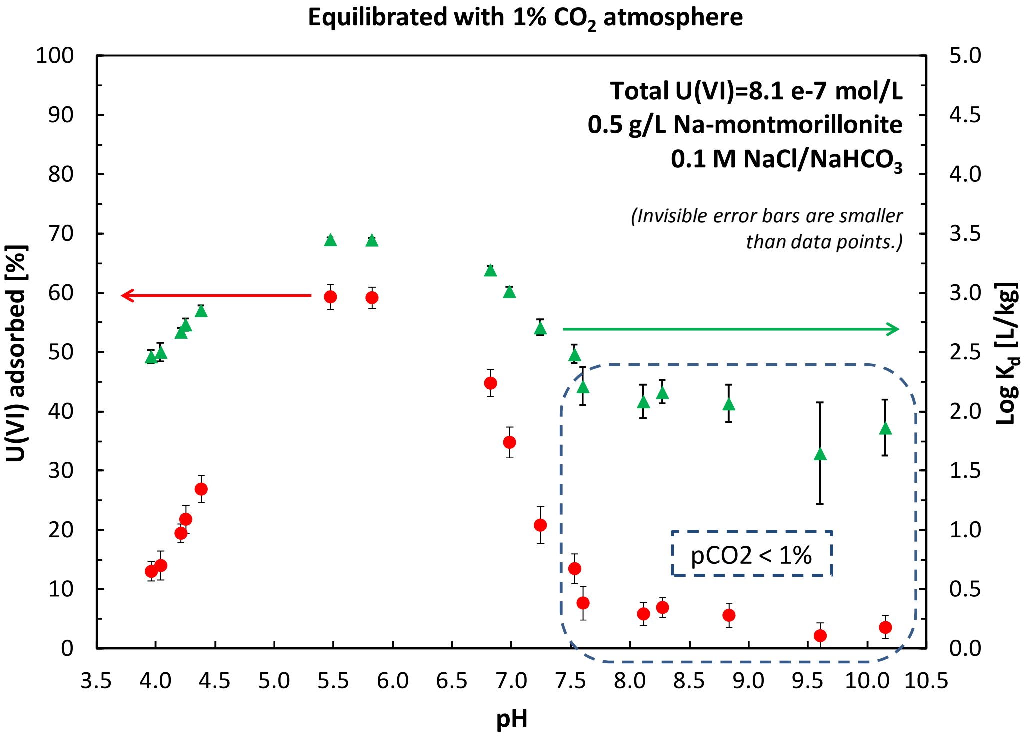

Figure 5.6. U(VI) adsorption onto Na-montmorillonite after equilibration with a ~1% $CO_2$ atmosphere.

Table 5.1. Summary of U(VI) adsorption data in batch sorption envelope experiments

| Atmospheric $CO_2$ | | | | $CO_2$-free atmosphere | | | | ~1% $CO_2$ atmosphere | | | |
|---|---|---|---|---|---|---|---|---|---|---|---|
| Final pH | U(VI) sorbed | Kd | log Kd | Final pH | U(VI) sorbed | Kd | log Kd | Final pH | U(VI) sorbed | Kd | log Kd |
| [ ] | [%] | [L/kg] | [L/kg] | [ ] | [%] | [L/kg] | [L/kg] | [ ] | [%] | [L/kg] | [L/kg] |
| 3.95 | 8.98 | 191 | 2.28 | 3.92 | 8.46 | 179 | 2.25 | 4.04 | 14.09 | 318 | 2.50 |
| 4.40 | 18.33 | 434 | 2.64 | 4.39 | 15.96 | 367 | 2.57 | 3.96 | 13.10 | 292 | 2.47 |
| 4.60 | 21.98 | 545 | 2.74 | 4.62 | 26.42 | 695 | 2.84 | 4.21 | 19.53 | 470 | 2.67 |
| 4.86 | 31.10 | 874 | 2.94 | 4.88 | 32.83 | 946 | 2.98 | 4.25 | 21.89 | 543 | 2.73 |
| 5.12 | 49.86 | 1,925 | 3.28 | 5.17 | 50.54 | 1,978 | 3.30 | 4.38 | 26.99 | 715 | 2.85 |
| 5.63 | 75.04 | 5,820 | 3.76 | 5.74 | 80.98 | 8,239 | 3.92 | 5.47 | 59.41 | 2,833 | 3.45 |
| 6.12 | 89.57 | 16,624 | 4.22 | 5.99 | 88.15 | 14,403 | 4.16 | 5.82 | 59.27 | 2,817 | 3.45 |
| 6.31 | 91.75 | 21,533 | 4.33 | 6.40 | 92.52 | 23,945 | 4.38 | 6.82 | 44.86 | 1,575 | 3.20 |
| 6.96 | 82.05 | 8,845 | 3.95 | 6.71 | 92.15 | 22,712 | 4.36 | 6.98 | 34.88 | 1,037 | 3.02 |
| 7.35 | 66.13 | 3,780 | 3.58 | 6.83 | 91.89 | 21,917 | 4.34 | 7.24 | 20.91 | 512 | 2.71 |
| 7.95 | 16.82 | 391 | 2.59 | 6.91 | 92.30 | 23,211 | 4.37 | 7.53 | 13.56 | 304 | 2.48 |
| 8.18 | 3.13 | 63 | 1.80 | 7.08 | 91.58 | 21,049 | 4.32 | 7.60 | 7.77 | 163 | 2.21 |
| 8.48 | 0.95 | 19 | 1.27 | 7.29 | 90.06 | 17,528 | 4.24 | 8.11 | 5.92 | 122 | 2.09 |
| 8.68 | n.d. | n/a | n/a | 8.05 | 89.33 | 16,212 | 4.21 | 8.27 | 7.01 | 146 | 2.16 |
| 8.98 | 0.66 | 13 | 1.11 | 8.67 | 89.03 | 15,703 | 4.20 | 8.83 | 5.70 | 117 | 2.07 |
| 9.55 | n.d. | n/a | n/a | 9.28 | 86.32 | 12,216 | 4.09 | 9.60 | 2.24 | 44 | 1.65 |
| 10.00 | n.d. | n/a | n/a | 9.89 | 85.07 | 11,027 | 4.04 | 10.15 | 3.64 | 73 | 1.86 |

Under atmospheric $CO_2$ conditions, U(VI) sorption onto Na-montmorillonite is characterized by relatively low sorption in low and high pH regions, and a sorption maximum at around pH 6.3 (Figure 5.4). At low pH, U(VI) sorption is assumed to be limited due to its competition with protons for the same reactive surface/ion exchange sites (Stumm, 1992). At high pH, low uranium sorption is attributed to increasing carbonate concentrations leading to weakly or non-sorbing aqueous U(VI)-carbonato complexes (Davis et al., 2004; Hsi and Langmuir, 1985). Highest and lowest U(VI) $K_d$ values ranged from $K_d$ = 21,533 L/kg (92% U(VI) sorbed) at pH=6.3 to $K_d$ = 13 L/kg (0.7% U(VI) sorbed) at pH=9. At pH=4, the $K_d$ value was determined at 191 L/kg (9% U(VI) sorbed). Hence, under atmospheric $CO_2$ conditions, U(VI)-montmorillonite distribution coefficients vary over three orders of magnitude as a function of pH.

In $CO_2$-free systems (Figure 5.5), the shape of the U(VI) batch sorption envelope is different compared to the atmospheric $CO_2$ system. In the low-pH region, U(VI) sorption characteristics remain similar with comparable $K_d$ values in the pH range from 4 to 6. Above pH 7, however, U(VI) sorption is much stronger in the absence of $CO_2$. The increase in U(VI) sorption at high pH values is attributed to the lack of aqueous U(VI)-carbonato complexes in the $N_2$(g) environment. As a result, $K_d$ values varied from a lowest value of 179 L/kg (8.5% U(VI) sorbed) at pH = 3.9 to a high of 23,945 L/kg (93% U(VI) sorbed) at pH = 6.4. From pH = 6.7 to pH = 9.9, $K_d$ values decreased only by a factor of around 2 (from 22,712 to 11,027 L/kg).

The effect of carbonato solution complexes on U(VI) sorption characteristics is also demonstrated by U(VI) sorption results for the system with elevated $CO_2$ concentrations (~1% $CO_2$ atmosphere). In this case, the shape of the sorption envelope is similar to the one determined under atmospheric carbon dioxide conditions. However, U(VI) sorption decreased at pH values greater than 5.8 ($K_d$ = 2,817 L/kg, 59% U(VI) sorbed). Due to an error in the experimental set up and problems with a disposable glove bag, only solutions up to a pH of 7.24 were equilibrated with the ~1% $CO_2$ atmosphere; solutions at higher pH values had lower inorganic carbon concentrations than would be expected for a 1% atmosphere (for details, see

TIC results). Hence, only the experimental data points up to pH = 7.24 were included in the visual comparison (Figures 5.7 and 5.8). However, it can be assumed that at ~1% $CO_2$, U(VI) sorption would be similar or lower at the higher pH value, again due to the influence of carbonate solution species. The experiment with the 1% $CO_2$ atmosphere is being repeated to overcome the experimental error.

#### 5.3.2.2 Uranium Wall Sorption

A comparison of U(VI) sorption onto container wall surfaces was determined for all three types of batch sorption experiments in Figure 5.9. In general, U(VI) wall sorption was low, with less than 2% of the total U(VI) solution concentrations lost onto container walls. U(VI) wall sorption exhibits a similar pH dependence to U(VI) sorption on montmorillonite under atmospheric $CO_2$ conditions. Interestingly, the data from the ~1% $CO_2$ experiment suggest that higher amounts of U(VI) were sorbed onto container walls at elevated carbonate concentrations.

#### 5.3.2.3 Total Inorganic Carbon (TIC)

A comparison of TIC data for all types of batch sorption envelope experiments is provided in Figure 5.10. The TIC results for the experiment performed under atmospheric $CO_2$ conditions generally follow the values expected from the literature. For the $CO_2$-free glove box experiment, we see a slight increase in TIC concentrations with increasing pH. This is an indication that the glove bag is not able to exclude carbon dioxide completely; however, $CO_2$ contamination was fairly minor.

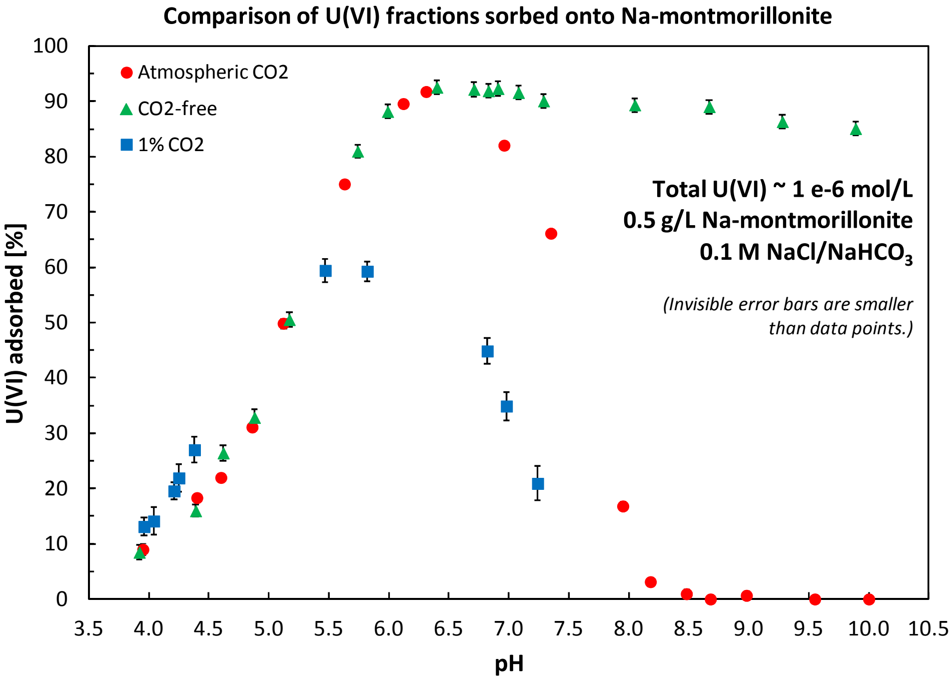

Figure 5.7. Comparison of U(VI) sorbed onto Na-montmorillonite in batch sorption equilibrium experiments.

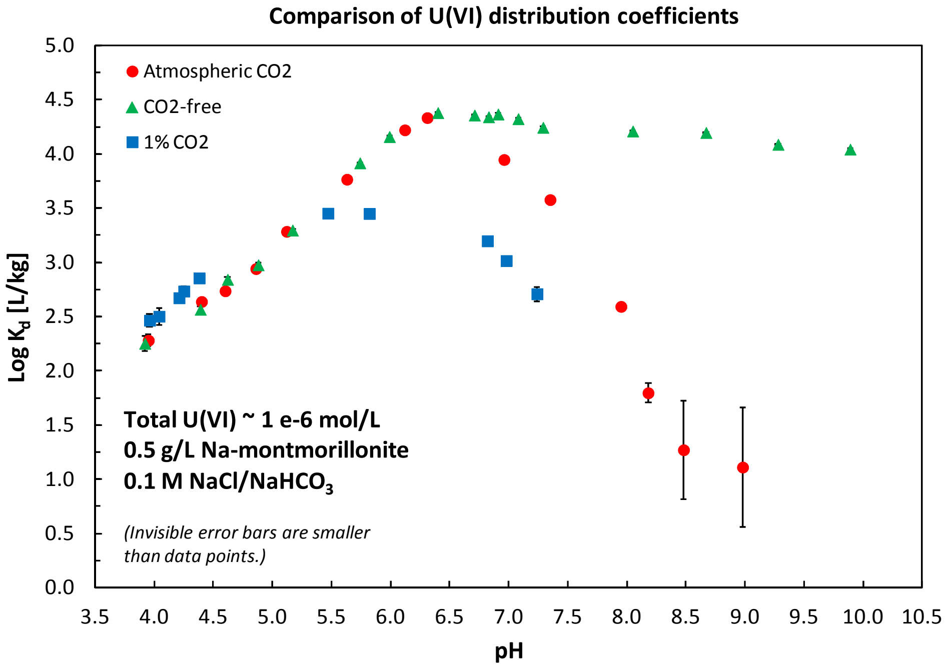

Figure 5.8. Comparison of U(VI)-montmorillonite $K_d$ values determined in batch sorption equilibrium experiments.

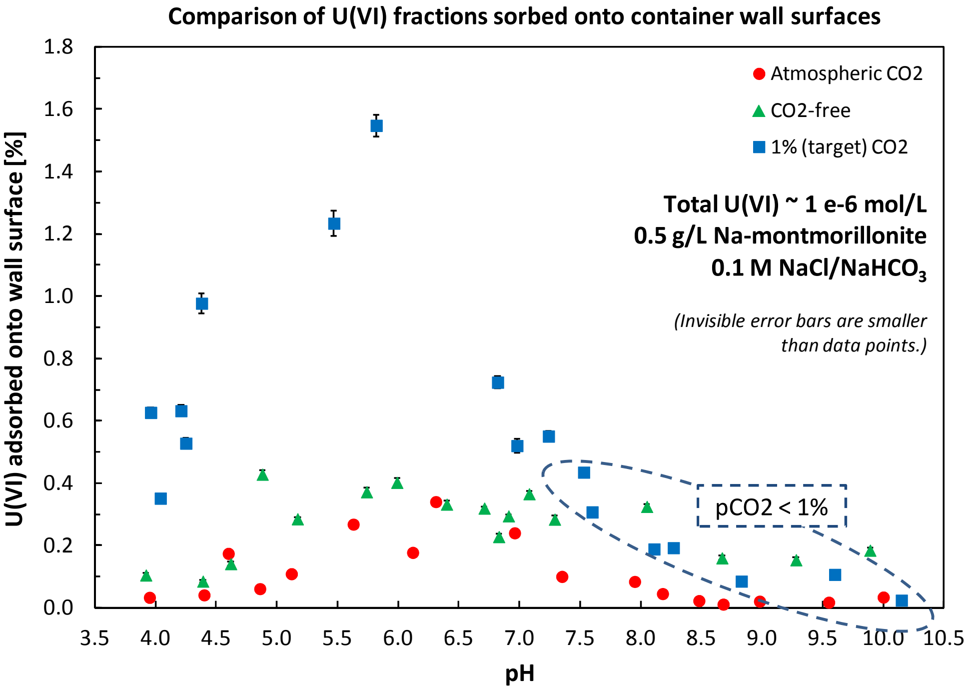

Figure 5.9. U(VI) container wall sorption determined in batch sorption envelope experiments.

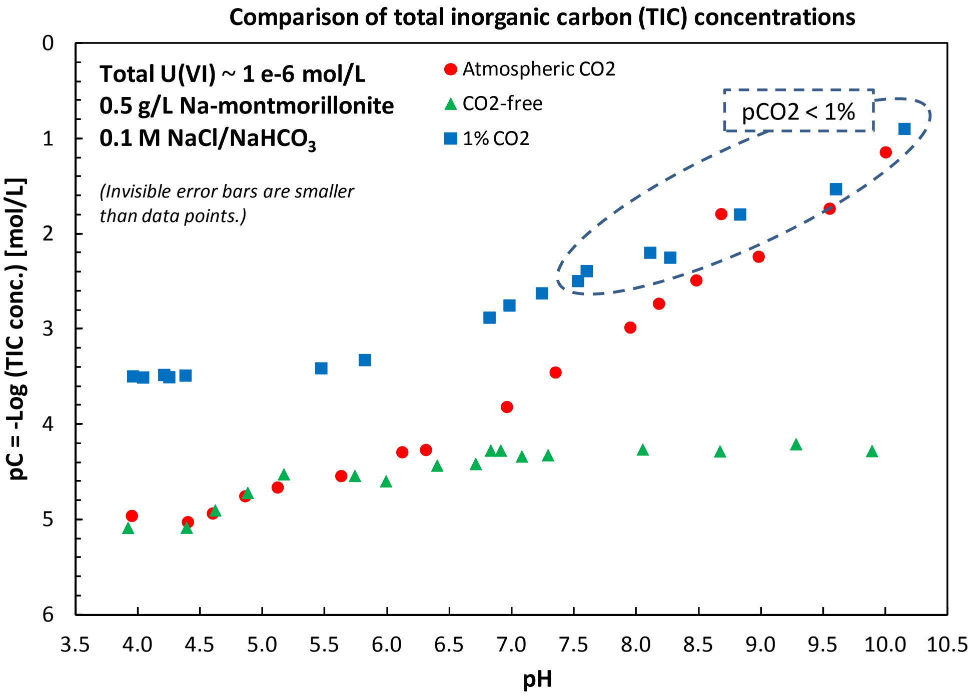

Figure 5.10. Total inorganic carbon (TIC) concentrations measured in batch sorption envelope experiments.

For the experiment set up at elevated (2%) $CO_2$, the TIC results suggest some experimental problems. Using these data, we back-calculated the atmospheric $CO_2$ concentrations equilibrated with the measured total carbonate concentrations in solution. We determined that solutions up to a pH of 7.24 were equilibrated with ~1% $CO_2$, while solutions at higher pH values showed lower dissolved carbonate contents than expected. First, this indicates that the purging of solutions and of the disposable glove bag with 2% $CO_2/N_2$ gas was insufficient. In addition, it was found that the amounts of sodium bicarbonate buffer added to solutions at higher target pH values were not high enough. Based on these results, the latter data points were excluded from comparisons of U(VI) sorption data determined in other carbon dioxide environments (Figures 5.7 and 5.8). However, data points in the lower pH region are still representative for a 1% $CO_2$ atmosphere.

#### 5.3.2.4 Calcium

Total calcium concentration data are shown in Figure 5.11, and as Ca released from the clay mineral in Figure 5.12. The latter was calculated based on the subtraction of Ca contents in blanks containing no mineral phase. Blank values ranged from 42 to 109 µg/L Ca in the experiments, and contributed between 5.6% and 25% of total Ca concentrations in solution. The addition of sodium bicarbonate buffer solutions at elevated pH values may also slightly add to Ca background concentrations. For instance, if we assume that the degree of purity of $NaHCO_3$ given by the manufacturer (99.998%) is accurate, and all buffer impurities are due to Ca, the buffer addition to a pH = 10 sample at atmospheric $CO_2$ levels would increase the Ca background by around $3 \times 10^{-6}$ mol/L Ca (128 µg/L Ca). Hence, Ca background concentrations in the added $NaHCO_3$ buffer cannot fully explain the increase in Ca levels with higher pH values. Instead, this trend may indicate that carbonate ligands in solution may enhance Ca release from the clay mineral. This hypothesis is further supported by lower Ca concentrations found in solutions in contact with atmospheric/$CO_2$-free gas phases in comparison to the Ca levels found in solutions in contact with the ~1% $CO_2$ atmosphere. Overall, in these systems the determined Ca background concentration levels are not high enough to affect U(VI) solution speciation in terms of the formation of ternary U(VI)-Ca-carbonato solution complexes. Typical Ca concentrations with relevant effects on U(VI) speciation are at millimolar concentrations (Fox, et al., 2006).

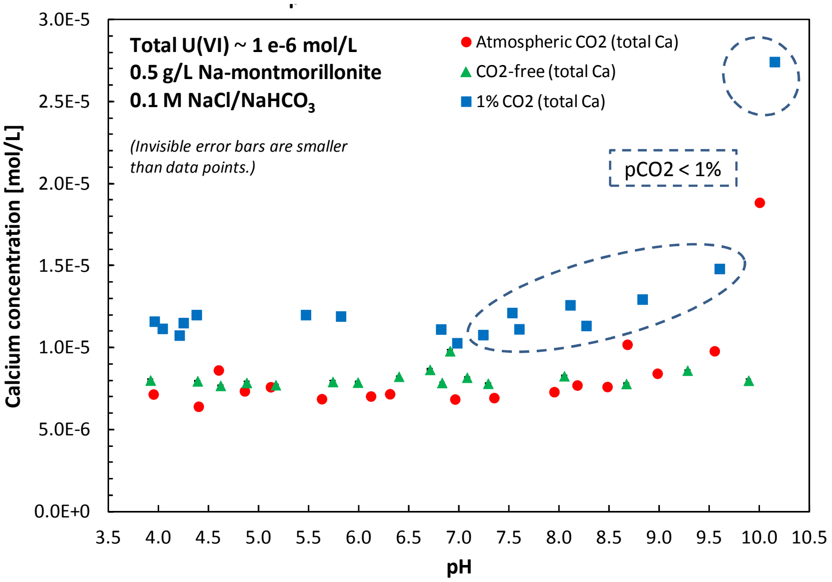

Figure 5.11. Total calcium concentrations measured in U(VI) batch equilibrium experiments.

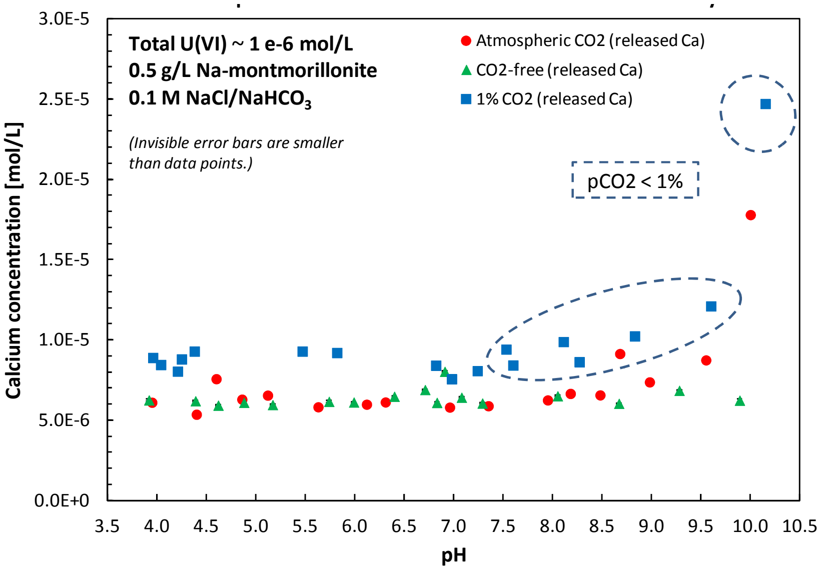

Figure 5.12. Ca concentrations released from Na-montmorillonite in batch experiments, corrected for background Ca.

### 5.3.3 Batch Sorption Kinetic Experiments

In experiments conducted at a (target) pH value of 5.0, U(VI) shows an initial fast uptake, followed by slower sorption kinetics (Figure 5.13). As a result, U(VI) $K_d$ values (Figure 5.14) slightly increase over time. For instance, for an ionic strength of 0.002 M, $K_d$ values increased from 12,700 L/kg (2 days) to 23,100 L/kg (13 days), for I=0.01 M, from 8,350 L/kg to 10,200 L/kg, and for I=0.1 M from 1,710 L/kg to 2,480 L/kg. Hence, distribution coefficients determined at sorption equilibration times of 2 days are slightly lower than those determined under full steady-state conditions. Furthermore, it appears that these slower, long-term sorption processes may be affected by the ionic strength conditions in sample solutions. Increasing ionic strength seems to cause slower overall sorption reactions in comparison to lower salt contents.

However, based on the data depicted in Figures 5.13 and 5.14, the potential influence of ionic strength on U(VI) sorption kinetics is difficult to judge.

Figure 5.15 shows the results normalized to the final values of U(VI) surface concentrations reached in kinetic experiments, assuming for now that these concentrations represent steady-state values. Assuming pseudo-first order reversible sorption kinetics and constant chemical conditions, two systems should show the same kinetic sorption behavior if they reach their individual equilibrium surface concentrations at the same rate (Espenson, 1995). In other words, systems with the same pseudo-first order sorption kinetics show the same fractional approach to equilibrium at any given point in time, independent of the individual equilibrium surface concentrations reached. Typically, reaction kinetics are compared between systems using a ‘characteristic time’ where 50% of equilibrium concentrations have been approached (Espenson, 1995; Stone and Morgan, 1990). However, due to the fast sorption rates observed for the lowest ionic strength conditions, we decided to evaluate potential differences in U(VI) sorption kinetics due to ionic strength for time-points where 95% of the U(VI) equilibrium surface concentrations have been reached. The 95% limit is indicated as a horizontal, green line in Figure 5.15. Based on this interpretation, the time-frames needed to the reach the same fraction of the U(VI) sorption equilibrium is longer with increasing ionic strength, given that other chemical conditions were constant. Figure 5.16 illustrates that dissolved inorganic carbon remained fairly constant throughout the experiments. On the other hand, pH values seemed to consistently increase in all samples over time (Figure 5.17). In the near future, we will use surface complexation modeling as a tool to determine if these pH changes had a significant impact on the kinetic behavior observed.

The results suggest the possibility that different sorption mechanisms were dominant at various ionic strength conditions. For instance, it might be possible that at low ionic strength (fast) ion exchange reactions drive the overall sorption kinetics at pH 5 (McKinley et al., 1995). At higher ionic strengths, surface complexation reactions at clay edge sites might gain importance due to the increased competition between U(VI) ions and other cations for ion exchange sites. Therefore, (possibly slower) surface complexation reactions may become more and more relevant under these conditions. However, other explanations for this behavior are also possible, and will be evaluated in further detail in the future.

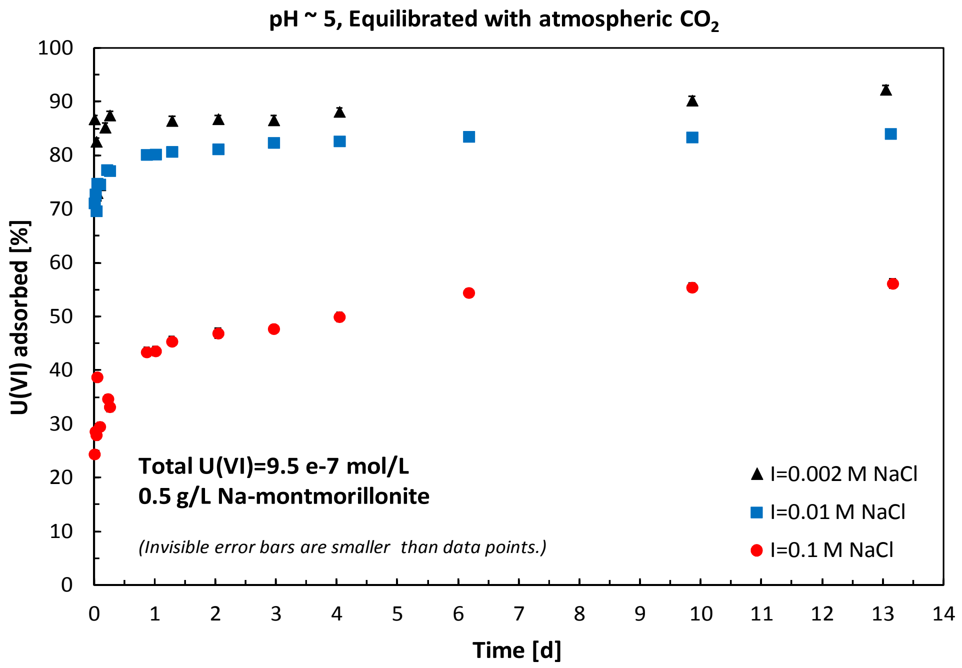

Figure 5.13. U(VI) sorption as a function of time at pH=5, equilibrated with air.

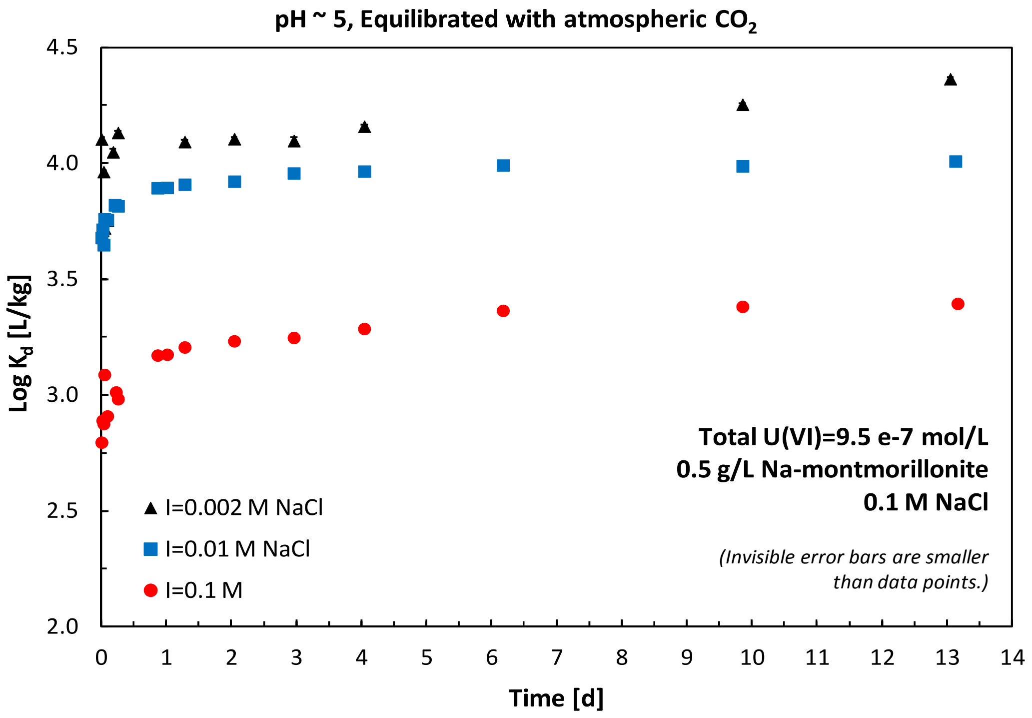

Figure 5.14. U(VI) $K_d$ values with time at pH=5, equilibrated with air.

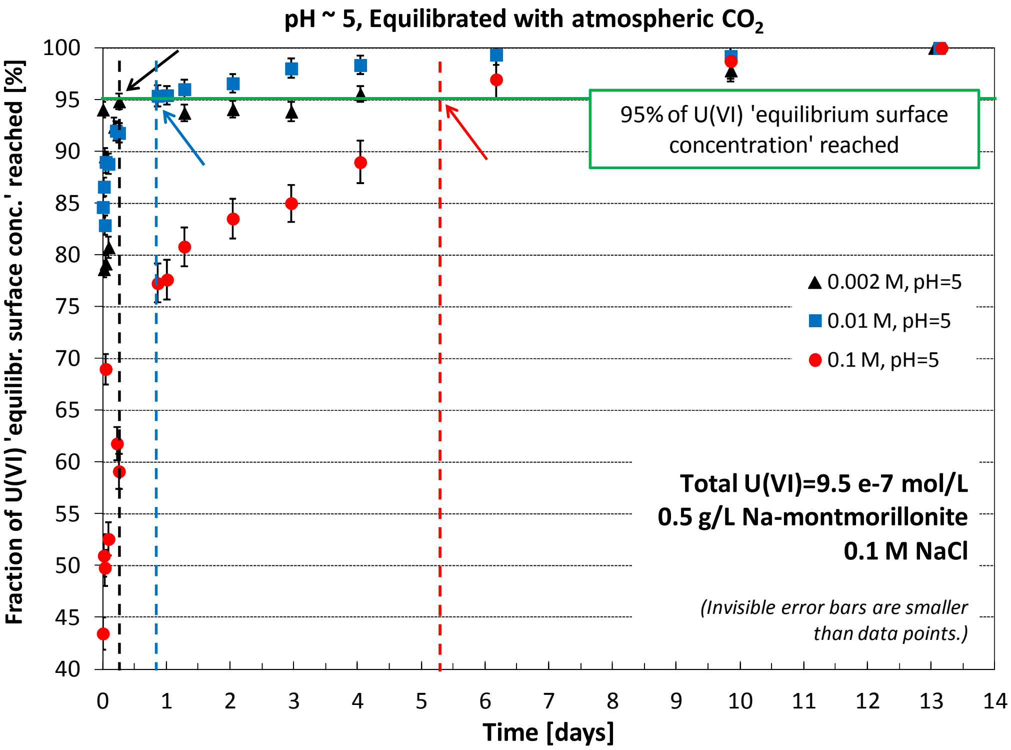

Figure 5.15. Fractional approach to equilibrium for U(VI) sorption at pH 5. The 95%-fraction of U(VI) surface concentrations is reached at each ionic strength when the series of experimental data points crosses the green horizontal line.

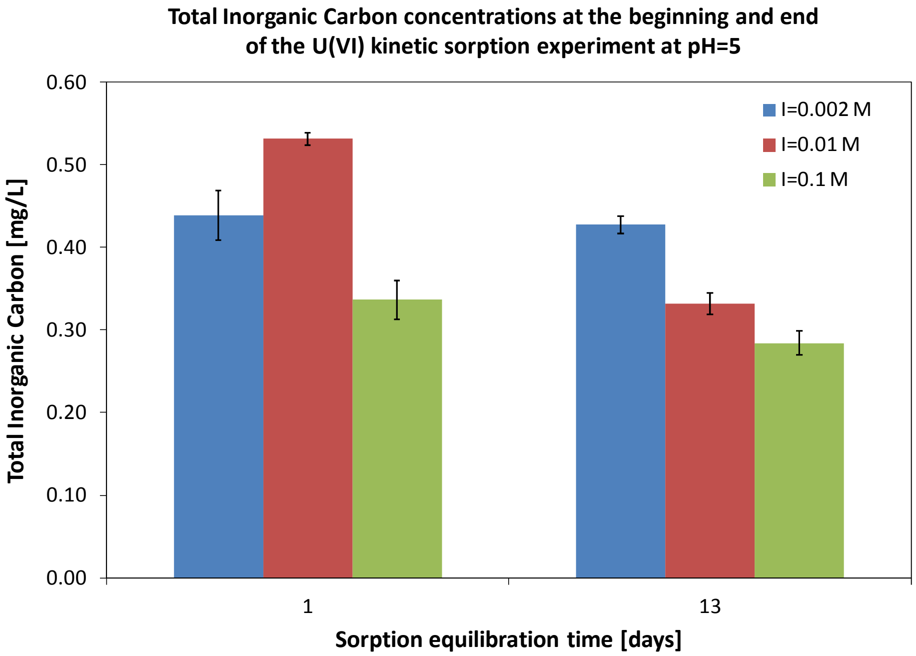

Figure 5.16. Dissolved inorganic carbon concentrations at the beginning and end of the U(VI) kinetic experiments at pH 5 in air.

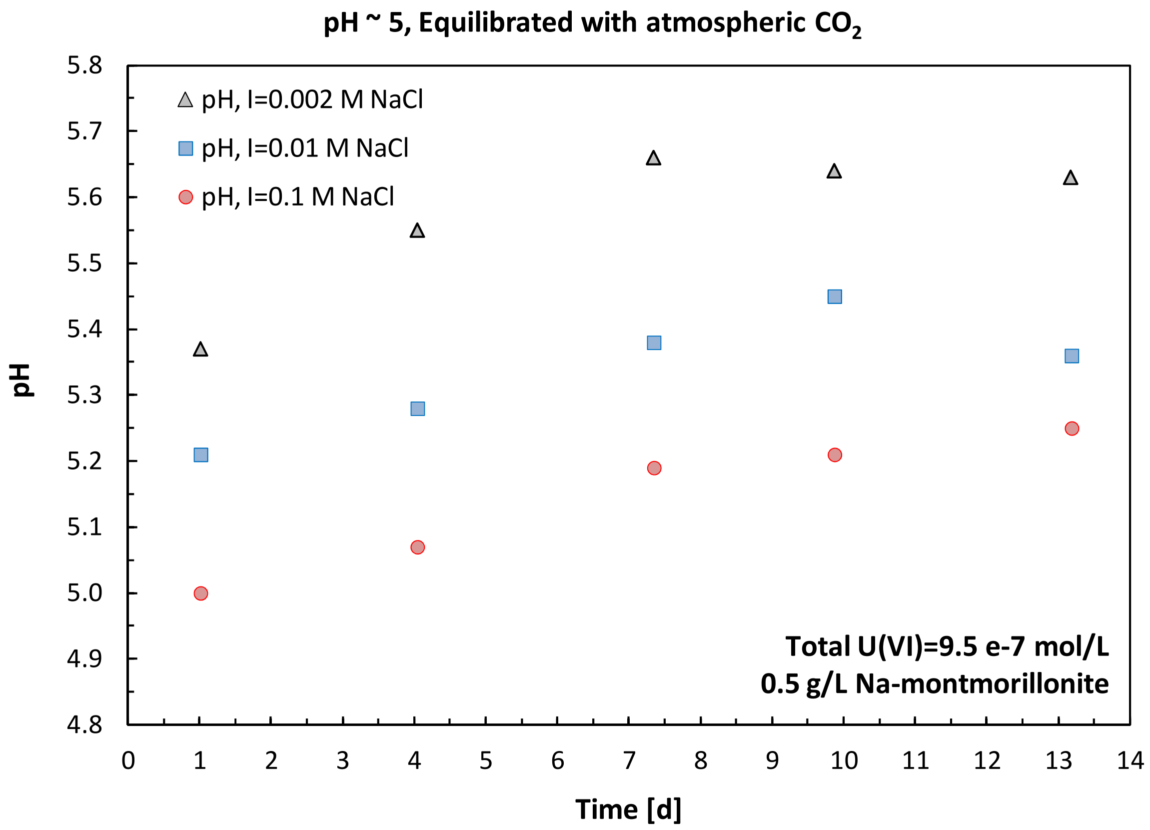

Figure 5.17. pH as a function of time in the U(VI) sorption experiments near pH 5 in air.

### 5.3.4 Surface Complexation Modeling

Preliminary surface complexation models have been developed to describe the experimental data as a function of chemical composition that are presented above. There are alternative approaches, depending on the type of electrical double layer model that is used as part of the surface complexation model. These results are an important step forward but were considered too preliminary to present at this stage.

## 5.4 Summary and Conclusions

Experimental studies of U(VI) sorption on montmorillonite show that $K_d$ values are highly dependent on the values of pH and bicarbonate concentration. We also expect that the values will be highly sensitive to the Ca concentration, based on work by Fox et al. (2006). In current models for radionuclide diffusion through bentonite in an engineered barrier, the apparent and effective diffusion coefficients are linked through the $K_d$ value, which is often believed to be a constant value for a particular radionuclide. In the case of U(VI), this is less likely to be true because of the very high sensitivity of the $K_d$ value to pH, and bicarbonate and calcium concentrations. It should be noted that the waste forms, and possibly concrete in the vicinity of an EBS, are likely to create gradients in these chemical variables within the EBS. Because of this, it is important to represent U(VI) partitioning within an EBS with a surface complexation model rather than a constant $K_d$ value.

Furthermore, in many diffusion studies that have been conducted, the chemistry of the diffusing ion (or neutral species) has been extremely simple, e.g., $Cl^-$, tritium. This is also true for cations, e.g. $Cs^+$, $Sr^{2+}$, which primarily bind to montmorillonite at ion exchange sites located in the interlamellar space within the mineral structure. Binding at these sites is substantially affected by compaction. However, binding of U(VI) is dramatically different from these cations. Although $UO_2^{2+}$ can bind to ion exchange sites at low pH and low ionic strength, it should be expected that under field-relevant conditions for an EBS U(VI) will bind to montmorillonite primarily by surface complexation at edge sites. It is unknown how this type of binding will affect U(VI) diffusion when montmorillonite is compacted.

In FY12, uranium(VI) sorption onto purified, Na-montmorillonite was studied in 0.1M NaCl solutions as a function of pH in systems equilibrated with $N_2(g)$, air, or a 98%/2% $N_2/CO_2$ gas mixture. $K_d$ values for U(VI) sorption onto bentonite equilibrated with air ranged from 13 L/kg at pH 9.0 to 21,500 L/kg at pH 6.5. At pH 4, the $K_d$ value was 191 L/kg. For systems equilibrated with $N_2(g)$, the $K_d$ values were approximately the same as in air in the pH range 4-6, but had much higher values in the range pH 7-9. The reason for the higher pH values was the lack of aqueous U(VI)-carbonate complexes in the pure $N_2(g)$ environment, which are more weakly adsorbed than the $UO_2(OH)_2(aq)$ species. For systems equilibrated with a $CO_2$ partial pressure of ~1%, $K_d$ values were much lower than in air in the pH range 6-8 because of higher concentrations of the aqueous U(VI)-carbonate complexes.

# 6. OVERALL SUMMARY

Bentonite and bentonite-sand mixtures have been found to have favorable properties for use as a backfill/buffer material for nuclear waste repositories. This report focuses on analyses of bentonite as a component of the EBS. Specific analyses presented here highlight progress made in areas of THM coupled processes models, reactive transport models, and reactive transport experiments for bentonite. These research activities address key Features, Events and Processes (FEPs) with rankings from medium to high, as listed in Tables 7 and 8 of *Used Fuel Disposition Campaign Disposal Research and Development Roadmap* (FCR&D-USED-2011-000065 REV0) (Nutt, 2011).

## 6.1 THM Process Modeling in Bentonite

We are developing and applying coupled THMC models for the analysis of EBS coupled processes in bentonite-backfilled repositories. This activity addresses FEP 2.2.01, Excavation Disturbed Zone (EDZ), for shale by investigating the effects of coupled processes on interactions between shale (clay) disposal formations and the EBS; FEPs 2.1.04.01, Buffer/Backfill; FEPs 2.1.07.02, 03, 04, 09, Mechanical Processes; FEPs 2.1.08.03, 07, 08, Hydrologic Processes; and FEP 2.1.11.04, Thermal Processes, by studying coupled processes in the EBS. In FY11, we developed an advanced modeling capability by implementing the Barcelona Basic Model into the TOUGH-FLAC simulator. In FY12, we have further improved our modeling capability and initiated a modeling validation study using international data sets. Our FY12 accomplishments for this activity include:

- We expanded Barcelona Basic Model to a dual-structure model for expansive clay, such as bentonite. We have implemented a dual-structure model and are currently testing and verifying this implementation against published numerical modeling and experimental data. The next step will then be to link the dual-structure model with diffuse double layer theory for the coupling between chemistry and mechanics resulting in a coupled THMC model for the analysis of the long-term EBS behavior.
- We have initiated the work on the modeling of the HE-E heater test along with our participation in the DECOVALEX project. The first phase will involve modeling of a previous HE-D heater test for calibration and validation of the rock mass model related to THM processes under heating of the Opalinus clay.

In the remaining months of FY12, we will

- Complete testing and documentation of dual-structure model.
- Perform Mont Terri HE-heater test modeling along with DECOVALEX schedule in FY12:
    - Final Task description to be delivered to research teams in June.
    - Modeling previous Mont Terri rock mass HE-D heater test for calibration of THM rock properties (until October 2012).
- Link dual-structure model with diffuse double layer theory for the development of THMC EBS model.
- Test THMC model against laboratory experiments (e.g. swelling under different salinity).

For FY13, we propose to conduct

- Mont Terri HE-heater test modeling along with DECOVALEX schedule in FY13
- Buffer material study of THM experimental data provided by DECOVALEX to determine and calibrate buffer properties (until October 2013)
- Dual-structure material modeling of FEBEX mock-up test
- Application of new THMC model for generic repository cases

## 6.2 Modeling Reactive-Diffusive Transport in Bentonite

The focus of this activity has been on developing rigorous and yet practically useful approaches to modeling diffusive process in bentonite. This activity addresses Features, Events and Processes (FEPs), FEPs 2.1.04.01, Buffer/Backfill; and FEPs 2.1.09.52, 53, 54, Chemical Processes—Transport by investigating reactive-diffusive radionuclide transport in bentonite. Our FY12 accomplishments include:

- We have improved the DDL modeling capability based on the Donnan equilibrium or mean electrostatic approach. It allows for calculating a DDL thickness (or volume) using ionic strength.
- We have developed an improved model involving the coupling of the PNP set of equations with a suitable surface complexation model as an attempt to advance our capability in modeling diffusion processes in clay. The corresponding code is calibrated against previously provided benchmarks and an example 2D simulation of the electrical potential field is shown for the case in which charged clay surfaces modify the result. The good agreement we have achieved with available experimental data supports the usefulness of our model. In addition, the present study has served to reconcile the theory of the Poisson–Boltzmann equation with seemingly conflicting experimental evidence of non-zero anion concentrations found in highly compacted clays, by making use of the theory of fractals. If proved suitable, that would have relevant implications in the process of upscaling results from the nano- up to macro-scales, based on the self-similarity of the fractal structure of clays.

In the remaining months of FY12, we will:

- Complete implementation of multicomponent Poisson-Boltzmann equation in new finite element code.
- Test against full range of Van Loon et al (2007) diffusion data for model validation.

For FY13, we propose to

- Complete implementation of multicomponent Poisson-Boltzmann Equation in general purpose reactive transport simulator.
- Use mean electrostatic and Poisson-Boltzmann models to simulate Fernández and Mäder (2011) experiments involving flow and transport through clay
- Use mean electrostatic and Poisson-Boltzmann models to simulate the experiments on uranium sorption and transport conducted in Section 5.

- Introduce calculations of the swelling pressure based on both the Poisson-Boltzmann and mean electrostatic (Donnan) approach.

## 6.3 Molecular Dynamics Prediction of Nanopore-Scale Diffusion Coefficients

The objective of our MD simulations is to develop the capability (based on first principles) to predict the temperature dependence of water and solute diffusion coefficients ($D$) in clay interlayer nanopores, considering that EBS is subject to substantial temperature variations. This activity addresses Features, Events and Processes (FEPs), FEPs 2.1.04.01, Buffer/Backfill; and FEPs 2.1.09.52, 53, 54, Chemical Processes—Transport by investigating reactive-diffusive radionuclide transport in bentonite. Our FY12 accomplishments for this activity include:

- We have developed a robust MD simulation methodology that correctly predicts the temperature dependence of sodium diffusion in bulk liquid water. This methodology predicts that sodium diffusion has a lower activation energy ($E_A$) in the three-layer hydrate of Na-montmorillonite than in bulk liquid water. These results open up a promising avenue for modeling and interpreting experimental results on the activation energy of diffusion of ionic solutes in macroscopic samples of compacted montmorillonite.

In the remaining months of FY12, we will

- Make efforts to obtain more precise $E_A$ values (by extending the duration of our simulations).
- Predict the $E_A$ value of sodium in the two-layer hydrate of Na-montmorillonite (to better understand the influence of compaction).

For FY13, we propose to

- Determine the activation energy of diffusion of $Cs^+$ in Na-MMT interlayers (by replacing a few $Na^+$ ions by $Cs^+$ ions in our simulations) and integrate the work with that described in Section 3.
- Develop a simulation methodology for investigating ion exchange between bulk liquid water and clay interlayers, which would enable us to predict the adsorption of $UO_2$ complexes in montmorillonite interlayer nanopores and its impact on effective diffusion coefficients. This last task would aid in the interpretation of the uranium diffusion experiments that are being carried out as described in Section 5.

## 6.4 Experimental Study on Reactive-Diffusive Transport

The major objective of this activity is to develop an improved understanding of radionuclide transport mechanisms and providing data sets for more accurately modeling the transport process in bentonite. This activity addresses Features, Events and Processes (FEPs), FEPs 2.1.04.01, Buffer/Backfill; and FEPs 2.1.09.52, 53, 54, Chemical Processes—Transport by investigating reactive-diffusive radionuclide transport in bentonite. In current models for radionuclide diffusion through bentonite in an engineered barrier, the apparent and effective diffusion coefficients are linked through the $K_d$ value, which is often believed to be a constant value for a particular radionuclide. In the case of U(VI), this is less likely to be true because of the very high sensitivity of the $K_d$ value to pH and bicarbonate and calcium concentrations. Our FY12 accomplishments for this activity include:

- We completed literature survey of diffusion experiments into montmorillonite and bentonites and surface complexation modeling of U(VI) on montmorillonite.
- We developed experiment setup in the laboratory and obtained preliminary results of Uranium(VI) equilibrium and kinetic sorption studies ($K_d$ values) under different test conditions.

Plans for the remainder of FY12 and for FY13 include the diffusion studies of U(VI) into bentonite and montmorillonite at various degrees of compaction and under various aqueous chemical conditions. Further studies of U(VI) sorption onto montmorillonite will also be conducted, especially as a function of Ca concentration.

Specifically, in the remainder of FY12, we will

- Complete analysis of batch kinetic studies of U(VI) sorption on montmorillonite. Conduct additional experiments if needed for interpretation of subsequent diffusion studies.
- Conduct kinetic and equilibrium U(VI) sorption experiments on montmorillonite as a function of calcium concentration
- Conduct one additional equilibrium experiment of U(VI) sorption on montmorillonite at an elevated partial pressure of $CO_2$(g), e.g. 10% $CO_2$.
- Complete/refine the surface complexation model for U(VI) sorption on montmorillonite by incorporating all experimental data collected in FY12.
- Design and complete fabrication of multiple diffusion cells for the study of U(VI) diffusion into montmorillonite and bentonite.
- Conduct preliminary study of U(VI) diffusion into montmorillonite for one set of chemical conditions.
- Engage in modeling collaborations with the diffusion modeling work conducted in Sections 3 and 4 to develop a diffusion model for U(VI) that is consistent with our experimental data.

In FY13, we will complete the following tasks listed below. These tasks are important for improving predictive models of diffusion of all actinide radionuclides through bentonite barriers. Such predictive models are an important component of performance assessment models for deep nuclear waste disposal.

- Conduct batch kinetic and equilibrium U(VI) sorption experiments on montmorillonite as a function of temperature. Complete/refine the surface complexation model for U(VI) sorption on montmorillonite by incorporating all experimental data.
- Conduct study of $Br^-$ and $Ca^{2+}$ diffusion into montmorillonite at low compaction and at pH 7 in 0.1M NaCl solutions equilibrated with air.
- Conduct studies of U(VI) diffusion into montmorillonite at low compaction and at low pH (5.0), circumneutral pH (7.0) and high pH (8.5) in 0.1M NaCl solutions equilibrated with air.
- Conduct study of U(VI) diffusion into montmorillonite at low compaction at pH 7 in 0.1M NaCl/1 mm $CaCl_2$ solution equilibrated with air.
- Conduct study of U(VI) diffusion into montmorillonite at intermediate and high compaction at pH 7 in 0.1M NaCl/1 mm $CaCl_2$ solution equilibrated with air.

- Conduct study of $Br^-$ and $Ca^{2+}$ diffusion into bentonite at low compaction and at pH 7 in 0.1M NaCl solutions equilibrated with air.
- Conduct studies of U(VI) diffusion into bentonite at low compaction and at low pH (5.0), circumneutral pH (7.0) and high pH (8.5) in 0.1M NaCl solutions equilibrated with air.
- Employ X-ray spectroscopic and electron-based imaging techniques to evaluate U(VI) diffusion on scales of microns up to one mm.
- Engage in modeling collaborations with the activities described in Section 3 and 4 to develop a diffusion model for U(VI) that is consistent with our experimental data.

# 7. REFERENCES

Alonso E.E., Vaunat J., Gens A. Modelling the mechanical behavior of expansive clays. *Engineering Geology*, **54**, 173–183 (1999).

Appelo, C.A.J. and Wersin, P., Multicomponent diffusion modeling in clay systems with application to the diffusion of tritium, iodide, and sodium in Opalinus Clay. *Environ. Sci. Techno*l. **41**, 5002-5007 (2007).

Appelo, C.A.J., Vinsot, A., Mettler, S. and Wechner, S., Obtaining the porewater composition of a clay rock by modeling the in- and out-diffusion of anions and cations from an in-situ experiment. *J. Contam. Hydrol*. **101**, 67-76 (2008)

Arai, Y., M. McBeath, J.R. Bargar, J. Joye, J.A. Davis, Uranyl adsorption and surface speciation at the imogolite-water interface: Self-consistent spectroscopic and surface complexation models, *Geochimica et Cosmochimica Acta*, **70**, 2492-2509 (2006).

Avena, M.J., De Pauli, C.P., Proton adsorption and electrokinetics of an Argentinean montmorillonite, *Journal of Colloid Interface Science* **202**, 195-204 (1998)

Bargar, J.R., R. Reitmeyer, J.J Lenhart, J.A. Davis, Characterization of U(VI)-carbonato ternary complexes on hematite: EXAFS and electrophoretic mobility measurements, *Geochimica et Cosmochimica Acta*, **64**(16), 2737-2749 (2000).

Bickmore, B.R., K.M. Rosso, K.L. Nagy, R.T. Cygan, C.J. Tadanier, *Ab initio* determination of edge surface structures for dioctahedral 2:1 phyllosilicates: Implications for acid-base reactivity, *Clays and Clay Minerals* **51**, 359-371 (2003).

Birgersson M., Karnland, O., Ion equilibrium between montmorillonite interlayer space and an external solution - Consequences for diffusional transport, *Geochimica et Cosmochimica Acta* **73**(7), 1908-1923 (2009).

Bourg, I.C., G. Sposito, Connecting the molecular scale to the continuum scale for diffusion processes in smectite-rich porous media, *Environmental Science and Technology* **44**, 2085-2091 (2010).

Bourg, I.C., A.C.M. Bourg and G. Sposito, Modeling diffusion and adsorption in compacted bentonite: a critical review, *J. Contam. Hydrol.* **61**, 293–302 (2003).

Bourg, I.C., G. Sposito and A.C.M. Bourg, Tracer diffusion in compacted, water-saturated bentonite, *Clays Clay Miner.* **54**, 363–374 (2006).

Bourg, I.C., Sposito, G. and Bourg, A.C.M. Modeling cation diffusion in compacted water-saturated sodium bentonite at low ionic strength. *Environ. Sci. Technol*. **41**, 8118–8122 (2007).

Bourg, I.C., G. Sposito, A.C.M. Bourg, Modeling the acid–base surface chemistry of montmorillonite, *Journal of Colloid and Interface Science*, **312**, 297-310 (2007).

Bradbury, M., B. Baeyens, A generalized sorption model for the concentration dependent uptake of caesium by argillaceous rock, *Geochimica et Cosmochimica Acta*, **42**, 141-163 (2000).

Bradbury, M., B. Baeyens, Sorption of Eu on Na- and Ca-montmorillonites: Experimental investigations and modelling with cation exchange and surface complexation**,** *Geochimica et Cosmochimica Acta*, **66**, 2325-2334 (2002).

Bradbury, M., B. Baeyens, Modeling the sorption of Mn(II), Co(II), Ni(II), Cd(II), Eu(III), Am(III), Sn(IV), Th(IV), Np(V) and U(VI) on montmorillonite: linear free energy relationships and estimates of surface binding constants for some selected heavy metals and actinides. *Geochimica et Cosmochimica Acta*, **69**, 875-892 (2005).

Bradbury, M., B. Baeyens, Predictive sorption modelling of Ni(II), Co(II), Eu(IIII), Th(IV) and U(VI) on MX-80 bentonite and Opalinus Clay: A "bottom-up" approach, Applied Clay Science, **52**, 27-33 (2011).

Catalano, J.G., G.E. Brown, Uranyl adsorption onto montmorillonite: Evaluation of binding sites and carbonate complexation, *Geochimica et Cosmochimica Acta*, **69**(12), 2995-3005 (2005).

Chen, T., B. Smit, A.T. Bell, Are pressure fluctuation-based equilibrium methods really worse than nonequilibrium methods for calculating viscosities? *Journal of Chemical Phys*ics **131**, 246101 (2009).

Chipera, S.J., D.L. Bish, Baseline studies of the Clay Minerals Society source clays: Powder X-ray diffraction analysis, *Clays and Clay Minerals*, **49**, 398-409 (2001).

Costanzo, P.A., S. Guggenheim, Baseline studies of the Clay Minerals Society source clays: Preface, *Clays and Clay Minerals*, **49**, 371-371 (2001).

Cygan, R.T., J.-J. Liang, A.G. Kalinichev, Molecular models of hydroxide, oxyhydroxide, and clay phases and the development of a general force field, *Journal of Physical Chemistry B* **108**:1255-1266 (2004).

Davis, J.A., D.M. Meece, M. Kohler, G.P. Curtis, Approaches to surface complexation modeling of uranium(VI) adsorption on aquifer sediments, *Geochimica et Cosmochimica Acta*, **68**, 3621-3641 (2004).

Ersahin, S., Gunal, H., Kutlu, T., Yetgin, B., Coban, S., Estimating specific surface area and cation exchange capacity in soils using fractal dimension of particle-size distribution, *Geoderma* **136**, 588–597 (2006).

Espenson, J. H., Chemical kinetics and reaction mechanisms. McGraw-Hill, Inc., New York, 1995.

Fernández, R. and Mäder, U., (2011) Modelling the bentonite column with CrunchFlow and comparison with PhreeqC, including diffuse layer features. NAGRA Report, April 18, 2011.

Ferrage, E., B.A. Sakharov, L.J. Michot, A. Delville, A. Bauer, B. Lanson, S. Grangeon, G. Frapper, M. Jiménez-Ruiz, G.J. Cuello, Hydration properties and interlayer organization of water and ions in synthetic Na-smectite with tetrahedral layer charge. Part 2. Toward a precise coupling between molecular simulations and diffraction data, *Journal of Physical Chemistry C* **115**:1867-1881 (2011).

Fox, P.M., J.A. Davis, J.M. Zachara, The effect of calcium on aqueous uranium(VI) speciation and adsorption to ferrihydrite and quartz, *Geochimica et Cosmochimica Acta*, **70**, 1379-1387 (2006).

Garitte, B., and others, HE-E experiment - In situ Heater Test, Presentation given at 1th DECOVALEX 2015 workshop, April 2012, Berkeley.

Gens, A, Alonso, E. A framework for the behaviour of unsaturated expansive clays. *Can. Geotech. J.* **29**, 1013–1032 (1992).

Gens, A., Sánchez, M., Sheng, D. On constitutive modelling of unsaturated soils. *Acta Geotechnica*, **1**, 137–147 (2006).

Gens, A., J. Vaunat, B. Garitte, B., Y. Wileveau, In situ behaviour of a stiff layered clay subject to thermal loading, observations and interpretation. *Geotechnique* **57**(2), 207–228 (2007).

Glaus, M.A., B. Baeyens, M.H. Bradbury, A. Jakob, L. Van Loon, A. Yaroshchuk, Diffusion of $^{22}$Na and $^{85}$Sr in montmorillonite: evidence of interlayer diffusion being the dominant pathway at high compaction, *Environmental Science and Technology*, **41**, 478-485 (2007).

Gonçalvès, J., Rousseau-Gueutin, P., Revil, A., Introducing inter-acting diffuse layers in TLM calculations: A reappraisal of the influence on the swelling pressure and the osmotic efficiency of compacted bentonites, *Journal of Colloid Interface Science* **316**, 92-99 (2007).

Holmboe, M., S. Wold, M. Jonsson, Porosity investigation of compacted bentonite using XRD profile modeling, *Journal of Contaminant Hydrology* **128**, 19-32 (2012).

Hsi, C.K.D., D. Langmuir, Adsorption of uranyl onto ferric oxyhydroxides: Application of the surface complexation site-binding model. *Geochimica et Cosmochimica Acta*, **49**, 1931-1941, (1985).

Kalinichev, A.G., R.J. Kirkpatrick, R.T. Cygan, Molecular modeling of the structure and dynamics of the interlayer and surface species of mixed-metal layered hydroxides: Chloride and water in hydrocalumite (Friedel's salt), *American Mineralogist* **85**,1046-1052 (2000).

Kozaki, T., H. Sato, A. Fujishima, S. Sato, H. Ohashi, Activation energy for diffusion of cesium in compacted sodium montmorillonite, *Journal of Nuclear Science and Technology* **33**, 522-524, 1996.

Kozaki, T., A. Fujishima, S. Sato, Self-diffusion of sodium ions in compacted sodium montmorillonite, *Nuclear Technology* **121**, 63-69 (1998).

Kozaki, T., H. Sato, S. Sato, H. Ohashi, Diffusion mechanism of cesium ions in compacted montmorillonite, *Engineering Geology* **54**, 223-230 (1999).

Kozaki, T., A. Fujishima, N. Saito, S. Sato, H. Ohashi, Effects of dry density and exchangeable cations on the diffusion process of sodium ions in compacted montmorillonite, *Engineering Geology* **81**, 246-254 (2005).

Kozaki, T., J. Liu, S. Sato, Diffusion mechanism of sodium ions in compacted montmorillonite under different NaCl concentration, *Physics and Chemistry of the Earth* **33**, 957-961, 2008.

Leroy, P., Revil, A., A triple-layer model of the surface electrochemical properties of clay minerals, *Journal of Colloid Interface Science* **270**(2), 371-380 (2004).

Leroy, P., A. Revil and D. Coelho, Diffusion of ionic species in bentonite, *J. Colloid Interface Sci.* **296** (1), 248–255 (2006).

Leroy P., Revil A., Altmann S., Tournassat C. Modeling the composition of a pore water in a clay-rock geological formation (Callovo-Oxfordian, France). *Geochimica et Cosmochimica Acta* **71**(5), 1087-1097 (2007).

Lichtner P.C. (1998) Modeling reactive flow and transport in natural systems. Proceedings of the Rome Seminar on Environmental Geochemistry, 5-72.

Mandelbrot, B., The fractal geometry of nature, W.H. Freeman and Co., New York, 1999.

McKinley, J.P., J.M. Zachara, S.C. Smith, G.D. Turner, The influence of uranyl hydrolysis and multiple site-binding reactions on adsorption of U(VI) to montmorillonite, *Clays and Clay Minerals*, **43**, 586-598 (1995).

Mermut, A.R., A.F. Cano, Baseline studies of the Clay Minerals Society source clays: Layer-charge determination and characteristics of those minerals containing 2:1 layers, *Clays and Clay Minerals*, **49**, 393-397 (2001).

Nagasaki, S., Sorption of uranium(VI) on Na-montmorillonite colloids - effect of humic acid and its migration. In: Y. Iwasawa, N. Oyama, H. Kunieda (Eds.), Studies in Surface Science and Catalysis. Elsevier, 2001.

Nutt, M., Used Fuel Disposition Campaign Disposal Research and Development Roadmap (FCR&D-USED-2011-000065 REV0), U.S. DOE Used Fuel Disposition Campaign, 2011.

OECD, Engineering barrier systems and the safety of deep geological repositories (State-of-the-art Report), ISBN 92-64-18498-8, 2003.

Plimpton, S., Fast parallel algorithms for short range molecular dynamics, *Journal of Computational Physics* **117**, 1-19 (1995).

Rutqvist J., Ijiri Y. and Yamamoto H. Implementation of the Barcelona Basic Model into TOUGH-FLAC for simulations of the geomechanical behavior of unsaturated soils. *Computers & Geosciences*, **37**, 751–762 (2011).

Sánchez, M., Gens, A., Guimarães, L. do N., Olivella, S. A double structure generalized plasticity model for expansive materials. *Int. J. Numer. Anal. Meth. Geomech*., **29**, 751–787. (2005).

Schoch, R.B., Han, J., Renaud, P., Transport phenomena in nanofluidics. *Reviews of Modern Physics* **80**,839-883 (2006).

Stone, A. T., J.J. Morgan, Kinetics of chemical transformations in the environment. In: W. Stumm (Ed.), Aquatic chemical kinetics: reaction rates of processes in natural waters. John Wiley & Sons, Inc., New York, 1990.

Steefel, C.I., CrunchFlow - Software for modeling multicomponent reactive flow and transport, 2009.

Steefel, C.I., K. Maher, 2009, Fluid-rock interaction: A reactive transport approach. *Reviews in Mineralogy and Geochemistry* **70**, 485-532, DOI: 10.2138/rmg.2009.70.11.

Stumm, W. Chemistry of the Solid Water Interface: Processes at the Mineral Water Particle Water Interface in Natural Systems, John Wiley & Sons, 428 p., 1992.

Tournassat, C., Appelo, C.A.J., Modelling approaches for anion-exclusion in compacted Na-bentonite, *Geochimica et Cosmochimica Acta* **75**(13), 3698-3710 (2011).

Tournassat, C., E. Ferrage, C. Poinsignon, L. Charlet, The titration of clay minerals: II. Structure-based model and implications for clay reactivity, *Journal of Colloid and Interface Science*, **273**, 234-246 (2004).

Van Loon, L.R., Glaus, M.A., Müller, W., Anion exclusion effects in compacted bentonites: Towards a better understanding of anion diffusion, *Applied Geochemistry* **22**(11), 2536-2552, 2007

Viani, B.E., Low, P.F., Roth, C.B., Direct measurement of the relation between interlayer force and interlayer distance in the swelling of montmorillonite, *Journal of Colloid and Interface Science* **96,** 229–244 (1983).

Wersin, P., Curti, E. and Appelo, C.A.J. Modelling bentonite-water interactions at high solid/liquid ratios: swelling and diffuse double layer effects. *Appl. Clay Sci*. **26**, 249-257 (2004).

Xu, Y.F., Sun, D., Yao, Y.P., Surface fractal dimension of bentonite and its application to determination of swelling properties, *Chaos, Solitons and Fractals* **19**, 347–356 (2004).

Xu, Y.F., Calculation of unsaturated hydraulic conductivity using a fractal model for the pore-size distribution, *Computers and Geotechnics* **31**, 549–557 (2004).

Yeh, I.-C., G. Hummer, System-size dependence of diffusion coefficients and viscosities from molecular dynamics simulations with periodic boundary conditions, *Journal of Physical Chemistry B* **108**,15873-15879 (2004).